Alma Mater Studiorum – Università di Bologna

DOTTORATO DI RICERCA IN

MONITORAGGIO E GESTIONE DELLE STRUTTURE E DELL'AMBIENTE – SEHM2

Ciclo XXXIV

Settore Concorsuale: 08/B3 – TECNICA DELLE COSTRUZIONI

Settore Scientifico Disciplinare: ICAR/09 – TECNICA DELLE COSTRUZIONI

DAMAGE IDENTIFICATION OF STRUCTURES THROUGH VIBRATION-BASED STRUCTURAL MONITORING SYSTEMS

Presentata da: MIRCO TAROZZI

Coordinatore Dottorato

Prof. Ing. Alessandro Marzani

Supervisore

Prof. Ing. Andrea Benedetti

Co-supervisore

Prof. Ing. Andrea Giorgetti

Esame finale anno 2022

Preface

The present thesis *"Damage Identification of Structures through Vibration-Based Structural Monitoring Systems"* has been made as a part of my PhD study programme from November 2018 to November 2021 at the Department of Civil, Chemical, Environmental and Materials Engineering, University of Bologna.

The thesis has been carried out within the *"SHAPE Project - Predicting Strength Changes in Bridges from Frequency Data Safety, Hazard, and Poly-harmonic Evaluation"* which dealt with the structural assessment of existing bridges and laboratory structural reproductions through the use of vibration-based monitoring systems, for detecting changes in their natural frequencies and correlating them with the occurrence of damage. SHAPE was one of the concurrent projects involved in the *"ERA-NET Plus Infravation 2014 Call"* and supported by the European Community. Thus, its financial support is gratefully acknowledged.

Acknowledgements

I am very grateful to my supervisor Andrea Benedetti, a full professor from the Department of Structural Engineering, University of Bologna, who assisted and guided me during the entire work, for all the food for thought that increased my curiosity and motivation on the research, for his patience and not at least technical and moral support during these years.

Thanks also to my co-advisor Andrea Giorgetti, associate professor from the Department of Electrical, Electronic, and Information Engineering "Guglielmo Marconi", and the people of the WiNET group for supporting me in the activities concerning the deployment of the network used for the monitoring of the dynamic behaviour of two existing bridges in Bologna.

I wish to thank Roberto Bianchi, Roberto Carli, Mario Marcolongo and all the other people of the LISG (Structural and Geotechnical Engineering Laboratory), at the University of Bologna, for their patience and in particular for their technical support and suggestions during the preparation of the setups and the execution of all the experimental tests.

Lastly but not least, I would like to thank my family, my friends and past and actual colleagues of mine for the moral support and the moment we shared together during my PhD study.

Bologna Mirco Tarozzi

January 2022

Abstract

The thesis has been carried out within the *"SHAPE Project - Predicting Strength Changes in Bridges from Frequency Data Safety, Hazard, and Poly-harmonic Evaluation"* which dealt with the structural assessment of existing bridges and laboratory structural reproductions through the use of vibration-based monitoring systems, for detecting changes in their natural frequencies and correlating them with the occurrence of damage. SHAPE was one of the concurrent projects involved in the *"ERA-NET Plus Infravation 2014 Call"* and supported by the European Community.

The main purpose of the research carried out in the aim of this PhD dissertation has been the detection of the variation of the main natural frequencies as a consequence of a previous-established damage configuration provided on a structure.

In the first part of the thesis, the effect of local damage on the modal feature has been discussed mainly concerning a steel frame and a composite steel-concrete bridge. Concerning the variation of the fundamental frequency of the small bridge, the effect of increasing severity of two local damages has been investigated. Moreover, the comparison with a 3D FE model is even presented establishing a link between the dynamic properties and the damage features which will be useful in planning the condition assessment through dynamic monitoring of real deteriorated full-scale bridges.

Then, moving towards a diffused damage pattern, four concrete beams and a small replica of a concrete deck were loaded achieving the yielding of the steel reinforcement. The fundamental problem of expressing the stiffness deterioration in terms of frequency shift has been reconsidered when a large set of dynamic experiments on simply supported ordinarily reinforced concrete beams discussed in the literature have been collected. The comparison of the normalized non-dimensional load-frequency curves suggested a significant agreement among all the experiments. Thus, in the framework of damage mechanics, the phenomenon of the "breathing cracks" has been discussed and the analytical formula able to explain the observed frequency decay has been proposed. The formula is still valid both for concrete beams and the small bridge deck.

Lastly, some dynamic investigations of two existing bridges and the corresponding Finite Element Models are presented in Chapter 4. Moreover, concerning the bridge in Bologna, two prototypes of a network of accelerometers were installed and the data of a few months of continuous monitoring have been processed and then illustrated.

Table of Contents

List of Figures

List of Tables

1 Introduction

1.1 Motivation and Objective

The problem of ensuring bridge safety, either in terms of early warning of critical conditions or maintenance scheduling, has a long history. A very simple and direct insight can be gained by accessing the page “List of bridge failures” on *Wikipedia* [1], where a large repository of news, photos and data is available. Analysing the period 1950 – 2021, the average number of collapses with casualties and injured is two per year, with an average of 36 killed and 38 injured every year, and those numbers are steadily increasing, mainly as a consequence of the increase in the number and age of bridges, but also due to the growth of vehicle weight and passages Figure 1.1.

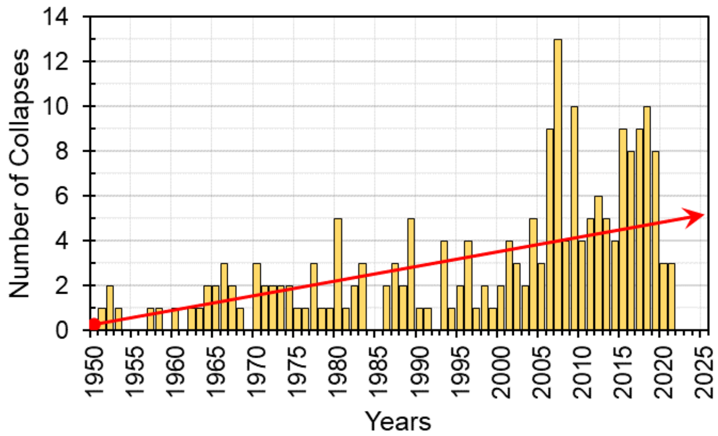

Figure 1.1. List of bridge failures (1950 - 2021) [1].

The change in vibration frequency caused by damage in structural elements has always attracted the interest of researchers as a viable tool for the serviceability assessment of structural parts. For instance, this technique can be used for the detection of localized cracks in metallic mechanical parts and the identification of damaged zones (in terms of position, extent, severity) in reinforced concrete bridges and buildings.

The object of this work concerns the detection of the variation of the main natural frequencies as a consequence of certain damage provided to a structure, whether it is local in the case of steel structures or diffused regarding structures made of concrete. The variation of the fundamental frequency is strictly related to the bending stiffness of the structure involved in the analysis. Thus, dealing with structures built in a lab environment (e.g. concrete beams, steel frames, bridge reproduction), it is even possible to assess the losses in terms of stiffness and some cases even the residual bending capacity. Concerning the tests performed on the bridges in the laboratory and then discussed in this work, each one is supported by an accurate Finite Element Model created with the software Strand7, able to simulate its real behaviour. In addition, all the numerical models will be available for further investigation and even the two small bridges will be part of a benchmark for algorithm and sensor networks validation.

1.2 Organization of the thesis

The thesis consists of the following five Chapters:

Chapter 1 - Introduction

Provides the introduction and the objectives of the research

Chapter 2 - State of the art of vibration-based damage identification

Presents a brief introduction to the Structural Health Monitoring (SHM) field and the approaches suggested for assessing the condition of existing structures. A state-of-the-art of the available vibration-based methods currently used for system identification and damage detection are also provided, including the concept of damage from the structural viewpoint.

Chapter 3 - Effect of damage on the natural frequencies

Consists of two sections. Firstly, the frequency decay due to local damage is discussed dealing with a steel-concrete composite deck built in the LISG lab, where the damage is simulated by cutting the main beams and restoring their strength through a bolted connection, and even the results of a small steel frame are discussed. Then, the problem of diffused damage is even considered for a set of concrete beams and a concrete deck in which the damage condition followed the crack pattern obtained from a progressive static load test, representing different severity of the damage. Some Finite Element models were created for simulating the structural behaviour concerning the concrete beams and the small bridge decks.

Chapter 4 - Assessment of the dynamic behaviour of existing bridges

Illustrates two existing bridges for which some dynamic investigations were performed for collecting their modal feature. The Annibaldi bridge is a pedestrian arch bridge that was tested during the “APESS” Summer school in Rome for the identification of its dynamic behaviour. The second bridge is the Bacchelli bridge in Bologna, which was tested for assessing its dynamic behaviour. Once the evaluation of the frequency associated with its first bending mode was obtained, two prototypes of a network were installed on the bridge for monitoring its evolution over time. Even the architecture of the network is included.

Chapter 5 - Conclusions

Presents an extended summary, a list of the main contributions of this work and the conclusions that can be derived from this study. Suggestions for future work are also pointed out.

References

2 State of the art of vibration-based damage identification

2.1 The need for the structural health monitoring

Today, where cost-effectiveness combined with life safety is a primary manufacturing goal, private owners and governments are currently looking for the best solution for monitoring their structures that can send some alerts in case of safety losses. Several engineering structures are now approaching or exceeding their initial design life. Despite their ageing and consequent damage accumulation, they are nevertheless in use for economic reasons. The proper health assessment of a structure becomes a critical task in such cases. In addition, a reliable Structural Health Monitoring (SHM) system is needed, especially after an exceptional event like earthquakes, or other natural phenomena, to assess the safety of existing buildings, mitigating economical losses through the proper plan for managing the interventions [2].

Time-based maintenance is now required for all the new structural systems, even if not always observed by the owners. It is the reason why the solution of operating only when and where is needed seems more affordable. Therefore, the use of a sensing device can be used for monitoring the condition of one structure, detecting the occurrence of damage as soon as possible, and preventing or warning the upcoming failure.

Worden & Dulieu-Barton [3] highlight four major interdisciplinary areas of primary interest for structural monitoring and damage assessment. First, the Structural Health Monitoring (SHM) [4], which originally concerned only aerospace and mechanical applications, then extended the field of operation to the civil structures. It usually includes networks of several sensors (e.g. accelerometers, optical fibres, etc.), that can online monitor one structure during its operative conditions. Second, Condition Monitoring (CM) [5] mainly deals with rotating machines, such as those used for power plants. Then, the Non-Destructive Evaluation (NDE) [6], on the other hand, is often used offline for quantifying the severity of one damage previously discovered using online sensors. Lastly, the Statistical Process Control (SPC) [7] is an experimental process-based approach that uses several kinds of sensors to monitor the process output, only. It aims at checking if one process is staying under control and, if not, what are the causes of the process changes, such as the occurrence of structural damage. The aforementioned areas of SHM, CM, NDE and SPC differ mainly in their application branches, but they exhibit common aspects, such as the use of sensors for acquiring some structural response features and appreciating the potential evolution of those responses over the time.

The structural monitoring regards both the material scale and the whole structural behaviour. In the first case, the properties of the materials are measured locally for understanding their health condition and detecting any kind of degradation. Then, good knowledge about the material can drive the following analyses dealing with the assessment of global behaviour. It is clear that when a large number of sensors is installed on a structure, the amount of information and their reliability are directly improved. On the other hand, the drawback of the use of many sensors is the management of the huge amount of data collected during the monitoring period in terms of transmission rate and storage capacity. Therefore, the deployment of monitoring systems goes beyond a simple collection of data and should take into account several tasks depending on the nature of the damage identification approach.

Worden et Al. identified two main categories [8], the Data-Driven approach based on the collected data only, and the Model-driven approach which is supported by a numerical model. Both the categories are outlined in Figure 2.1 and each step is further discussed.

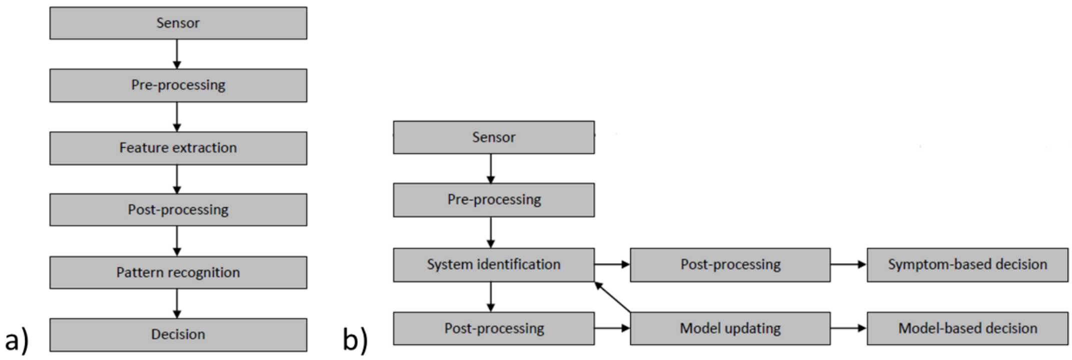

Figure 2.1. Flow charts for the Data-Driven Approach (a) and Model-Driven Approach (b). [8].

The model-driven approach considers the process of identifying damage as an inverse problem where the structure is modelled following the geometrical data and the physical laws. Then, changes in the measured data are related to the variation in the physical parameters through some system identification algorithms. On the other hand, the data-driven approach follows the pattern recognition theory where the measured data are classified according to the nature of the damage and then recognized by the algorithm. Anyway, some stages are commonly shared among the two procedures before aiming a decision.

Hereafter, all the main steps are discussed:

- **[Operational Condition]**: the design of the monitoring system has to be previously motivated by economical or life-safety reasons. Then, the characteristics of both operational and environmental conditions under which the system should be monitored have to be pointed out for finding any potential limitations and choosing the appropriate level of monitoring depending on the nature of the feature to be monitored. Moreover, the proper knowledge about the potential facility and the constraints on the observability of the system will dictate the scope and the return on investment that may be expected from any application.

- **[Sensor]:** the knowledge about the structures and the expected types of damage often drives the choice of the optimal type, position and number of sensors. One sensor basically provides electrical signals proportional to physical variables of interest recorded at a fixed sample rate depending on the nature of the data being measured. The location of sensors is often a very delicate task opting for limited sensors in critical points, rather than overdesigning the whole network. At this concern, *Staszewski et Al.* [9] discussed the sensor optimization approach to study the fail-safe distribution of sensors. Moreover, even the sensors of the networks have to be monitored against any sensor faults causing avoidable alarms or the whole stop of the network. One solution is to provide individual self-monitoring sensors [10] capable to assess their conditions and even the measurement uncertainties. Conversely, *Kramers* [11][12] suggested using sensors for mutually evaluating the conditions of the others. The choice of an appropriate experimental setup (e.g. type of sensors, sensor locations, frequency band) may even be driven by the evaluation of the structural response through the deployment of an a-priori numerical model based on the original drawings.
- **[Pre-Processing]:** it mainly encompasses three tasks operating on the raw data, directly. Firstly, the normalization stage separated changes in sensor reading caused by damage from those caused by varying operational and environmental conditions [13][14][15]. Secondly, the cleansing phase mainly involves the removal of noise, potential spikes or outliers contained in the input signals, preventing the transfer of those singularities to the next step. Lastly, the redundant data are discarded for decreasing the whole dimension of stored data. For instance, Fourier Spectra are much preferable rather than time series in terms of information content and size.
- **[Feature Extraction and Post-Processing]:** there exist many procedures for extracting damage-significant features from available data sets. Some of them may provide features either in a scalar form (amplitude) or vectorial form (frequency spectra). Three

types of approaches are currently used in practice, the first one concerns the simple correlation of extracted features with those associated with the first measurements tracking any potential changes. The other two approaches are based on the simulation of defects on existing structures measuring the corresponding response or the creation of supporting FE models validated experimentally, respectively. The number of features may be too large for being successfully processed in the pattern recognition stage. The reduction of the size of data is very delicate and needs a proper engineered judgement avoiding the discard of any relevant information. Basically, all the redundant data should be removed.

- **[Pattern Recognition]:** It mainly concerns the recognition of a certain damage condition and the corresponding severity evaluation. Worden pointed out three main categories of algorithms based on the type of diagnosis [8]. While Novel Detection algorithms are able only to discern if data become from the operating condition or not, the other two classes provide further information about damage location and severity using linear and nonlinear regression, often addressed by neural networks, or creating discrete class labels to be used to locate damage. The important limitation regarding the presence of noise is still valid for all the algorithms. Even small damages may produce weak signal variations that are easily detectable for noise-free data. On the contrary, noisy signals usually produce significant data fluctuations that may mask deviations due to damage, even in the case of severe damage.
- **[Decision]:** It is a matter of consideration of the pattern recognition outputs leading to the actions to be taken.

At the end of the process, the network has to be physically installed on a structure for monitoring purposes. Nowadays, despite the typical architecture being based on wired peripheral sensors connected to a centralized data controller, the recent trend is moving towards systems of low-cost wireless sensors for improving the spatial resolution of the acquired information avoiding the unnecessary costs related to the installation and maintenance of cables [16]. The applications of wireless networks were recently extended even concerning the measure of structural vibrations through the use of accelerometers, seismometers or optical fibres, properly handling the sampling rates and the transmission of data. In some applications, all the aforementioned steps are implemented onboard providing only the significant features capable to reduce the total amount of data to be stored. Typical algorithms to be used for the identification of systems and the detection of damage are discussed in the following, particularly concerning vibration-based methods.

2.2 Vibration-based system identification

The problem of predicting, or assessing, the static and dynamic behaviour of structures plays a significant role in the world of structural design, either for validating some hypothesis assumed during the design phase (e.g. constraints, stiffness values and mechanical properties) or assessing the conditions of existing buildings. More often, these activities need sophisticated mathematical models to accurately describe the real structural behaviour, although the correspondence among the data used for the verification and the actual structural parameters might not be checked in practice, especially those related to the dynamic behaviour. For this reason, many modal parameter estimation techniques have been developed over the years to estimate structural dynamic features through experimental tests. Earlier algorithms in the field of dynamic investigations were deployed for aeronautics and aerospace engineering [17] and then extended for civil engineering purposes. Several procedures were set out investigating buildings and bridges under an artificial excitation (input-output) or in their operational conditions (output-only).

2.2.1 Experimental and Operational Modal Analysis

The field of vibration-based system identification includes all the existing techniques able to estimate the key feature of the dynamic behaviour of a system, through the analytical or the experimental approach. The analytical approach is based on the full knowledge of the structure in terms of geometry, density distribution, materials and boundary conditions. Then, the eigenvalue problem is solved for the extraction of the modal parameter of the system. In contrast, from the experimental viewpoint, both the records of the dynamic excitation on the structure and the corresponding structural response are usually collected and then used for providing some Frequency Response Function suitable for assessing the dynamic feature of the system.

Even in the case of the experimental approach, a fundamental classification has to be stated distinguishing all the techniques in which both the excitation and the structural response are collected, and those that involve the measurement of the structural response, only. The first class of methods is named Experimental Modal Analysis (EMA), whereas the second is the so-called Operational Modal Analysis (OMA).

The EMA techniques are based on the use of special equipment (e.g. vibrodines, instrumented hammers, hydraulic or electrodynamic exciters) for applying an artificial excitation on the structures which allow to measure and control their motion. However, it usually needs the interruption of all the activities present in that structure for carrying out the test. This is true, especially for bridges that need to be closed to traffic during the test.

Typical sources of excitation for EMA investigation are signals containing a single frequency or signals containing a spectrum of frequencies. In particular, the signals belonging to the first category are of the sinusoidal type (swept sine, stepped sine), whereas the others can be grouped into 3 families: periodic (periodic chirp, burst chirp), non-periodic (pure random) and transient (impact) signals. In general, the criteria for classifying EMA methods are mainly based on the number of inputs and outputs: since the location of the source of excitation and the points where the response is measured can be single or multiple, the following four classes are identified:

- Single response due to a single excitation: Single-Input, Single-Output (SISO);
- Multiple responses due to a single excitation: Single-Input, Multiple-Output (SIMO);
- Multiple responses due to multiple forcings: Multiple-Input, Multiple-Output (MIMO);
- Single response due to multiple forcings: Multiple-Input Single-Output (MISO).

The first three methods are the most commonly used. Then, the dynamic behaviour of the structure can be described through a set of differential equations in the time domain or by a set of algebraic equations if the frequency domain is of concern.

Since the early ‘90s, dealing with the investigation of civil structures and infrastructures the scientific community began to take advantage of the vibration caused by the structural operative conditions (e.g. road and rail traffic) or those produced by natural sources of excitation (e.g. wind, earthquakes). In this case, the expression "Operational Modal Analysis" (OMA) is used to indicate a large number of identification procedures based on output-only information. Usually, It is assumed that the unknown input is well represented by white noise with Gaussian destruction at zero mean value. This hypothesis implies that the input is characterized by a flat spectrum in the range of frequencies of interest, consequently, all modes are excited and the output spectrum contains all the information relating to the structure.

As with traditional EMAs, the OMA procedure allows the evaluation of the natural frequencies, the modal shapes, and the damping ratio. However, since the input on the structure is unknown, or not measurable, the modal participation factors can not be calculated. On the other hand, without the use of any special equipment, the cost of the test decreases significantly and no interference with the operation of the structure is produced.
The theory of OMA is based on the following fundamental assumptions:

- **Linearity**: the system's response to a particular input is equal to the sum of the respective responses. (e.g. the principle of superposition of effects);
- **Stationarity**: the dynamic characteristics of the structure do not change over time;
- **Observability**: the data necessary to determine the dynamic characteristics of interest must be such as to be measured (hence the need to choose the measurement points wisely, avoiding placing the measurement instruments in those points, called "modal nodes", in which the observability of the modes is zero).

Thus, the considered systems are linear and stationary. It means that they are fully characterized by their impulse response h(t) or its equivalent in the frequency domain, the frequency response function H(f). In both cases, a proper design of the experimental setups can minimize the cost/benefit ratio in terms of the number of sensors involved in the test and the amount of information that it is possible to obtain from them. Indeed, a good setup needs information known a priori about the frequency range of interest, the expected modal shapes, and the accessibility of the measurement points. However, it is to mention that unfortunately the amount of sensors often depends only on the economic budget. Some solutions to this problem had been suggested by the research community that proposed the use of several sensor setups which are merged together in the data-processing phase when all the data have been collected [18][19][20]. The multi-setup approach involves the use of a small number of reference sensors in some key locations in common with all the setups, and a set of roving sensors which change their position in each setup increasing the spatial resolution of the collected data.

2.2.2 Methods for the dynamic identification of structures

The main difference among the existing procedures for the dynamic identification of structures is the classification in frequency-domain and time-domain methods. In the first case, the frequency-domain algorithms provide information about the dynamic behaviour of structures, in terms of natural frequencies, mode shapes and damping ratios by collecting and then processing some accelerometric signals recorded during the tests. Practical application dealing with frequency-domain methods involves the following methods:

- **Peak-Picking (PP):** [21] PP is the simplest way to evaluate modal parameters simply by investigating the harmonic content of accelerometric signals recorded on a structure. The method owes its name to the identification of the eigenfrequencies associated with peaks in the spectrum plot. The use of PP is suitable for structures characterized by low damping and well-separated modes. However, the peak selection may become a subjective task, especially if the spectra resolution is not fine enough, leading to an unreal estimation of the parameters. Felber developed the Hybrid Bridge Evaluation System [22], which concerns the assessment of the dynamic behaviour of bridges and other structures, mainly based on the PP method. Since the Power Spectral Density (PSD) of the recorded signals are usually collected in a matrix form, each column at each resonance frequency is used for the estimation of the modal shapes. Moreover, regarding the evaluation of structural damping, the so-called half-power bandwidth [23] may be used, even if its accuracy was proved to be not always satisfactory [24]. The same procedure may be applied more accurately in EMA contexts, where the Frequency Response Functions take place instead of the PSDs for the modal feature extraction [25].
- **Complex Mode Indication Function (CMIF):** [26] It is based on the diagonalization of the FRF matrix via Singular Value Decomposition (SVD), identifying the number of significant eigenvalues in each spectral line of the FRF matrix, solving the problem of multiple modes at the same frequency.
- **Circle-Fit method:** It is widely used in operating with the frequency domain in EMA contexts. The plot of Frequency Response Function curves in Nyquist's complex plane describes a circle in the vicinity of each natural frequency [25]. Then, the computation of the modal parameters (e.g. Natural frequencies, damping and mode shapes) becomes analytically possible starting from the linear interpolation of each experimental circle.
- **Frequency Domain Decomposition (FDD):** [27] FDD is the extension of the CMIF in the OMA framework. This approach applies the SVD to the matrix of output response power spectra instead of the FRF matrix. The application of FDD leads to the estimation of the modal frequencies and mode shapes, although no information about damping is

provided. The Enhanced Frequency Domain Decomposition (EFDD) was proposed by *Brincker et Al.* [28], improving the accuracy of frequency estimates and implementing the calculation of damping ratios. In this method, the Inverse Discrete Fourier Transform (IDFT) is performed at each peak of the PSD spectrum leading to the corresponding time series; then, the Damping is simply estimated via the logarithmic decrement applied to the normalized autocorrelation function of the resulting signal. Later, a new improvement of the FDD has been developed integrating the PSD with the information about spatial measurements [29]. Other frequency domain methods were presented in the work of *Gade et Al.* [30], while a detailed comparison among the performances of other methods was addressed by *Andersen et Al.* [31].

Conversely, starting in the 90s, even time-domain methods were proposed for investigating the dynamic behaviour of structures:

- **Natural excitation techniques (NExT):** Natural Excitation Technique is mainly based on the calculation of Auto- and Cross-correlation of structural random responses caused by ambient excitation. It is one of the earliest algorithms in the OMA field presented by *James et Al.* in the 1990s [32], which was picked up from the EMA practice and then extended to output-only modal analyses. Modal features are typically obtained employing other existing time-domain methods, such as Least Square Complex Estimation (LSCE) [33], Ibrahim Time Domain (ITD) [34], Polyreference Time Domain (PTD) [35], Eigensystem Realization Algorithm (ERA) [36], or simply obtaining the time series corresponding to each resonance through the Inverse Fourier Transform. It is to mention that, some of those techniques may be used either in the EMA or the OMA frameworks, even though OMA data have stochastic nature as opposed to the EMA ones.
- **Random decrement (RD):** Structural responses to ambient excitation are converted into Random Decrement functions, the computation of the corresponding correlation functions leads to the estimation of the modal feature of interest [37].
- **Second-Order Blind Identification method (SOBI):** SOBI is a method involving both the Blind Source Separation (BSS) [38] and the Principal Component Analysis (PCA). The combination of both the algorithms showed very effective performances in recovering unobserved source signals from their observed mixtures, even in the case of

civil structures [39]. SOBI uncouples an MDOF system into n-SDOF subsystems using the joint diagonalization procedure for computing an orthogonal matrix that diagonalizes a set of covariance matrices [40], highlighting how environmental variables influence the structural response.

- **p-LSCF:** The poly-reference Least Squares Complex Frequency Domain (p-LSCF), or PolyMAX, is a technique for the identification of the modal parameters via FRFs. In spite it has its origin in the frequency domain, *Peeters et Al.* [41] extended p-LSCF even to the operational case yielding clear stabilization diagrams and facilitating the pole-selection process that leads to the estimation of the mode shapes.

In the same period, other researchers laid the foundation for studying structural responses as stochastic processes, by processing the recorded time series for creating analytical models able to describe and interpret the experimental observations [42], [43]. It is the case of *Input-Output Models,* naming with *y(k)* the response at a certain time *k*, it is fully described by the linear combination of the previous responses $y(k-1),\ldots,y(k-n)$, previous inputs $u(k-1),\ldots,u(k-n)$, and the model error *e(k)* for taking into account a lack of accuracy of the model or potential errors affecting the measurements. Concerning a linear time-invariant system, the input and the output are described as follows :

$$y(k)=\alpha_1 y(k-1)+\ldots+\alpha_n y(k-n)+\beta_1 u(k-1)+\ldots+\beta_n u(k-n)+e(k) \tag{2.1}$$

Further models can be derived starting from the *Eqn.* (2.1), by making specific assumptions on the nature of the model error *e(k)* or by neglecting, or not, the input *u(k)*.
Autoregressive (AR) type models are currently suitable in the case of linear time-invariant systems (LTIs) excited by white noise. Typical AR-based methods for system identification are the ARMA models which become ARMAV when multiple inputs are involved [44]:

- **Auto-Regressive Moving Average (ARMA) and ARMAV methods:** The use of the Prediction Error Method (PEM) for ARMAV models was firstly proposed by *Andersen et Al.* [45]. In the time-domain context, PEM is a stochastic data-driven approach for estimating modal features by minimizing the difference between estimated and measured responses. The computational cost is not always affordable and even the solution may not converge because of the high nonlinearity of the algorithm, its sensitivity toward the initial values and the presence of noise. minimization is usually computationally onerous due to the high nonlinearity of the optimization algorithm from the time series.

By contrast, when other auxiliary variables appear in the model a *State-Space Model* is of concern and the equations governing the system become:

$$\begin{cases} x(k+1) = Ax(k) + Bu(k) + w(k) \\ y(k) = Cx(k) + Du(k) + v(k) \end{cases} \tag{2.2}$$

The vectors **u***(k)* and **y***(k)* are the measurements at time instant *k* of respectively the *m* inputs and *l* outputs of the process. The vector **x***(k)* is the state vector of the process at discrete time instant *k* and contains the numerical values of *n* states. These states do not necessarily have a direct physical interpretation but they have a conceptual relevance. Of course, if the system states would have some physical meaning, the similarity transformation of the state-space model to convert the states to physically meaningful ones always exist. **v***(k)* and **w***(k)* are unmeasurable vector signals, which are usually assumed as zero-mean, stationary, white noise vector sequences. Concerning the matrices:

- **A** is the system matrix describing the dynamics of the system as completely characterized by its eigenvalues;
- **B** is the input matrix which represents the linear transformation by which the deterministic inputs influence the next state;
- **C** is the output matrix that describes how the internal state is transferred to the outside world in the measurements **y***(k)*;
- **D** is called the direct feedthrough term. In continuous-time systems this term is most often 0, which is not the case in discrete-time systems due to the sampling;
- **Q**, **S**, and **R** are the covariance matrices of the noise sequences **w**(k) and **v**(k).

The matrix pair **A**-**C** is assumed to be observable, which implies that all modes in the system can be observed in the output **y***(k)* and can thus be identified. The matrix pair **A**-[**B Q**] is assumed to be controllable, which in turn implies that all modes of the system are excited by either the deterministic input **u***(k)* and/or the stochastic input **w***(k)*.

State-space models are usually adopted when the so-called Stochastic Subspace Identification (SSI) and the Eigensystem Realization Algorithm (ERA), in the stochastic and deterministic field, respectively, are of concern:

- **Stochastic Subspace Identification (SSI) methods:** SSI is a time-domain method that took its origin from the branch of mechanical engineering related to systems and controls. In particular, it was initially applied for the identification of the state-space matrices of systems by *Van Overschee et Al.* in the second 1990s [46] and then proposed in the field of civil and engineering structures by *De Roeck et Al.* [47][48][49] a few years later. The class of SSI methods is one of the most powerful in the output-only system identification [50], and even the most used. Typically, two main approaches may be implemented, named Covariance-Driven (Cov-SSI) and Data-Driven (DD-SSI). Conversely to EMA which uses the Impulse Response Functions, Cov-SSI forms a block-Hankel matrix based on the correlation data, then the Hankel matrix is properly weighted (e.g. Principal Component Analysis (PCA), Canonical Variant Analysis (CVA), Balanced Realization (BR) [51]), and lastly decomposed via SVD. On the other hand, while the Cov-SSI simply computes the covariances by the Fast Fourier Transform (FFT), DD-SSI involves the projection of future outputs based on the past ones via the QR decomposition of the Hankel matrix [48]. Thus, Cov-SSI is more computationally efficient than DD-SSI. Further discussion about the SSI method may be found in *Aoki et Al.* [52] or was provided by Scherrer [53] more recently.
- **Eigensystem Realization Algorithm (ERA):** ERA may be considered the deterministic counterpart of the SSI algorithm [36]. Based on the state-space representation of a system, the idea is to link the theoretical response with the measured via a transformation matrix: ERA forms the matrix containing all the structural responses, then the Hankel matrix is generated and processed with the SVD for the estimation of natural frequencies and mode shapes. *Benveniste et Al.* [54] proved the robustness of ERA even in the case of non-stationary inputs.

2.3 The concept of structural damage

The system behaviour is adversely modified after the occurrence of one damage, which is usually detected based on the comparison between two different states of the system, where the initial one is often the undamaged state. Dealing with structures, the damage is associated with changes in the material (e.g. ageing, deterioration), geometrical properties (e.g. occurrence of cracks), or changes in the boundary conditions. The damaged structure can still operate, but its safety could decrease dramatically, up to the state in which it is no longer acceptable to the user.

The main task of a monitoring system is to prevent this situation, by storing significant information for ensuring the safety of the monitored structure and possibly suggesting some retrofit intervention. Before proceeding to introduce the methods for the damage identification, according to *Worden & Farrar* [55] a list of the general principles that have driven their deployment over the years, has to be presented:

- **Axiom I:** All materials have inherent flaws or defects;
- **Axiom II:** The assessment of damage requires a comparison between two system states;
- **Axiom III:** Identifying the existence and location of damage can be done in an unsupervised learning mode, but identifying the type of damage present and the damage severity can generally only be done in a supervised learning mode;
- **Axiom IV:** Sensors cannot measure the damage. Feature extraction through signal processing and statistical classification is necessary to convert sensor data into damage information;
- **Axiom V:** The length- and time scales associated with damage initiation and evolution dictate the required properties of the SHM sensing system;
- **Axiom VI:** There is a trade-off between the sensitivity to damage of an algorithm and its noise rejection capability;
- **Axiom VII:** The size of damage that can be detected from changes in system dynamics is inversely proportional to the frequency range of excitation.

While most of the axioms don't need any further explanation, a few words have to be spent regarding axiom III: the supervised learning consists of regression analyses and group classifications applied when the data are available from both the undamaged and damaged states for a certain structure, whereas the unsupervised learning refers to methods that are used on data that do not contain instances from the damaged structure, by looking only at the statistical distribution of some measured, or derived, features (e.g. the outlier detection).
Concerning the damage state of a system, the following five levels of a hierarchical process lead to a full description of the damage [56]:

- **Detection:** Check the existence of damage in the structure;
- **Localisation:** Find the position of damage;

- **Classification:** Identify the type of damage, and possibly its nature;
- **Assessment:** Quantify the severity of the damage;
- **Prognosis:** Evaluate the residual life of the structure.

Each further step needs all the information previously collected in the lower levels and usually is not so easy to fulfil each task. An inverse problem approach is often chosen for damage identification purposes, in which the behaviour of a real structure is simulated through the corresponding numerical model. By applying linear algebra and optimization algorithms for calibrating some parameters to be assigned to the model, its behaviour matches to a given precision the real one [57]. Adversely, even a pattern recognition problem [58] can drive a damage detection process, where a large set of data has to be acquired for a normal condition of a structure forming a template to be compared with new sets of data to detect changes related to any particular damage condition or pattern (e.g. types, nature, location, extension, severity) and possibly their evolution over the time. The data are usually collected by using experimental tests or by performing several analyses on the numerical model of the structure. Both the experimental and the numerical approaches hide several drawbacks. Indeed, creating a reliable numerical model require a proper knowledge of building materials, especially if complex material constitutive models are involved, and anyway the simulation of a damaged condition is not easy. Numerical models inevitably include several simplifications that usually affect their accuracy, or use fine meshes, that are more accurate but highly time-consuming.

By contrast, from the experimental viewpoint, often it is not easy to explore all the potential configurations of damage or collect enough training data depending on the application (e.g. in the analysis of aircraft). The solution for this problem was suggested by *Worden et Al.* [59], [60] through the novelty detection technique, where the data are collected for the undamaged condition only and proper algorithms try to detect deviation from the normal trend. Moreover, the other approach may be the use of continuous sensors (e.g. Fiber Bragg Gratings - optical fibre [61], [62]) which record data in several locations simultaneously collecting more data than those associated with discrete sensors facilitating the detection of damage.

The current health evaluation of the structural conditions mainly involves two categories of inspection techniques. In the first case, classical Non-Destructive Evaluation procedures may be efficiently applied when the location of the damaged region over the whole structural element is a priori known, investigating the severity of the damage. Despite their effectiveness, they investigate small local areas and each of them needs to be readily accessible for the inspections. The necessity of the global condition assessment of large and complex structures motivated an increasing interest in the field of structural dynamic investigation, through vibration measurements.

2.4 Vibration-based damage detection methods

Regarding the detection of damage, all the techniques in which the measure of accelerations [63][64], strains [65] and displacements [66][67] are provided looking for the dynamic behaviour of a structure are usually named vibration-based methods. Normally, high sample rates in the range of 100-200 Hz are chosen for recording data and then downsampled up to 20-30 Hz reducing the size of the recorded data and reducing the measurement noise. These techniques are based on the idea that when damage occurs on a structural element, it alters the physical property of the whole structure, and mainly its stiffness and damping which are strictly correlated to the measured static and dynamic responses.

As explained by *Farrar et al.* [68], the development of vibration-based damage detection methods occurred concurrently with the evolution, miniaturization and cost reductions of Fast Fourier Transform (FFT) digital analysers and computing hardware. Since the 1970s, the first applications were found regarding offshore structures because of the complications in having access to the platforms for doing measurements and those related to the position of an occurred damage. Thus, some damage scenarios were simulated and a new methodology based on the correlation between the resonant frequency of the real structure and the ones provided by a numerical model was proposed [69]. However, changes in the level of the water surrounding the platform and the fluid contained in the tanks altered continuously the boundary conditions and the mass of the system, respectively, causing several problems in the interpretation of the acquired data. Thus, this solution was then discarded.

On the other hand, some years later, when the aerospace community started to develop the space shuttle, the use of vibration-based damage identification recovered its relevance, especially for identifying fatigue damage in components that were not easily accessible or coated with thermal protective layers preventing the use of traditional non-destructive tests. Hereafter, even other engineering community increased their interests in this field, applying vibration-based methods for monitoring either rotating machinery in the case of mechanical engineering [70][71] or bridges in the world of civil engineering [16][72].

Regarding the available damage detection methods, *Yan et Al.* [73] focused on the advancements provided by researchers in this field over the years, summing up all the existing techniques. Firstly, *Doebling et Al.* [74] and then, more recently, *Casas et Al.* [75][76] even provided an extended review in this area. Moreover, the researchers of the Los Alamos Lab produced a very interesting report collecting the existing literature on the SHM field [77]. Lastly, other important review papers on that topic were provided by *Fan et Al.* [78] and *Hou et Al.* [79] discussing the existing literature and comparing the performances of different techniques.

Most of those techniques are based on the identification of the modal properties of a structure in both normal and damaged conditions. Thus, the examination of the comparison among natural frequencies, damping ratios and modal shapes associated with each condition is able to provide both the position and the severity of damage especially if even the recordings of the input are available. Traditional vibration-based techniques, named Experimental Modal Analyses (EMA) methods involved the records of both the source of excitation applied to a structure and the subsequent structural response. Since the algorithms often required the computation of the transfer function between input and output, and the source of input needed to be completely known for having an accurate estimation of the modal parameters, no tests could be performed on the structures under their operational condition, in particular dealing with bridges. Indeed, modern damage detection methods began to be deployed for solving this problem. They usually are cheaper and feasible for online and cloud data processing, in particular, advanced output-only signal-processing techniques and artificial intelligence algorithms are used to obtain information about the structural conditions. One of the main problems that are still to be solved is the influence of the noise affecting each measure and even the consequences of the fluctuation of environmental and operational conditions (e.g. temperature, traffic) on the modal parameters. According to the previous section, two main classes of approaches exist in the damage identification field [80]: the data-driven approach [81] and the model-driven approach [82] where a FE numerical model or mathematical models are usually used for detecting damage. In what follows, most of the existing vibration-based procedures for detecting damages are introduced and then discussed:

- **Natural Frequency:** It is well known that since either structural stiffness or mass distribution are physical quantities directly involved in the calculation of natural frequencies, any change in mass or stiffness leads to variations of the natural frequency. Due to the ease of measuring natural frequencies, damage identification methods based on changes in natural frequencies are among the oldest ways used to identify the damage, because no more than one sensor is usually required to obtain the early fundamental frequencies. *Salawu* [83] provided a review of the existing techniques based on frequency shifts, which were used by some researchers for efficiently identifying damage in simple structures affected by single localized damage, without any information about its severity. More recently, *Benedetti et Al.* [84] reviewed the existing literature about the frequency decay in concrete beams related to the presence of damage. They proposed a simple formula capable to assess the loss of rigidity starting from the measure of the fundamental frequency, even considering the nonlinear behaviour of cracked beams due to the breathing crack phenomena. Another closed-form solution was developed by *Narkis* [85] to determine the inverse problem of the frequency shift of the position of a single crack in a simply supported beam. The suggested approach, involving the first two frequency shifts, was validated using FE analysis and did not exhibit any dependency on the shape or the severity of the damage. Researchers used to create curves investigating the influence of different damage locations on the lower natural modes, then they obtained the location of damage by intersecting those curves either dealing with beams [86] or frames [87], even if this approach was effective only for single damage scenario. Other examples are provided by *Vestroni et Al.* [88] and *Cerri et Al.* [89] concerning the use of natural frequency for detecting the position of damage or identifying a damaged area in simply supported beams. *Messina et Al.* introduced a detection method based on the combination of linearized sensitivity and the use of statistics [90]. The proposed approach named Multiple Damage Location Assurance Criterion (MDLAC) was able to locate even multiple damages, by measuring the variation of the principal natural frequencies. In general, frequency-based methods are suitable for detecting the presence of damage, but some limitations occur when even the location, the typology and the severity are of interest.

- **Modal Shapes:** Several methods in the existing literature allow the evaluation of the structural mode shapes by processing measured data [25]. Concerning the identification of damage, most of the algorithms are based on the curvature of the measured modal shapes, or even the mode shapes directly. It is the case of Modal Assurance Criterion (MAC) [91] and COordinate Modal Assurance Criterion (COMAC) [92] which are two common procedures for assessing the similarity of corresponding modal shapes in terms of modal coordinates. MAC and COMAC detect mode shape changes over the entire structure by taking advantage of the orthogonality of eigenvectors, indeed their values range between 0 and 1, they are closer to 1 as much as the two compared modes shapes are similar, whereas they assume lower values when the similarity decrease. Low values of MAC and COMAC may be indexes of damage. *Salawu and Williams* [93] proved the validity and the robustness of MAC in the case of a reinforced concrete bridge extracting the mode shapes before and after repair. The comparison of two mode-shapes through the MAC indexes is provided in Eqn. (2.3) where the vector $\{\varphi_i\}_j$ contains all the *j-th* modal components corresponding to the *i-th* mode:

$$MAC_{1,2} = \frac{\left|\left\{\varphi_1\right\}_m^T \left\{\varphi_2\right\}_n\right|^2}{\left(\left\{\varphi_1\right\}_m^T \left\{\varphi_1\right\}_m\right)\left(\left\{\varphi_2\right\}_n^T \left\{\varphi_2\right\}_n\right)} \tag{2.3}$$

Even the COMAC was validated through a similar test performed by *Fryba et Al.* [94], establishing the consistency between the undamaged and the repaired segment of a prestressed concrete bridge. It is simply based on the mode-shape vectors $\varphi_{i,j}^{D,U}$ corresponding to the Damaged (D) or the Undamaged state (U), according to the Eqn. (2.4), the COMAC calculation is straightforward:

$$COMAC_{m,n} = \frac{\left|\sum_{n=1}^{k} \varphi_{m,n}^{U} \varphi_{m,n}^{D}\right|^2}{\sum_{n=1}^{k} \left(\varphi_{m,n}^{U}\right)^2 \sum_{n=1}^{k} \left(\varphi_{m,n}^{D}\right)^2} \tag{2.4}$$

The main drawback is the need of extracting several mode shapes described by a large number of points. It means that even a large number of measurement points and sensors are required. Even if regarding beam-like structures COMAC is still susceptible to false-positive damage locations [95], it continues to be one of the most diffused techniques for detecting damage in civil structures [96]. Then, a solution for the problem of spatial resolution was found by *Khan et Al.* and *Gentile et Al.* who applied Laser Doppler Vibrometer (LDV) and Radar Interferometry (RI) techniques for identifying the structural modal shapes, allowing for a dense grid of measurements without the use of many sensors [67][97]. Concerning laboratory-scale structures, *Ren & De Roeck* [98] concluded that although methods based on modal shapes are effective with simulated data, they are difficult to apply to real structures due to noise, measurement errors, and the complexity of accurate modelling. Usually, modal-shapes-based methods are very effective when local damages are of concern, but only weak changes are evident for a diffused damage configuration. On the contrary, changes in natural frequencies appear more evident for both local and diffused damage. It is the reason why natural frequency and mode shape-based methods are often combined together improving the accuracy and reliability of the estimated damage features.

- **Modal Damping:** it is to mention that the attenuation of damping values can rise or fall depending on the type of damage. For example, dealing with concrete structures, *Yamaguchi et al.* [99] have observed that damping ratios are particularly sensitive to corrosion-induced damage. Furthermore, the occurrence of cracks usually increases the damping due to the internal friction, as well as nonlinear behaviour. However, some applications exist where damping doesn't show significant variation as *Casas and Aparicio* showed in their study [100]. Instead, concerning truss structures the removal of one element may reduce damping. *William & Salawu* [101] and *Farrar et al.* [102], firstly concluded that the high variability of the modal damping compromises its effectiveness as a reliable damage indicator. Dealing with bridges, even the vibration amplitudes and the operative conditions may affect the damping non linearly in the case of steel or composite decks. [103].
- **Modal Curvature:** The use of Finite Element models or analytical simulations enforced the feasibility of the mode-shape curvatures for detecting and localising damage through the Modal Curvature Method (MCM) [104]. Both the MCM and the updated variant of the Modal Curvature Squared Method deployed by *Ho and Ewins* [105] some years later on, lose their accuracy when a limited number of sensors is involved, or if potential errors occur in the curvature calculation through the central difference method applied to the mode shapes. Besides, some damage indexes were introduced for localizing damage, mainly comparing modal curvatures and the polynomial interpolation of the mode shapes [106]. *Wahab et Al.* firstly introduced the curvature damage factor as the difference in curvature before and after damage, averaged over a certain number of modes. Then, they validated their procedure by applying the curvature-based method to the Z-24 Bridge in Switzerland [107]. It is possible to conclude that since methods based on modal shapes contain more information about the damage, they appear more robust than frequency-based methods to detect, locate and calibrate damage even though less effective in case of diffused damage.

- **Modal Strain Energy:** Modal Strain Energy may be defined as the energy stored in a structure when it deforms in its mode shape pattern [108]. Consequently, having lower modal strains means a lower structural capability of storing energy due to loss in stiffness caused by potential damage. The modal strains energy method is based on the curve-fit interpolation of the experimental mode-shapes obtaining a continuous pattern of strains and the use of modal curvature for the computation of the following Damage Index:

$$\beta_{i,j} = \frac{\int_a^b \left(\varphi"_D\right)^2 dx + \int_0^L \left(\varphi"_D\right)^2 dx}{\int_a^b \left(\varphi"_U\right)^2 dx + \int_0^L \left(\varphi"_U\right)^2 dx} \cdot \frac{\int_0^L \left(\varphi"_U\right)^2 dx}{\int_0^L \left(\varphi"_D\right)^2 dx} \tag{2.5}$$

The damage feature $\beta_{i,j}$ concerns the *i-th* mode and the *j-th* position, while the curvature φ either for the undamaged (U) or the Damaged (D) conditions are integrated over the element length *L* and the element’s limits *a* and *b*, computing the strain energy for each interval. The method showed high sensitivity to local structural change [109], although its use involves only lower modes due to the difficulty of having strain responses for higher modes or the side-effects related to the central difference approximation and the presence of suspicious potential damage as an interpolation consequence. Later, the extension of this method was suggested by *Cornwell et Al.* [110] and *Duffey et Al.* [111] including 2D structures or axial and torsional responses, respectively. The ratio between the modal strain energy of one element and its kinetic energy was proposed by *Law et Al.* [112] introducing the Elemental Energy Quotient (EEQ). The normalization and the average over several modes of the difference between the undamaged and the damaged condition is used as an index of damage. The method is still valid even in the case of incomplete or noisy modal data.

- **Modal Flexibility Matrix:** Since 1994, when it was proposed by *Pandey et Al.* [113], Modal flexibility is currently used for detecting structural damage, even concerning bridges [114]. The method involves the calculation of the flexibility matrix of a structure inverting its stiffness matrix **K** and the modal information related to a set of lower modes is associated with a single damage feature only. The procedure provided very good results when compared to other modal based methods [115], especially if combined with the modal curvature method [116]. Its damage sensitiveness is mainly due to the mass-based mode shape normalization, which allows the flexibility matrix to portray the displacement pattern of the structure per unit force applied. However, in the case of ambient vibration, the lack of knowledge about the input data generates uncertainties in the normalization of experimental mode shapes and this affects the method's performance [117]. In general, when damage occurs to a structure the changes in the stiffness matrix are more critical than those observed in the mass matrix. However, if the damage severity is not significant enough, the method won't be able to locate the damage correctly, as demonstrated by *Farrar et Al.* in the case of the I-40 Rio Grande Bridge in America [118].

- **Frequency Response Function:** the use of Frequency Response Functions was one of the first methods for detecting damage because of its reliability and completeness in the results, although its effectiveness and accuracy strongly depend on the number of sensors and their position [119]. Despite, the method may be implemented by combining FRFs with analytical or numerical models, some researchers proposed some techniques based on the measure of the FRFs without any model, reducing thus the experimental burden by detecting damage within a substructure [120].
- **Nonlinear methods:** most of the algorithms involved in the SHM field are based on the hypothesis of linearity of the system and its response. However, when potential damage occurs to that system, it may change the whole behaviour even introducing sources of nonlinearity. Since the breathing crack phenomena or the hysteretic behaviour of the materials are often present in most real-world applications and since they produce highly non-linear structural responses, nonlinear damage detection methods arose over the years [121]. Later, several authors proposed nonlinear vibration features for identifying damage, but usually, the level of damping of the vibrating system and the lack of a pure harmonic structural excitation negatively affect their performance in detecting further nonlinearities (e.g. material, geometry, boundary conditions) [122]. It is the reason why, other authors further introduced the concept of Nonlinear FRF for studying that kind of problem, approaching nonlinear systems similarly to linear ones.
- **Time-domain methods**: Auto-Regressive (AR) models are mainly used for detecting damage [123][124] since they point out nonlinear behaviour in the vibration data by inducing changes in the residual errors and/or model parameters. However, they usually require multiple sensor locations and a proper normalization of the input data removing

the effect of any external condition (e.g. presence of traffic, temperature variations). Some models turned out extremely efficient for detecting changes either in mass or stiffness in a laboratory-controlled environment [125], but further real-world investigations are needed for assessing their robustness. Other AR-type models may involve both experimental data and numerical models [126] for comparing the actual dynamic behaviour with the expected one, including the probability density function of the involved parameters. Moreover, some researchers explored even the nonlinear field testing the effectiveness of nonlinear AR-type methods dealing with the damage assessment for a damaged plate made of aluminium [127].

- **Time-frequency methods:** over the years, those techniques showed their power in detecting damage, especially in the case of non-linear and non-stationary signals. Wavelet Analysis [128] and Hilbert-Huang Transform [129] are two of the most effective time-frequency techniques able to deeply explore the acquired signals uncovering their local content, conversely to the traditional analysis tools, such as FFT, that provide frequency components averaged over the whole signal length. In particular, the Hilbert-Huang transform combines the Empirical Mode Decomposition (EMD) with the Hilbert Spectrum (HS) as well as proposed by *Huang et Al.* [130]: EMD decomposes the input signal into a set of Intrinsic Mode Functions that are suitably processed by HT for determining the distribution of data in terms of energy, frequency and time, all together. *Douka and Hadjileontiadis* [131] investigated the free vibration problem of a beam with a breathing crack through the combination of EMD and HT fully describing the system nonlinearities. Another very effective method for detecting changes in the natural frequencies and the instant of time when they occur in a structure is the Random Decrement (RD) technique proposed by *Yang et Al.* [132].
- **Artificial neural network methods:** the idea of Artificial Neural Networks (ANN) is born from the study of the brain neuronal system in which billions of neurons are interconnected for processing the incoming information and producing corresponding actions [133]. Starting from an individual neuron up to the modern neural grids based on several layers of neurons, networks have been developed over the years, acquiring the learning capability. ANNs operate as black boxes for solving problems too complex to be modelled. Most of the operations are exploited in hidden layers, having some data as input and providing some results as the output. Concerning, the identification of

structural damage, Neural Networks need large datasets of measured responses, either for the damaged or the undamaged conditions, for training the algorithm to recognize structural damage [134]. Then, the trained network is tested by using additional datasets to check its performance. In the end, the NN will be able to efficiently locate damage, assess its severity, and in some cases, even the nature of the damage. *Yun and Bahng* [135] gave as NN input the data of measured modal features and created the first training dataset applying the Latin hypercube sampling. The algorithm was able to estimate structural stiffness parameters either dealing with frames or trusses, even considering an incomplete set of measurements. The validity of ANNs was proved even for detecting multiple faults in rotating machinery, so it may be promising even for civil structural purposes [136].

- **Genetic algorithm methods**: basically, Genetic Algorithms (GA) are heuristic approaches for searching optima inspired by Darwin's theory of natural evolution. Similar to genes in genetics, GA represents the parameters in a given problem by encoding them in a string. GAs mainly involve five steps [137]. Firstly, the initialization consists of a random generation of the population of coded strigs including all the potential parameters searching for the optimal solution. Second, during the selection phase, or reproduction, some strings are selected to breed a new generation based on a sort of fitness function measuring the quality of the represented solution. Third, the generation of the second population of solutions from those selected through the crossover and mutation phase, where pairs of "parent" solutions produce a new solution named "child" which typically shares many of the characteristics of both its "parents". From this step, the next generation is more consistent than the previous because only the best organisms from the first generation are selected for breeding and produce strings with increased average fitness. Lastly, after the heuristic phase in which special operators encourage the diversity of the population and prevent a premature convergence of the results, the final solution is achieved, satisfying a minimum criterion. The algorithm will stop when further iteration no longer produces better results and a maximum number of generations is reached. Concerning the identification of damage, the solution is achieved by breeding a set of parameters that include several variables, such as the geometrical and mechanical parameters of the elements. Then, the obtained parameter is assigned to the element of the FE model for getting the structural response and comparing it to the one measured experimentally. Dealing with damage detection on laboratory structures, *Hao and Xia* [138] successfully proved their proposed methodology based on a GA for minimizing an objective function created with the variation of all the modal features. Moreover, *Chou and Ghaboussi* [139] proved that the Implicit Redundant Representation Genetic Algorithm (IRRGA) introduced by *Raich et Al.* [140] performed better than original GAs, both for localizing and quantifying damage even without any numerical simulations.

- **Model Updating:** Actually, many damage detection techniques involve the existence of a numerical model of the structure to be updated in its properties (e.g. FE Stiffness, Material Density) matching the experimental outcomes (e.g. natural frequencies, mode shapes). *Mottershead et Al.* [141] widely reviewed the existing literature in the model updating field. Most of the methods are based on the iterative minimization of an objective function that is obtained by the equation of motion and assumes different formulations if the procedure deals with the matrix updating, the solution of an optima issue, the sensitivity problem, or if some artificial intelligence algorithm is involved [142]. Firstly, the matrix-update methods are based on an objective function named Residual Force Vector which is the result of some "perturbations" applied to all the matrices involved in the dynamic equilibrium. Then, some constraints for the preservation of the symmetry, the sparsity and the positivity of the Mass, Stiffness and Damping matrices are imposed before updating the physical coefficients included in those matrices for damage identification purposes [143]. Secondly, optimal matrix methods give the final solution by using a closed-form procedure based on an objective function J and a function of Lagrange multipliers-weighted constraints. Here, the updating phase doesn't involve directly the matrix coefficients because it is directly applied to the properties of the model elements. Some evidence of the method's efficiency was provided by *Liu* [144] concerning the minimization of the squared error function for locating damage and assessing its severity on a simulated plane truss. Further development of the optimal matrix deals with the minimization of the perturbation matrix rank [145], rather than its norm, for estimating mass, stiffness and damping perturbation matrices at the same time. Based on the same idea, *Doebling* [146] suggested a similar method with different constraints where the global stiffness matrix perturbation becomes a function of those parameters placed on the main diagonal of the stiffness perturbation matrix. However, the updated model might result physically unrealistic, thus expert judgement is often needed to be more coherent with reality.

Dealing with sensitivity-based methods, the minima of the objective function are achieved through the Newton-Raphson iteration using analytical or field data in the differentiation. Relevant evidence of the predicting goodness was provided by *Ricles et Al.* [147] and *Farhat et Al.* [148] in their study concerning plane truss cantilever beam, even when incomplete or noisy modal data are collected. Lastly, more recent techniques related to the use of eigenstructure assignment or the computational intelligence for detecting damage [142][149]. Even today, although the computing power is still increasing and handles larger and more complex structural models, the updating procedure may lead to infeasible computational costs depending on the accuracy of the initial model, the number of the updating parameters and the quality of experimental datasets [150]. Anyway, the problem of the non-uniqueness of the solution is an important point in the model updating field. Since existing structures consist of several continuous elements, there is an infinite number of degrees of freedom. Thus, there exist an infinite number of physically reasonable models with finite DOFs which adequately reflect the real structural behaviour [151], leading to no uniquely corrected dynamic model of the structure. Despite the existing updating techniques able to select the best number of parameters needed for properly calibrate a numerical model, the objective function used for updating numerical model involves natural frequency and modal shapes, only.

The damage sensitivity of many vibration-based features was investigated by *Moughty et Al.* [152] by processing the dataset acquired during the well-known progressive damage test of the S101 Bridge in Vienna. *Kaloop & Hu* [153] proved the damage responsiveness of the acceleration amplitude by applying pattern recognition to the vibration data recorded on the Chinese Yonghe Bridge. Previously, even other researchers conducted studies comparing the performances of the existing Modal-Based damage detection method applied to laboratory structures [154], civil and bridge-like structures [155], or by means of numerical simulations [156]. They observed the influence of the measurement noise affecting the capability of localizing damage of all the techniques, even reducing the reliability of some damage features. Moreover, most of those methods are based on the assumption of linear stationary structural vibration, which may not always be appropriate for real-world applications. In conclusion, natural frequencies can easily assess the presence of damage, but further spatial information provided by mode shapes and their derivatives is needed for localizing it.

3 Effect of damage on the natural frequencies

One of the fundamental tasks of the SHAPE project was the prediction of the strength and stiffness changes in bridges looking at frequency data. It drove all the experimental campaigns performed at the University of Bologna hereafter discussed. Dealing with bridges, there are plenty of damage scenarios to be considered during the assessment of their structural conditions, such as the corrosion of the steel rebars or prestressing wires, the effect of fatigue on the steel details or the crack propagation. Each of them needs a deep and wide knowledge of several topics and huge availability of specimens for exploring experimentally their influence on the structural behaviour. It is the reason why the present research preliminary involves the design, the calculations and the execution of the small replica of two existing bridges, creating a laboratory benchmark for studying several damage conditions and for the validation of future system identification or damage detection algorithms simply by the comparison of the outcomes with those provided in this work. Even the numerical model will be the potential objective of future investigation and upgrades. Then, the following sections address the assessment of their structural behaviour. Furthermore, the testing of a set of concrete beams and a small steel frame will be illustrated and the corresponding outcomes discussed.

3.1 Design, construction and geometry of the small bridges

3.1.1 Building materials and their properties.

The strength classes and mechanical properties of the materials employed in the construction are summarized in Table 3.1. The concrete was obtained with 350 kg/m^3 of Portland cement CEM II/A-LL 42.5R, a water-cement ratio varying from 0.53 to 0.59, sand in the range 0.1-1 mm and gravel in the range 5-15 mm complying with a granulometric curve for thin sections. In agreement with the European Standard EN 206 [157], the poured concrete achieved the strength class C28/35 with a density ρ equal to 2300 kg/m^3. The cubic compressive strength R_{ck} determined by laboratory tests held 38 MPa. The density was derived by weighing cubic samples. Then, ultrasonic tests were performed on the same specimens to obtain an experimental value of the dynamic elastic modulus. The obtained experimental value of the dynamic elastic modulus is 36 GPa. According to the ratio between the static and dynamic moduli approximately equal to 0.9 [158][159], this value was reduced to 32 GPa, even consistent with the Italian Standard [160].

Table 3.1. Mechanical properties of the construction materials employed in the erection of the bridge and applied to the FE model of the bridge.

Material	Strength Class	Thickness [mm]	Elastic Modulus [MPa]	Density [kg/m^3]
Structural Steel[1]	S 275	Various	210000	7860
Concrete[2]	C 28/35	Various	32000	2400*
Steel Rebar	B 450 C	Ø 8-12-16	210000	7860
Corrugated Steel[1]	S 275	0.8	210000	7860
Neoprene Sheet	Shore A	15	2.5	1270
Asphalt	-	25	-	800

[1] European Standard EN 10025 and EN 10219
(Committee, n.d.; European Technical Committee, n.d.)
[2] European Standard EN 206 and UNI-EN 11104 [157]
[*] The density includes roughly 100 kg/m^3 of steel reinforcement.

Concerning the rubber bearings, the standards dealing with bridge bearing devices [163] and the neoprene rubber datasheet [164] suggest the calculation of the axial stiffness of a neoprene pad as a function of the rubber shear modulus G, the shape factor S of the pad, and the bearing stress σ_V leading to the Eq. (3.1):

$$k_V = 20GS + 3\sigma_V \tag{3.1}$$

According to the manufacturing company the values of G and S hold 0.9 MPa and 2.5, respectively. By considering the rubber incompressibility, the straight calculation suggested by [163] led to a first approximation of the pad axial stiffness k_V equal to $1.5 \cdot 10^5$ kN/m and $7.2 \cdot 10^4$ kN/m corresponding respectively to the rubber pads below the concrete beams and steel beams of the two bridges. These values will be slightly updated in the following matching the experimental data.

3.1.2 Foundations and Abutments

The two bridge decks were designed to be built on the ground and then placed above the abutments after the concrete curing by lifting them via four steel hooks. Two independent abutments made of reinforced concrete stand over the same foundation reducing the cost of the formworks and avoiding any potential interaction between the two decks.

A total of eighteen Tubfix piles complete the layout presented in Figure 3.1, which represents even the print of the foundations. Each one is a steel ø 127 mm tube-shaped pile with a thickness of 5 mm (Figure 3.2), forming a ø 200 mm pile, which increases its diameter to 250 mm for the last 1 m near the tip.

Concerning the length of the piles (A), 7 m is the length L of the piles below each foundation providing an efficient restraint to the ground increasing the whole stiffness; whereas the remaining piles (B) are 11 m long and operate as an anchoring system for exerting the load on the two bridges through the loading setup discussed later. While piles (A) are mainly dedicated to the structural stiffness increase, the others need to be longer because are subjected to an extraction force transmitted by the loading system.

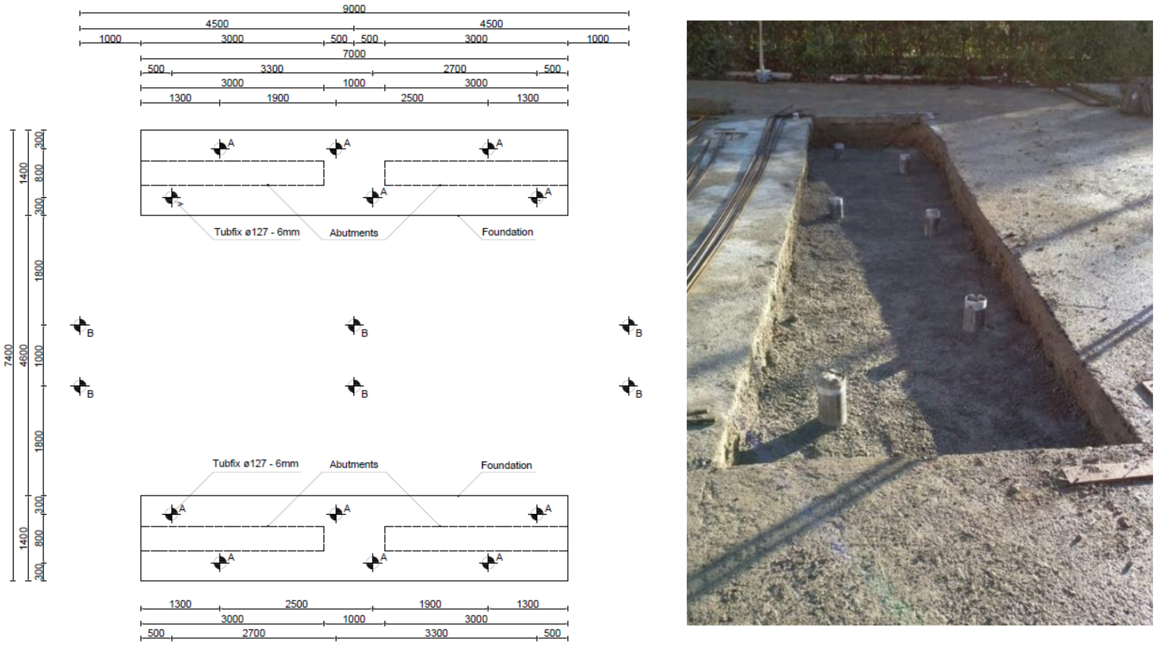

Figure 3.1. The layout of the piles and the foundations.

Figure 3.2. Tubfix piles ø127mm and the hole in the ground ø200.

Given the raft base area A_f = 9.8 m^2, the pile base area A_p = 0.05 m^2 of the foundation and an average undrained soil cohesion c_u equal to 50 kPa (clay soil type), the approximate bearing capacity of a Pile (A), Pile (B) and the withstanding Soil are computed trough the *α-Method* in Eqs. (3.2)(3.3) and the Terzaghi formula in Eq.(3.4), respectively [165]:

$$Q_{\lim,P}(A) = \pi\alpha c_u \cdot \sum D_i L + A_p\left(9 \cdot c_u + \gamma L\right) \tag{3.2}$$
$$= \pi \cdot 0.7 \cdot 50 \cdot (0.2 \cdot 6 + 0.25 \cdot 1) + 0.05 \cdot \left(9 \cdot 50 + 10 \cdot 7\right) = 185\,kN$$

$$Q_{\lim,P}(B) = \pi\alpha c_u \cdot \sum D_i L = \pi \cdot 0.7 \cdot 50 \cdot \left(0.2 \cdot 10 + 0.25 \cdot 1\right) = 247\,kN \tag{3.3}$$

$$Q_{\lim,S} = N_c \cdot c_u A_f = 5.14 \cdot 50 \cdot 9.8 = 2518\,kN \tag{3.4}$$

Note that piles (A) are subjected to loads of the concrete works, whereas piles (B) are subjected to an extraction force, only. Thus, the bearing capacity at the base of piles (B) is neglected. Moreover, the coefficient α is usually adopted for cohesive soils and directly depends on the cohesion values, thus considering the present conditions α = 0.7.
Considering the property safety factor γ_R = 2.3 [160], according to the layout illustrated in Figure 3.1, the overall design bearing capacity of two pairs of piles (B) leads to the maximum design force to be exerted on the two bridges equal to 429 kN. Instead, the total bearing capacity of the raft foundation is 1555 kN including the bearing capacity of six piles (A) and the net base area of the foundation.
The maximum design force applied on the two bridges is then combined with the total weight of the concrete works, roughly equal to 680 kN, and the self-weights of the two decks equal to 80 kN and 60 kN, respectively for the concrete and the composite steel decks, for the calculation of the loads acting on the two foundations (roughly equal to 910 kN).
Moving to the design of the abutments, while their width was chosen as equal to the width of each deck (w = 3 m), the height and thickness were respectively set equal to 1.5 m and 0.4 m for having a value of their bending stiffness large enough to avoid any potential interaction during the experimental campaign performed on the two decks. Concerning the amount of steel reinforcement, the limited actions and the size of the resisting elements motivated the minimum area of steel according to the Italian Standards applicable at the time of construction [160]. The layout of the steel rebars is illustrated in Figure 3.3.

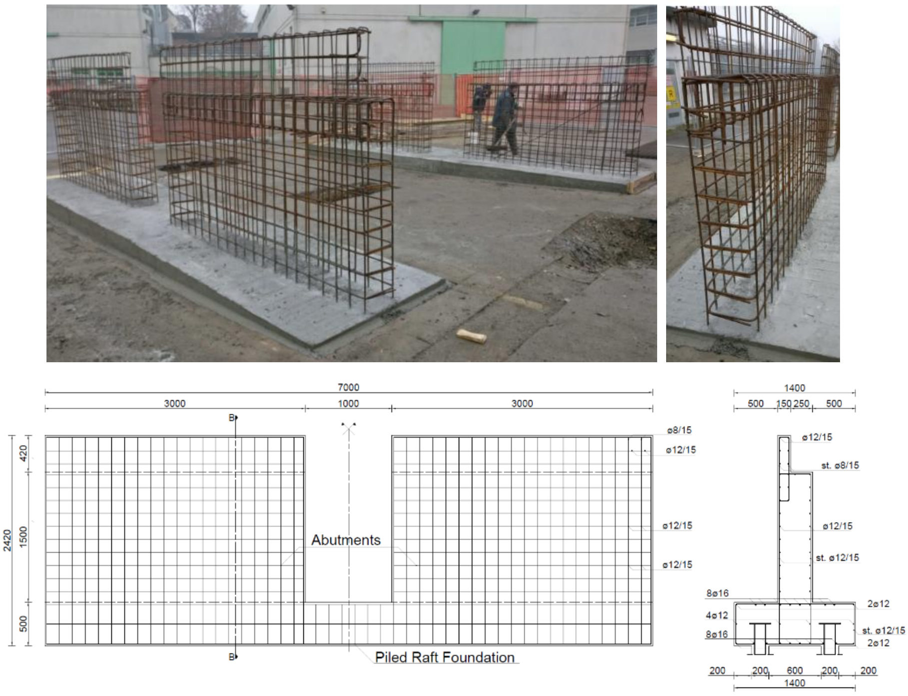

Figure 3.3. Front view, vertical section and steel reinforcements of the abutments (Picture and Drawings).

3.1.3 Steel-concrete composite bridge deck

One of the purposes of this work deal with the investigation of a small replica of one existing bridge crossing the A14 highway in Italy, near the city of Bologna (Figure 3.4). The scaling phase involved only the geometrical dimension, whereas the properties of the materials were selected according to the common design practice.

Figure 3.4. The bridge overpass on the A14 highway (on the left) and the scaled model under investigation (on the right).

The model was designed as a tool for checking the ability of dynamic tests in estimating the influence of localized damage states on structural performances. The bridge is composed of a composite deck and the two concrete walls raising from a piled raft foundation are illustrated in the previous section.

The deck concrete slab is 6000 mm long and 3000 mm wide. A 55 mm tall stay-in-place zinc-coated structural corrugated steel sheet formwork was adopted to contain the concrete pouring, leading to an average total slab thickness of 130 mm. The slab reinforcement was set out with a bidirectional ø6/100 mm steel mesh and ø8 transversal steel bars placed every 200 mm inside the ribs of the corrugated steel sheet. After the bridge completion, the concrete slab was finished with 25 mm of asphalt (Figure 3.5, Figure 3.6).

The steel braced framework illustrated in Figure 3.7 is fully made of steel S275 and includes three IPE 300 girders, two secondary cross girders made by coupling two UNP 140 and six L 35x4 equal leg angles as cross bracings. Two IPE 300 girders were used as head beams resting over the deck bearings laying on the piers according to the longitudinal section of the bridge shown in Figure 3.5. The steel framework and the concrete deck are connected by rows of Nelson's shear studs welded every 100 mm over the beam upper flanges.

The bridge deck is sustained by six 15 mm neoprene bearings, posed under the head beams centred to the axis line of the main beams.

The bearing capacity of the bridge deck is computed analytically according to the *Italian National Standards* [160], leading to the values of approximately 4200 kNm and 590 kN respectively for the resisting bending moment and the resistance in shear. Then, the whole deck has been properly designed including the verification of welded and bolted connections and the other structural details.

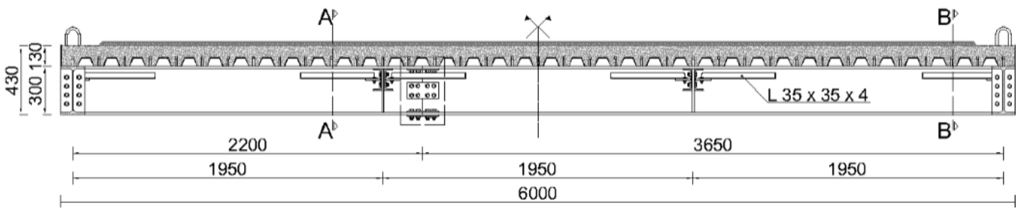

Figure 3.5. Longitudinal vertical section C-C of the steel deck.

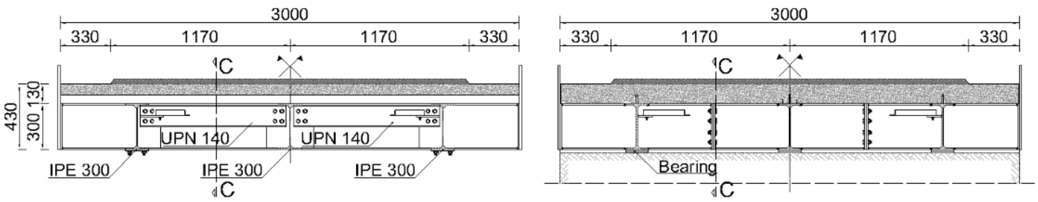

Figure 3.6. Transverse vertical sections A-A and B-B of the steel deck.

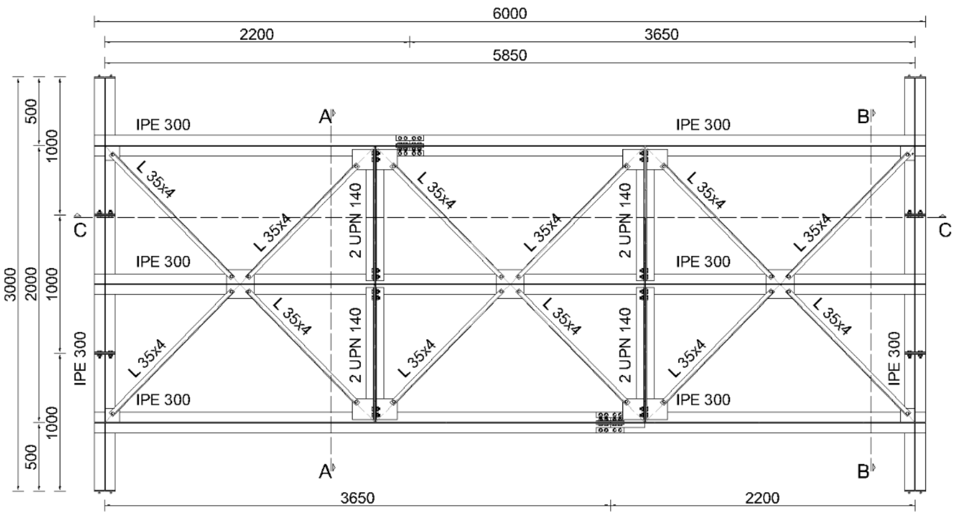

Figure 3.7. Plan view of the steel grillage of the deck.

During the construction phase and the deck casting operation, the structure was not propped. For this reason, the concrete slab shows a non-uniform thickness over its surface due to the uneven deflection of the steel elements. As usual, the connection among the main girders and the two head beams was executed with welded joints, while bolted connections linked the secondary cross girders and the bracings together to the main beams.

Besides, two vertical cuts have been provided at a fixed length of the two outer beams of the bridge model, able to simulate the presence of damage. From the mechanical point of view, the two cuts strongly reduced both the stiffness and the load-carrying capacity of the bridge, thus the two bolted twin plate splices illustrated in Figure 3.8 were properly designed to fully restore the original bending and shear capacity of the solid beams. These joints were introduced to obtain full continuity, flange break or beam break in one or two beams of the bridge steel framework, encompassing finally five different simulated damage states.

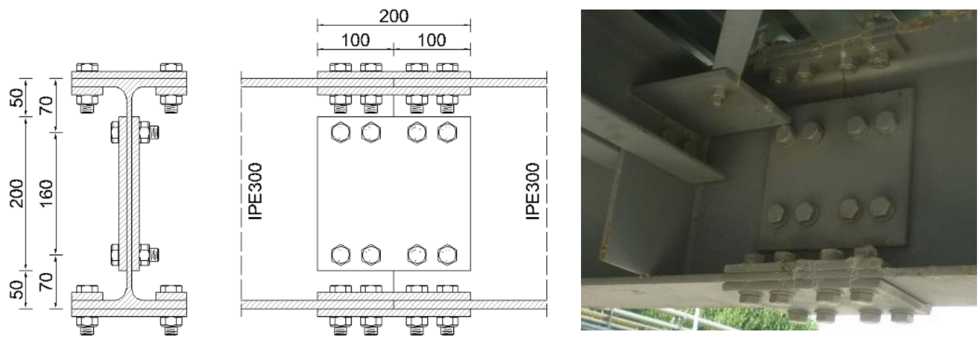

Figure 3.8. Bolted twin plate splices at one-third of the main beam length.

3.1.4 Concrete bridge deck

Another purpose of this work deal with the investigation of a small replica of one existing bridge made of concrete placed near the city of Bologna, both illustrated in Figure 3.9. The material properties were selected according to the material classes commonly used in bridge design practice. Although, the only difference consists in the nature of the materials: the beams of the existing bridge are made of high-strength concrete and reinforced with prestressing steel cables, whereas the laboratory sample used only ordinary steel and concrete (Section 3.1.1)

Figure 3.9. The existing bridge (on the left) and the investigated scaled model (on the right).

The details about the geometry of the model bridge and the experimental setup are here presented. The bridge is laying on the two abutments on the piled raft foundations, both illustrated in Section 3.1.2. The cross-section of the deck is composed of a 6000x3000x100 mm^3 concrete slab and four hollow rectangular girders. Two 200x400 mm rectangular beams were used as head beams resting over the deck bearings laying on the piers. The longitudinal section of the bridge is shown in Figure 3.10. Ten ø16 bars were placed on the lower layer of the beams and four ø12 bars at the top. The slab reinforcement was set out with a bidirectional ø6/100 mm steel mesh. After the bridge completion, the concrete slab was finished with 25 mm of asphalt Figure 3.11. Finally, the bridge deck is sustained by eight 15 mm neoprene pads, posed below the head beams centred to the axis line of the main beams Figure 3.12.
The bearing capacity of the bridge deck is computed analytically according to the *Italian National Standards* [160], leading to the values of approximately 1300 kNm and 800 kN respectively for the resisting bending moment and the resistance in shear. The experimental values obtained in the following section will be higher than those here estimated because of the influence of the safety factors.

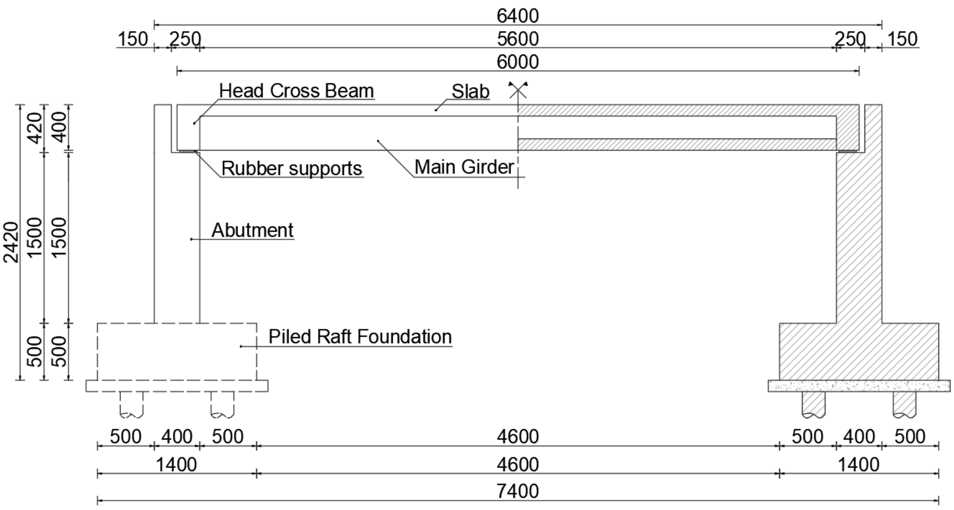

Figure 3.10. Longitudinal vertical section of the concrete deck.

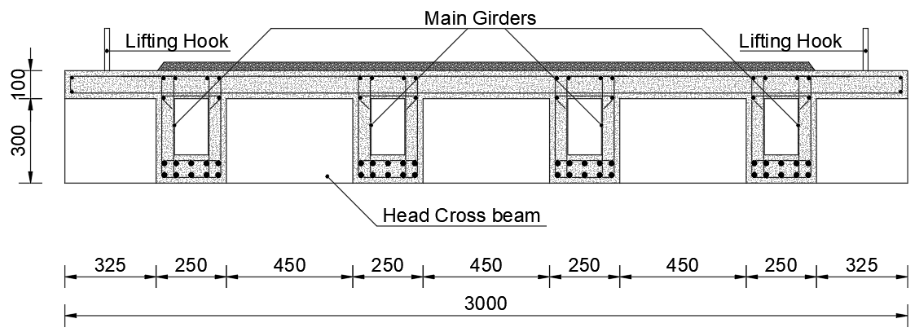

Figure 3.11. Transverse vertical section of the concrete deck.

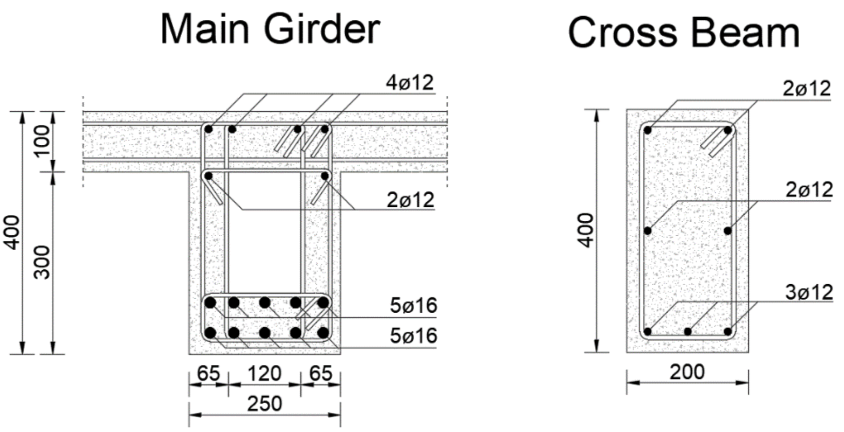

Figure 3.12. The “U-Shape” girder cross-section (on the left) and the head beam cross-section (on the right).

3.1.5 Loading System

Part of this thesis research deals with the assessment of the static and dynamic behaviour of the two aforementioned laboratory bridge decks. Static load tests have been used for validating the mechanical properties assigned to the numerical models of the two decks and the experimental outcomes. The whole setup of the loading test illustrated in Figure 3.13 and Figure 3.14 has been properly designed including the verification of welded and bolted connections and the other structural details.

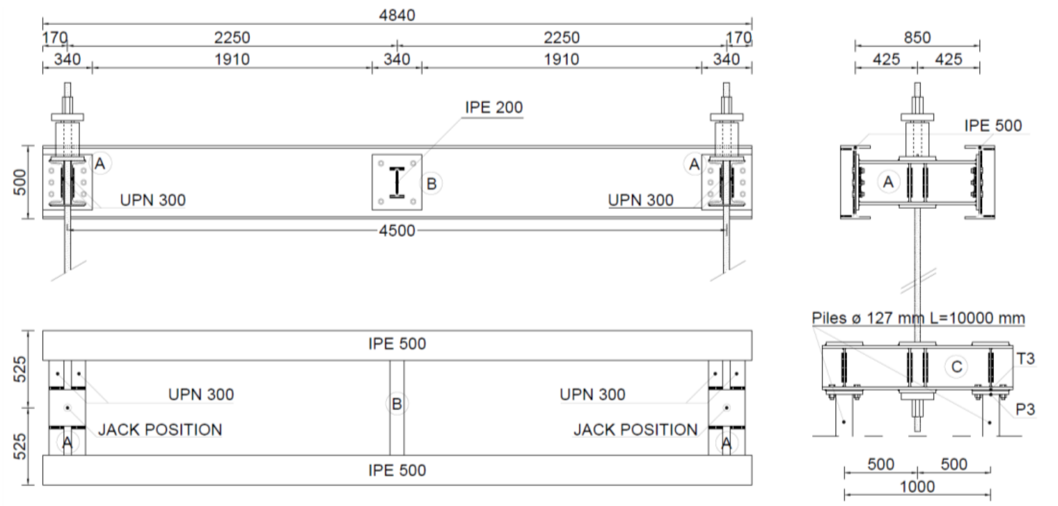

Figure 3.13. Drawings of the loading system.

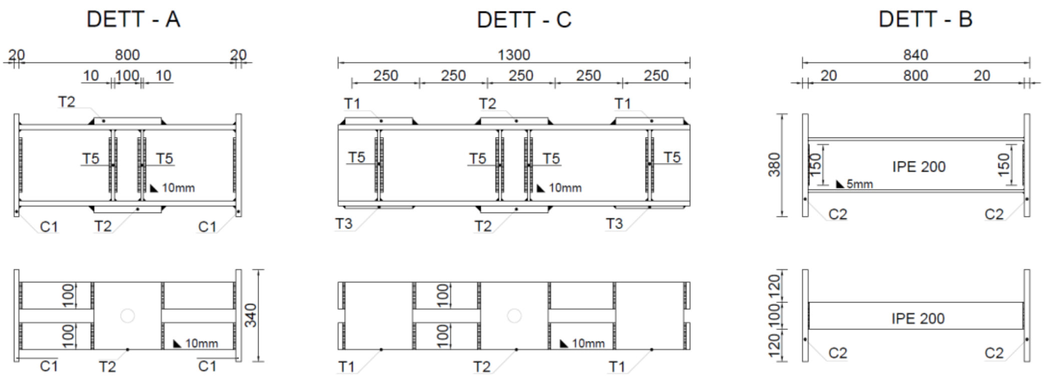

Figure 3.14. Details for the loading system.

Two pairs of UPN 300 steel profiles were bolted to two IPE 500 steel beams with six bolts M22 cl.8.8 creating the loading system. Each welding bead is 10 mm wide verifying the rules provided by the *Italian National Standards* [160]. Two ø36 mm Dywidag rods running inside the slots of the UPN 300 pairs were used in transferring the applied load to the anchoring system for which the reactions were provided by two pairs of Tubfix piles with their bearing capacity computed in Section 3.1.2.

Lastly, two jacks with a capacity of 667 kN are used for exerting the load on the Dywidag rods, and consequently to the bridge decks. act on the beam' ends using Dywidag rods with a diameter of 36 mm running inside the slots of the UPN 300 pairs.

The applied load acted directly on each of the main girders, thus the loading beam has been properly dimensioned against the internal actions corresponding to each setup by fixing the allowable deflection under the maximum load such that its influence on the force distribution over the bridge decks could be disregarded. Even the beams anchored to the piles (Figure 3.14) followed the same design criteria.

3.2 Local damage: damage identification and localization

The prediction of the evolving strength and the structural integrity of strategic structures, such as hospitals, rescue buildings or bridges, has attracted the interest of many researchers. Their performance can be shattered by environmental and accidental actions and therefore because of avoiding the suspension of the service state, early detection of the damaged condition is mandatory.

In the last years, the collection and the processing of the ambient vibrations became one of the main experimental methods for a global condition assessment of structures through the identification of their dynamic behaviour.

Usually, global modal parameters are functions of the physical properties of the structure. Thus, changes in the physical properties of the structure induce variation in the modal parameters. The topic is still the subject of continuous research [166]–[169] aiming at the characterization of the damages in terms of position and intensity. Many tests were carried out almost twenty years ago on full-scale structures and created a solid baseline for the research in the fields of Vibration-Based Structural Health Monitoring (VBSHM) and Damage Detection (VBDD) [170]–[174]. The data collected performing those tests are often used as a benchmark for developing new algorithms or comparing the detection capability and the robustness of different damage indicators [175].

Lauzon et Al. [176] presented an investigation similar to the one shown in this section but acting progressively only on one beam. *Zhou & Biegalski* [177] studied a real damaged bridge with a damage scenario very similar to the one used in the model bridge, but no dynamic investigation was performed. *Hagani et Al.* [178] listed several damage patches detected in real bridges but any link with the change of dynamic properties was set out. *Chajes et Al.* [179] detailed the damage detected in the I-95 Delaware bridge and the restoration works, but information concerning the bridge stiffness variation is missing.

However, the cited experiments allowed only episodic data collection not linked with the loading level experienced by the bridge. Laboratory scaled models can be loaded and dynamically investigated repeatedly at different load levels, ages, corrosion extent, etc., building so representative correlations of the parameters describing the state, and allowing for future further checks of the extracted data. Therefore the present section aims to evaluate how local damages, increasing in their severity, influence the natural frequency of a bridge, or the modal features of a small steel frame.

3.2.1 Investigation of the composite steel-concrete bridge deck

The bridge model was set out to study the effect of local damages on the fundamental natural frequency, estimating the loss of stiffness of the bridge by looking at the frequency decay due to the presence of damage. The laboratory campaign consisted of both static 4 Point Bending Tests (4PBT) and dynamic tests for the material property characterization, and then a bridge numeric counterpart is used for the experimental data validation.

Static load test: 4 Point Bending Test (4PBT)

The loading system illustrated in Section 3.1.5 was adopted for performing a static load test of the composite steel deck (Figure 3.15). The load acted directly on each of the three main girders thanks to the six loading points illustrated in Figure 3.16.

Figure 3.15. Static load test setup: on the left is shown the static loading system; on the right is visible the data acquisition system.

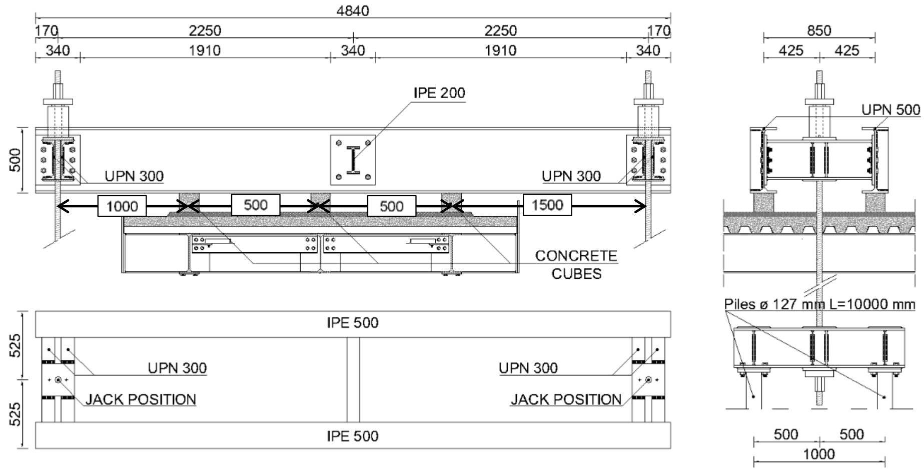

Figure 3.16. Drawings of the setup of the loading system.

The model bridge was firstly loaded up to 120 kN staying in the linear-elastic stress range of the materials and avoiding any yielding of the steel members. Thus, the linear elastic behaviour allowed to estimate the force exerted by each loading point simply by solving the static scheme of the problem. By considering the huge stiffness of the loading beam, the force acting on each concrete cube (Figure 3.16) can be computed following the equilibrium equations governing the whole loading system. Because of the eccentric loading setup (Figure 3.16), the forces exerted on the loading points were different.

In particular, for each load step, the forces computed at each pair of concrete cubes resulted in 21%, 33% and 46% of the total applied load P for the beams instrumented with the Linear Variable Differential Transducers (LVDTs) 1, 2 and 3 respectively. In particular, three sets of ten load cycles were applied to the bridge in the range of 0-45 kN, 0-90 kN and 0-140 kN respectively.

During the experimental campaign, a total of 5 LDTVs recorded the displacements at the five marked positions in Figure 3.17, while a digital manometer measured the oil pressure provided to the two hollow jacks. While three LVDTs (1 to 3) with a measuring range of 50 mm were placed below the mid-span of the main beams (red triangles in Figure 3.17), the last two were placed near the supports measuring the deflection of the elastic bearings. The two LVDTs “s01” and “s02” were selected with a range of 20 mm to improve the accuracy of the measure. In conclusion, the bridge elastic behaviour is described by five load-displacement curves of five reference points.

Solving the equilibrium of the composite cross-section and following the guidelines introduced in Section 3.1.1, the initial bending and torsional rigidities of the bridge and the axial stiffness of the rubber pads were analytically computed and then compared with the values inferred from the two experimental curves. The analytical bridge rigidity EJ_0 matched exactly with $1.70 \cdot 10^5$ kNm^2, the one reckoned from the mid-span load-displacement curve, while the torsional rigidity Gk_t resulted equal to $4.27 \cdot 10^4$ kNm. Concerning the stiffness of the rubber pad, the comparison with the support load-displacement curves proved a biased estimation of the neoprene axial stiffness: the backhand stiffness calculation suggested a proper value for the axial stiffness equal to $6.5 \cdot 10^4$ kN/m. This means that the lateral confinement exerted by the steel surfaces on a single pad was lower than the one considered by the Standards, and highlights the prerequisite of executing load tests for assessing the correct support stiffness, to be included in the dynamic calculations.

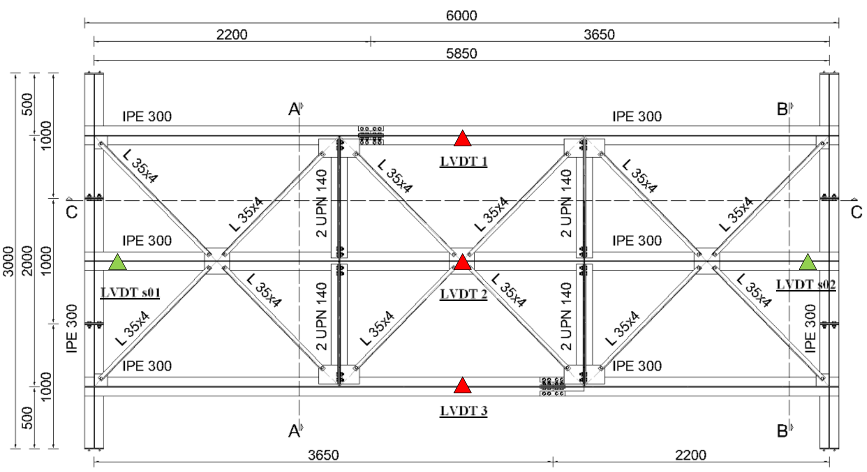

Figure 3.17. Plan layout of the LVDTs adopted for the static load test (measurement range: red marks 0-50 mm, green marks 0-20 mm).

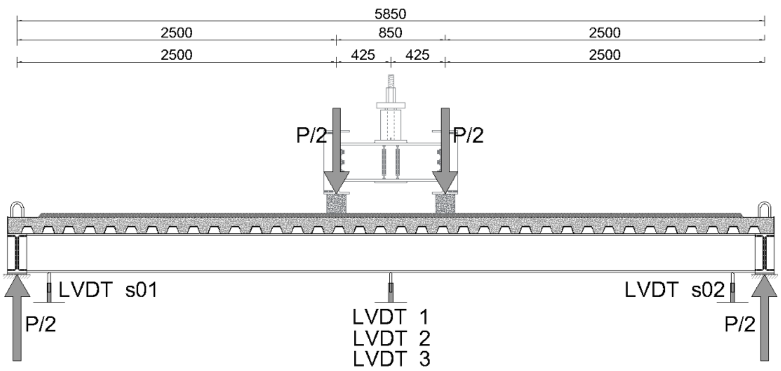

Figure 3.18. Setup for the static test.

Dynamic Identification of the bridge model

Concerning the dynamic investigation, AV and RW excitations were recorded for 30 minutes and 8 minutes respectively, to ensure an acquisition window of at least 2000 times the fundamental period of the bridge. Then, one rubber hammer was used to perform HH excitation in different positions, triggering in this way a large number of the main dynamic modes. Finally, the time series were processed either considering the total length of the signal or processing the acceleration produced by each hammer hit singularly. Since this study is devoted to investigating the influence of damage on the bending stiffness of the bridge and no significant difference was observed among the frequencies extracted from all the used excitation methods, only the lower main frequencies were extracted and their experimental values were defined by the average of all the completed tests.

The accelerations were measured at a sampling rate of 2000 Hz with a set of eight tri-axial Sensr CX-1 mems accelerometers arranged according to the setup of Figure 3.19 [180].

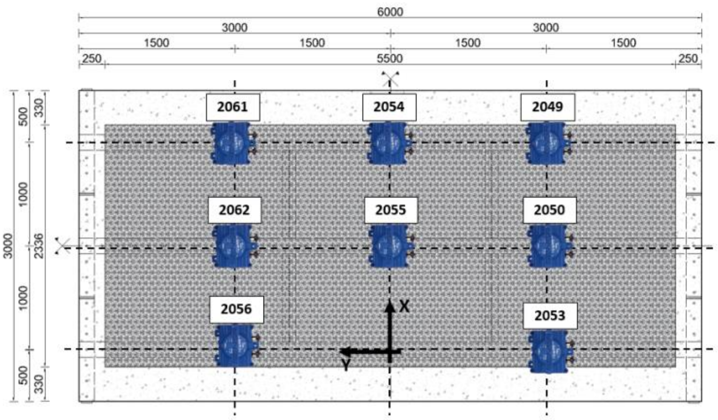

Figure 3.19. The setup used for the dynamic test.

The CX1 Accelerometer and Inclinometer patented by Sensr is a 5-channels instrument made of billet aluminium. It measures and forwards 3-axis accelerations and 2-axis tilt data to a PC connected via Ethernet or USB interfaces. While the Ethernet connection consumes 20 mA when supplied at 48 V, the USB absorbs 200 mA powered at 5 V. In this work, a USB connection is used both for data transmission and power supply. The physical characteristics include a total volume of 120 mm × 120 mm × 60 mm and a weight of 0.57 kg. Exploiting MEMS technology, the accelerometer exhibits a linear resolution of 10 μg, measuring acceleration ranges up to ±1.5 g, while the highest value detectable for angular data fluctuates around ±15° with a resolution of 10 μ°. When configured in acceleration mode it can provide up to 2000 sps along each axis, allowing for a maximum bandwidth of 1000 Hz; conversely, the inclinometer sample rate can not exceed 10 sps. The allowed temperature range is from −40 to 80 °C. Although composite steel-concrete decks are orthotropic plates, it is common practice for the dynamic investigation to align many sensors on the axis line of the bridge, while few of them are placed on transversal rows, owing to the detection of torsional modes. During the testing phase, the grid-shape arrangement of the sensors was chosen as a minimal setup able to detect and clearly distinguish the first six mode shapes of interest.

The recorded data were processed using both the frequency and the time domains. The Frequency Domain Decomposition (FDD) [27][181] and the Stochastic Subspace Identification (SSI-COV) [46][182][183], both available in a MatLab Environment [184][185], were applied to the recorded data. As previously pointed out, the modal identification was performed by considering the accelerations induced by environmental micro-tremors, hammer hits and people walking. A linear detrending and a resampling up to 500 Hz were applied to the recorded time series and two different output-only identification algorithms were employed to obtain an estimate of natural frequencies and mode shapes.

The vibration modes of the bridge are represented by the local maxima of the first singular value (SV) line (Figure 3.20), obtained by processing time windows of 16384 samples, considering an overlap of 50% between segments and adopting a Hanning window to reduce the leakage. Then, the SSI_COV algorithm was used to validate the FDD outcomes.

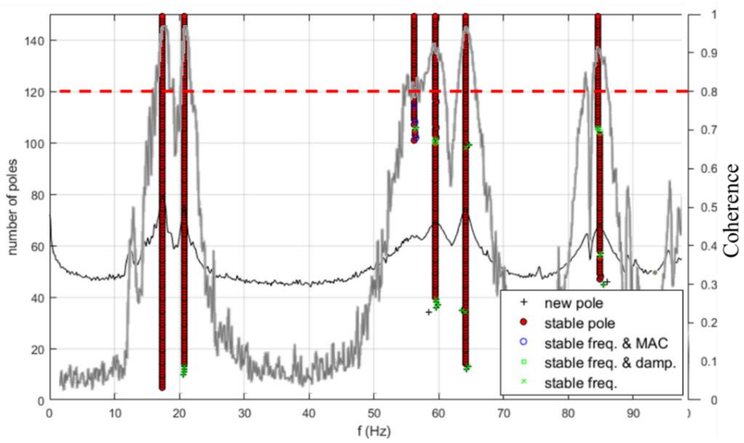

Figure 3.20. The plot of the first normalized singular value (black line), the SSI plot and the Coherence (grey line).

The inputs for the SSI method strongly influence their results, for this reason, they were chosen accordingly to what was suggested by *Magalhlaes et Al.* [183], [186]. In the present application, good results were achieved with a time lag of 1 second and a model order equal to 150. The lowest six amplification peaks are sharply shown in Figure 3.20, in which the first averaged normalized singular value, stable poles and the coherence are identified with the black line, the aligned red circles and the grey line.

A coherence value higher than 0.8 means that the measured signals are well correlated and thus noise shows a low influence. Instead, low coherence values indicate that the signals are strongly influenced by noise. For this reason, the spectrum part associated with coherence lower than 0.8 can be neglected. Thus, all the modal features associated with each local maxima are listed in Table 3.2. Then, the corresponding modal shapes are illustrated in Figure 3.22.

Table 3.2. List of identified modal shapes, modal frequencies and damping ratio.

Mode	Mode Type	FDD [Hz]	SSI [Hz]	Damping [%]
1	Bending	17.6	17.6	1.9%
2	Torsional	20.8	20.8	1.4%
3	Bending	59.4	59.5	2.1%
4	Torsional	55.9	56.8	4.4%
5	Plate-like	64.2	64.7	0.9%
6	Plate-like	85.0	85.3	1.4%

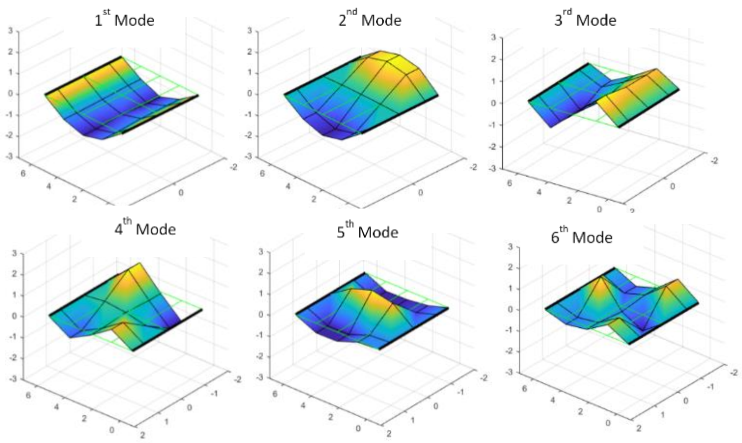

Figure 3.21. The lowest six identified mode shapes via the operational modal analysis.

Numeric interpretation of the experimental tests

Dealing with the description of the behaviour of the deck, the numerical model illustrated in Figure 3.22 was solved with the Italian version of the commercial FE software STRAND, supporting the mechanical parameters obtained through the tests. It figures out different colours meaning different mechanical properties, or thicknesses, assigned to the elements.

Three-dimensional solid 8-node brick elements were used to model the geometry of the concrete slab, while bi-dimensional 4-node shell elements were used to shape the geometry of the main beams, the corrugated steel sheet, and all the steel stiffening plates. Since secondary crossing beams and bracings are bolted to the main steel girders, these parts were introduced as beam and truss elements respectively. Besides, distributed masses have been applied to the slab surface modelling the layer of asphalt.

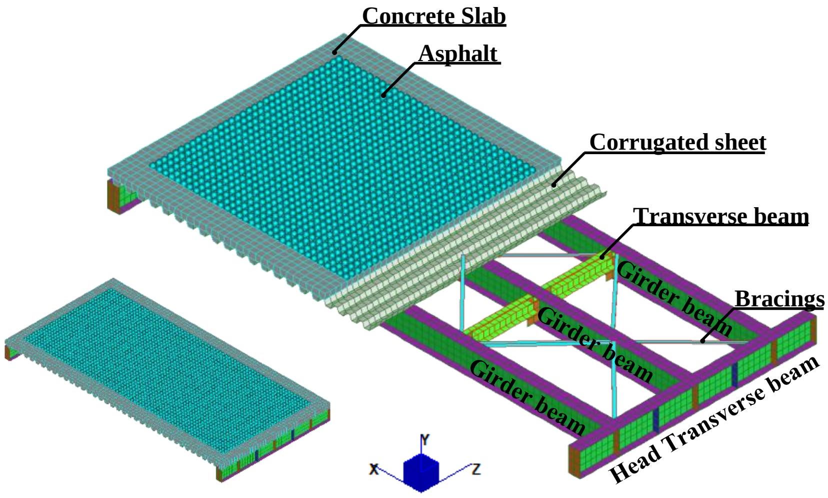

Figure 3.22. FE numerical model of the steel deck.

Concerning the load applied during the linear static analyses, the forces computed for each load step were spread as equivalent pressures in 150x150 mm^2 square areas on the concrete slab of the FE model. The pressures were set according to the positions of the concrete cubes used for enforcing loads on the bridge beams and the load fractions. Then, linear static and modal analyses were carried out simulating the load test and extracting the dynamic features, respectively. Regarding the static load test, Figure 3.23 and Figure 3.24 endorsed the perfect fit among the load-displacement curves at the supports and the bridge mid-span, respectively, with their numerical counterparts. The result was achieved by tuning the value of the concrete Young's modulus, from the value suggested in Section 3.1.1 to 25000 MPa obtained from the backhand stiffness calculation. In particular, Figure 3.23 illustrates the values of the two support deflections "*Exp_*" during the loading test compared with those obtained through the Numerical Linear Static analyses *"NLS_"*. The calibration was set by matching the black line (experimental average), with the results of the central girder supports in the FE model (red line). On the other hand, the static tests allowed also triggering the value of the static Young's modulus for the concrete slab. The tuning of the support stiffness and the concrete elastic modulus led to a very good fit among the experimental and the numerical displacements on the mid-span section for all the three girders (Figure 3.24).

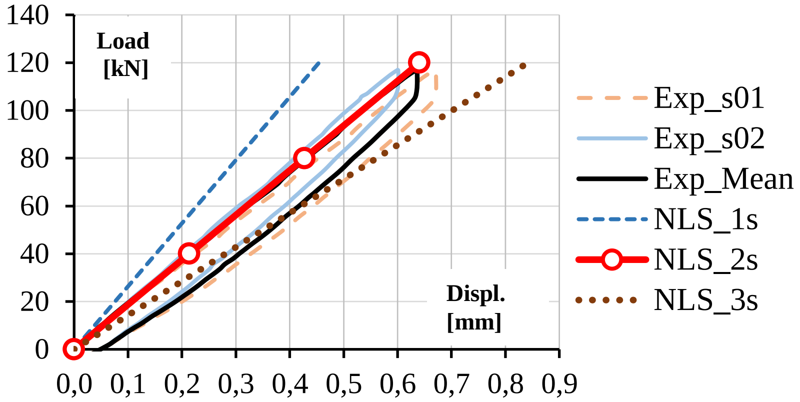

Figure 3.23. A plot of the Load-Displacement curve measured at the supports compared with the curves of the linear static analysis performed on the FE model.

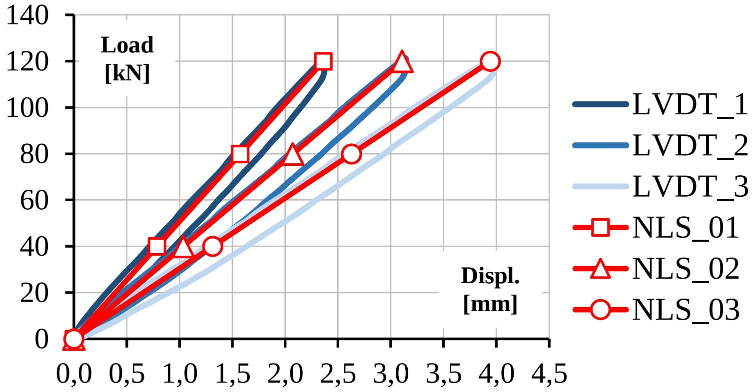

Figure 3.24. A plot of the Load-Displacement curve measured at the mid-span of the main beams and those reconstructed by performing a linear static analysis.

The numerical model showed good performance even regarding the dynamic behaviour: Table 3.3 compares the values of the fundamental frequencies, either estimated through the dynamic investigation or obtained carrying out the modal analysis on the FE model, showing reasonable discrepancies for all the modes with an exact match with the first frequency. Then, the corresponding modal shapes are illustrated in Figure 3.25

Table 3.3. Comparison among the frequencies obtained experimentally and those associated with the FE model.

Mode	Mode Type	FDD [Hz]	SSI [Hz]	Damping [%]	Numerical [Hz]	Error [-]
1	Bending	17.6	17.6	1.9%	17.6	0.0 %
2	Torsional	20.8	20.8	1.4%	20.4	-1.9 %
3	Bending	59.4	59.5	2.1%	51.1	-13.9 %
4	Torsional	55.9	56.8	4.4%	51.2	-8.41 %
5	Plate-like	64.2	64.7	0.9%	66.4	3.43 %
6	Plate-like	85.0	85.3	1.4%	92.8	9.18 %

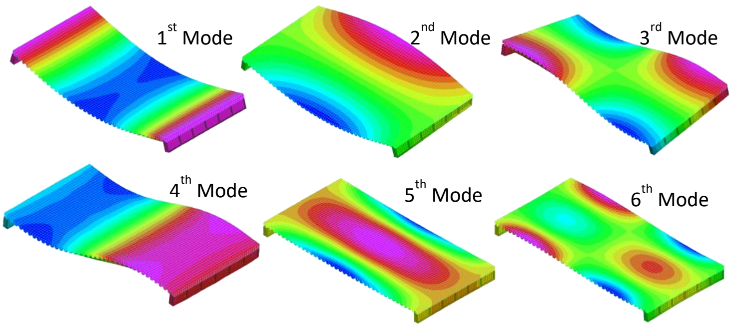

Figure 3.25. Lowest six mode shapes of the FE model.

Lastly, the accuracy of the FE model in terms of comparison among the mode shapes resulting from the application of FDD and their numerical counterpart can be validated by the computation of the well-known Modal Assurance Criterion (MAC) [187]. The Modal Assurance Criterion is applied by convolving the identified modal shapes with the numerical ones (Figure 3.25). Even the consistency of the FE model was proved, with all the values in the MAC matrix main diagonal higher than 80% according to Figure 3.26 and Table 3.4, except for the 3rd mode and the 4th one which appear inverted in their positions. Therefore, the obtained FE model can describe accurately either the static or the dynamic behaviour of the laboratory bridge by itself.

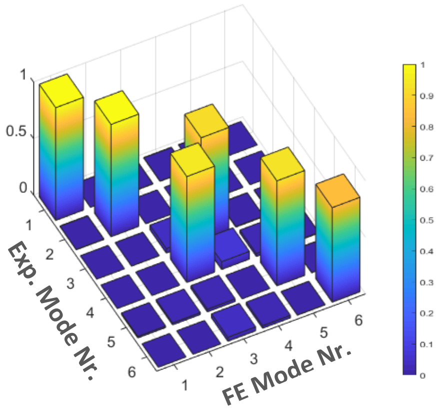

Figure 3.26. Bar-plots of the MAC comparing the set of the experimental modal shapes with those obtained from the numerical modal.

Table 3.4. Cross Mac values according to Figure 3.26.

Mode		**Calculated Modes**					
		1	**2**	**3**	**4**	**5**	**6**
Experimental Modes	**1**	1.00	0.00	0.00	0.00	0.00	0.00
	2	0.00	0.99	0.00	0.00	0.00	0.00
	3	0.00	0.00	0.04	0.91	0.01	0.01
	4	0.00	0.00	0.94	0.07	0.03	0.01
	5	0.01	0.02	0.02	0.00	0.93	0.00
	6	0.00	0.00	0.04	0.02	0.00	0.84

Description of progressive damage states and their numerical counterpart

According to the general overview of the bridge geometry in Section 3.1.3, two vertical cuts were provided at a fixed length of the two outer beams of the bridge model, able to simulate the presence of damage. From the mechanical point of view, the two cuts strongly reduced both the stiffness and the load-carrying capacity of the bridge, thus the two bolted twin plate splices illustrated in Figure 3.8 were properly designed to fully restore the original bending and shear capacity of the solid beams.

However, during the bridge modelling phase, since the stiffness of the bridge was completely restored by the splices and the mass of the plates used for this purpose is negligible compared to the whole mass of the bridge, the two splices were not included in the FE model considering the outer beams as solid beams. The simulation of damage involving the flange, or the flange and the web of a beam, was obtained by removing respectively the flange bolted twin splice plates, or both the flange and the web splice plates (Figure 3.27).

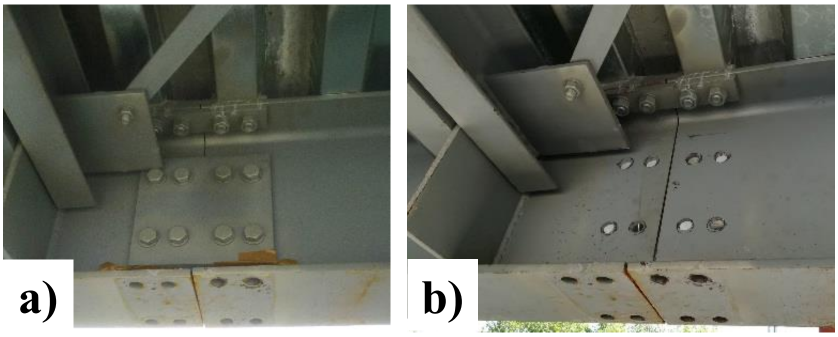

Figure 3.27. Progressive removal of the bolted plates: (a) removal of the bottom flange splice plates, (b) removal of flange and web splice plates.

Since the simulated damage in the beams consists of a vertical cut in the unbolted sections, this geometry change was obtained in the FE model by deleting a row of elements in the selected positions. In particular, the removal of the bolted splice plates in the bottom flange of the left side beam represents the damage phase D1; the removal of both the flange and the web splice plates of the same beam denotes the damage phase D2. By adding to this state the removal of the splice plates of the lower flange in the right side beam, the phase D3 is attained; progressing with the last web splice plates removal the maximum damage phase D4 is obtained.

For the sake of illustration, the damage conditions D1 and D2 are sketched in the following figure (Figure 3.28), by representing the portion around the cut section.

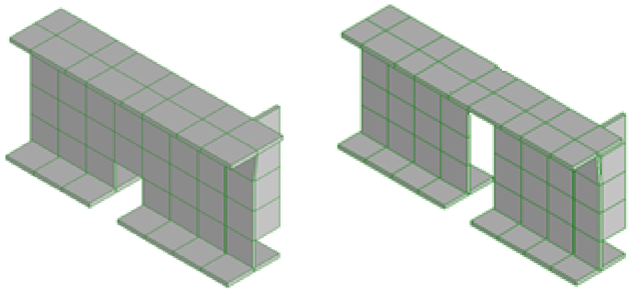

Figure 3.28: On the left the damaged condition D1, while, on the right, the Condition D2.

Proceeding with the dynamic investigations of the presented, the setup illustrated in Figure 3.29 involves only two accelerometers as typically used for continuous damage monitoring in simple bridges. In particular, only the CX-1 named 2056 and 2049 were adopted for the dynamic investigation at each stage of damage realization. These sensors were fixed on the lower flange of the two external beams at a quarter of their length.

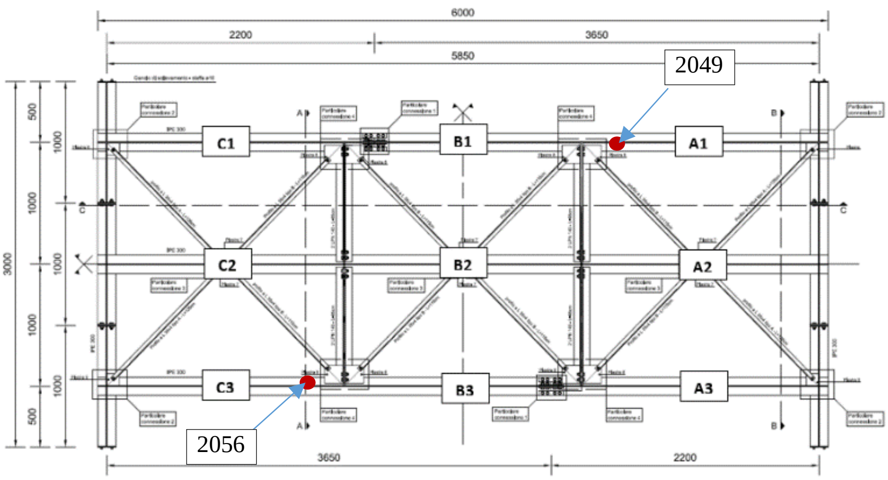

Figure 3.29. Accelerometers configuration in case of damage stages

All the measurements were performed repeatedly to improve the reliability of the extracted modal parameters similar to what concerned the investigation of the undamaged condition, earlier discussed. All the tests were completed in a few days with the same daily schedule, aiming to reduce the effect of the environmental conditions. The temperature, roughly equal to 30°C, was the same for all the tests.

At the end of the experimental campaign, all the data of the subsequent four damage phases were processed, by extracting the variations of the two lowest frequencies. Then, the frequency related to the first mode was computed for all the damage states by introducing the rigidity modification for the elements simulating the damaged zones and then compared with the frequencies of the FE model in the damaged conditions and those obtained from the dynamic investigation. The comparison among the frequency values led to data collected in Table 3.5 and then plotted in Figure 3.30.

Both the first and the second modes are very sensitive to damage. The experimental data showed an almost linear reduction in frequency with the progressive severity of the damage state.

The FE simulation led to a very good fit between the detected frequencies with those obtained performing the numerical modal analysis on the progressively changed model. The relative error in all the phases remained always below 3% of the experimental value. Since the aim of the study concerns the evaluation of the stiffness and the fundamental frequency variations due to the damage level, the modes higher than the first two were not taken into account.

Table 3.5. Comparison between numerical, experimental and analytical frequencies for each damage phase.

Freq.	D0 [Hz]	D1 [Hz]	D2 [Hz]	D3 [Hz]	D4 [Hz]
$F_{1,exp}$	17.6	17.1	14.7	14.5	13.8
$F_{1,mod}$	17.6	16.9	14.7	14.6	13.5
$F_{1,an}$	17.7	17.3	15.2	14.8	13.7
$F_{2,exp}$	20.8	20.3	19.3	18.7	16.1
$F_{2,mod}$	20.4	19.9	19.5	18.4	16.2
$F_{2,an}$	20.5	-	-	-	-

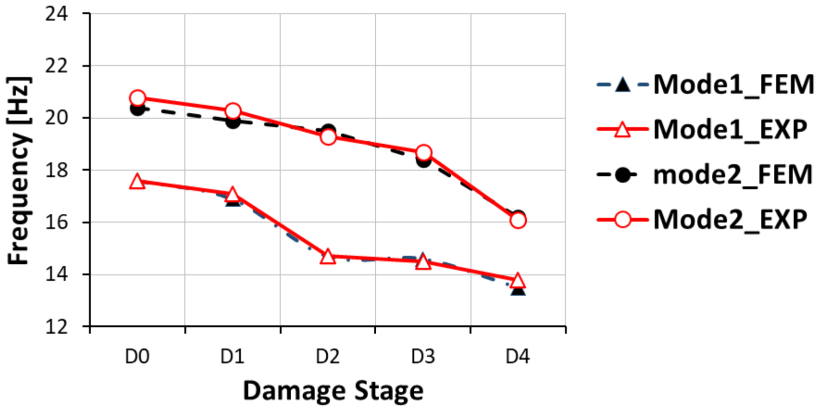

Figure 3.30. Frequency decay due to the presence of damage.

Concerning the fundamental frequency, both experimental outcomes and analytical calculations correctly evaluated the reduction in terms of stiffness. In particular, a decrease of 6%, 30%, 32%, and 39% in total stiffness was estimated through the frequency values extracted from the dynamic tests. The analytical stiffness decay is then computed for the damage conditions D1, D2, D3, and D4, resulting in 5%, 26%, 30% and 40% of the original value.

3.2.2 Laboratory steel frame: dynamic test and Damage Detection

The present section discusses the experimental campaign carried out at the *"University La Sapienza"* of Rome during the *"12th Asia-Pacific-Euro_Summer_School"*, which involved the dynamic investigation of a one-bay and 4-floors steel frame prototype with the aim of detecting the damage from the data collected during the tests. In particular, an electrodynamic shaker and an instrumented hammer are used for exciting the structure, whereas two systems were chosen for collecting data, simultaneously: firstly, four uniaxial piezoelectric accelerometers were placed at each floor collecting the accelerations, meanwhile, several markers were fixed to the frame columns whose motion is tracked using a high-speed camera. In this context, since even the inputs are available for the analysis, all the features suggest the use of EMA procedures, basically normalizing the spectra associated with the recorded outputs with those corresponding to the inputs. The focus of this test regards the comparison of the natural frequency and the mode shapes, only, neglecting the associated mode damping. The frame geometry and more detailed information about the tests are provided in the following.

Materials and Geometry of the steel frame

The steel prototype was built by the *"University La Sapienza"* in Rome which provided the technical drawings. The frame is made of S235 steel and consists of four floors with 200 mm of inter-storey completing a total height of 800 mm as shown in Figure 3.31. Each squared plan storey is 300 mm wide and consists of four 50x50x4 mm L-shaped beams which are bolted to the columns creating a solid floor. Most of the columns are 50x4 mm steel plates, while two of the four columns at the third level are smaller than the other (20x4 mm) reducing the storing stiffness simulating a type of damage. Then a ø12 hollow circular diagonal bracing with 0.4 mm of thickness is inserted for creating the undamaged condition of the frame.

Figure 3.31. Geometry of the one-bay and 4 floors steel frame: Undamaged and Damaged.

Description of the experimental campaign

Concerning the dynamic investigation of the steel frame, four parallel setups were involved in testing both the damaged and undamaged condition of the frame: two setups involved the use of an electrodynamic shaker exerting a white-noise excitation of the model, whereas an instrumented hammer was used for exerting an impulsive excitation at the top floor of the steel frame. Moreover, an additional difference occurs in the way chosen for collecting data: on one hand, an ICP accelerometer was installed at each storey to record the accelerations; on the other hand, the high-speed camera collected the displacements of 24 markers creating the time series of the motion of each point. Both the layouts are illustrated in Figure 3.32, where the locations of the accelerometers and the markers are marked with the green points in the photos or even letters on the corresponding simplified model.

Concerning the accelerations, sampling frequencies equal to 600 Hz and 4800 Hz were respectively chosen for the tests with the shaker and the hammer. Instead, 200 Hz and 200 frames per second were adopted for the base accelerations of the shaker and the displacements for the high-speed camera.

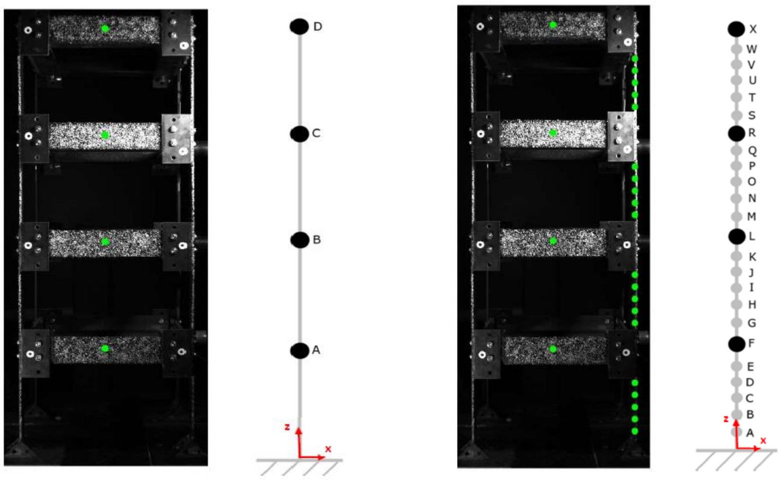

Figure 3.32. Experimental setups for the experimental campaign: Accelerometers (left), Markers (right).

Assessment of the modal feature and discussion of the results

Two sets of accelerations were recorded as “structural inputs” for the undamaged and the damaged configuration: dealing with the instrumented hammer the impulsive excitation exerted on the frame’s top floor was used as input for the analysis of the structural responses collected by the sensors illustrated in Figure 3.32; whereas an accelerometer placed at the base measured the input provided by the table shaker. Then the corresponding outputs in terms of accelerometer measurements and camera point collections completed the data sets for the experimental campaign. The natural frequencies estimated by processing the whole dataset are listed in Table 3.6 detected on the spectra of Figure 3.33 and Figure 3.34 associated with the hammer tests and shaking table tests, respectively. Since both inputs and outputs are available, EMA techniques are used for the frequency assessment using the *"modal-frf"* function already present in the Matlab environment, either for the accelerations or the displacements.

Table 3.6. Natural frequencies of the steel frame prototype for damage and undamaged configurations.

Condition	Mode	Frequency (Acc) [Hz]	Frequency (Disp) [Hz]
Undamaged	1st	17.3	17.3
	2nd	54.9	54.9
	3rd	72.8	72.9
	4th	-	-
Damaged	1st	14.9	14.9
	2nd	43.5	43.6
	3rd	70.9	71.1
	4th	82.8	83.0

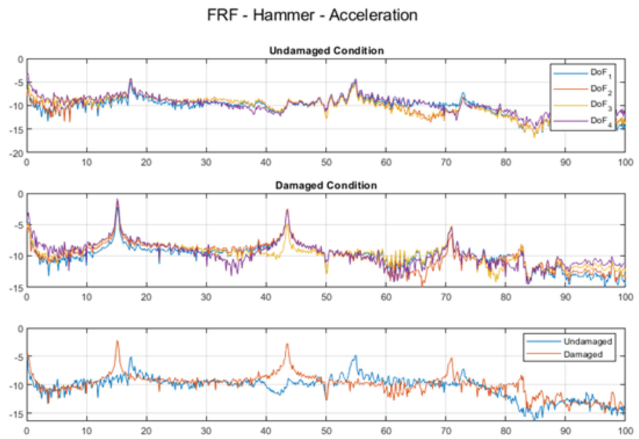

Figure 3.33. Frequency spectrum obtained from Hammer tests.

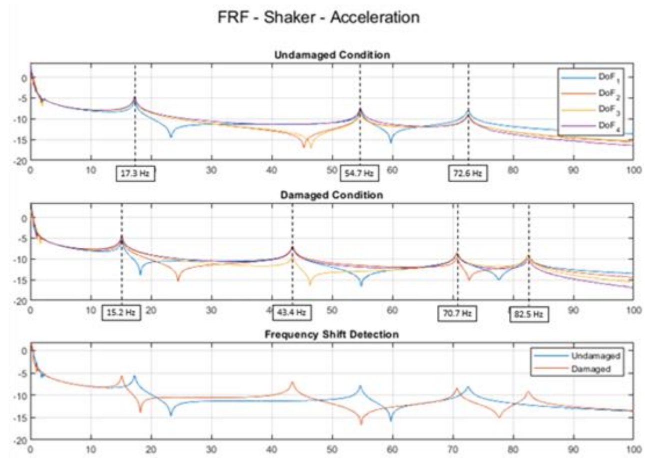

Figure 3.34. Frequency spectrum obtained from shaker tests.

All the time series required resampling to be compared with each other, thus a common scanning frequency equal to 200 Hz is chosen, according to the lower sampling frequency used within the experimental campaign. It means that the frequency bandwidth covers the range of 0-100 Hz. The steel frame is characterized by four storeys, thus four natural frequencies and four mode-shapes to them associated are expected at the end of the analysis. Unfortunately, the fourth frequency of the undamaged condition is higher than 100 Hz, and therefore it cannot be detected on the frequency spectra. Anyway, the reduction of all the frequencies is very clear by observing either the table or even the frequency spectra, where the blue line and the red line are respectively associated with the undamaged and the damaged condition of the frame.
Both the techniques used for recording the structural response provide very similar results in terms of frequency (Table 3.6) and even mode shapes too (Figure 3.35), even though the higher number of degrees of freedom associated with the use of the high-speed camera shows a better description capability concerning the mode shape spatial resolution.

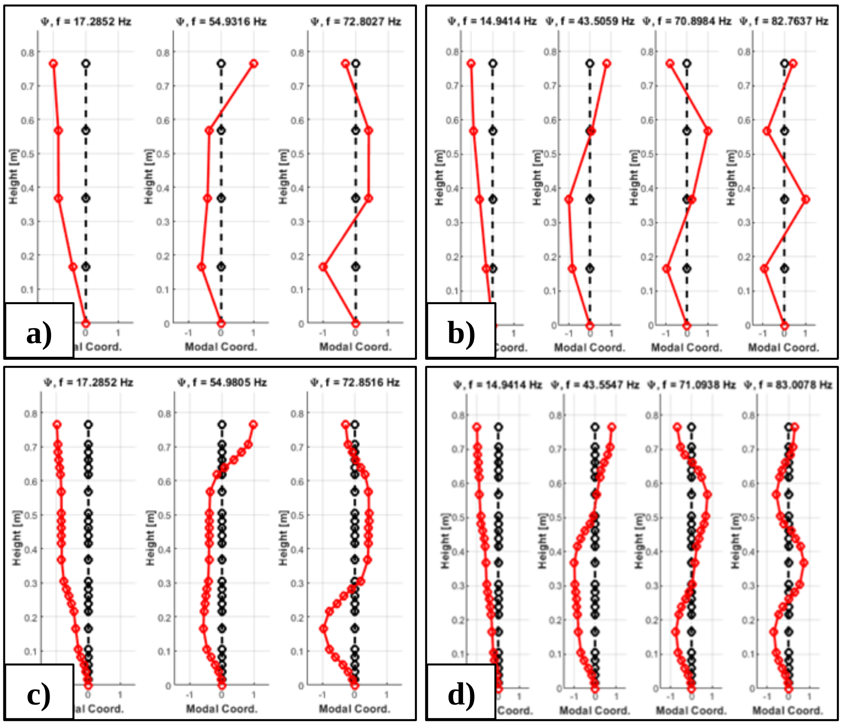

Figure 3.35. Mode shapes of the steel frame: Accelerometer - Undamaged (a) and Damaged (b); Speed camera - Undamaged (c) and Damaged (d).

Thank to the large amount of data collected during the tests, two main damage indexes can be used for detecting, or not, the occurrence of damage. In particular, the Modal Assurance Criterion (Figure 3.36) and the Coordinate Modal Assurance Criterion (Figure 3.37) have been implemented for this purpose, using the coordinates corresponding to the modal shapes associated with the damaged and the undamaged conditions. As usual, the MAC index only suggests that something happened on the structure, without any indication regarding the location and the severity. Concerning the undamaged condition, the MAC is computed among the modal coordinates of the three modal shapes associated with the absence of damage and obtained via the modal identification algorithms. Because of the orthogonality property of the mode shapes, only the MAC values over the main diagonal must be equal to 1 and 0 elsewhere. Figure 3.36 shows how MAC values change when the damage occurs (removing the steel bracing), indeed the values on the main diagonal decrease while the other tends to increase.

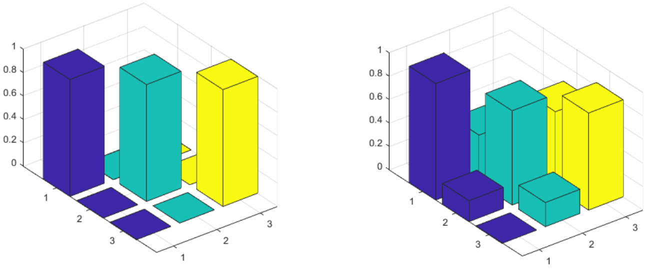

1.000	0.001	0.001
0.001	1.000	0.001
0.001	0.001	1.000

1.000	0.410	0.150
0.180	0.810	0.660
0.001	0.210	0.830

Figure 3.36. Effect of the Damage on the MAC Values: comparison between the undamaged (left) and the damaged condition (right).

The absence of information about the damage location led to the implementation of the COMAC index, which provides some information about the exact location of the damage. The plot of COMAC illustrated in Figure 3.37 suggests that something is happening at the level where the steel bracing has been removed in the case of the measurement of accelerations, and displacements.

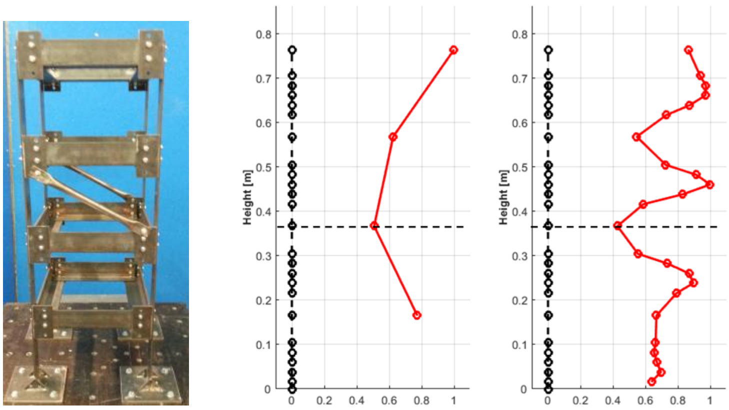

Figure 3.37. COMAC values computed starting from the accelerations and the Displacement.

3.2.3 *Contribution in the field of local damage identification*

In this Section, the problem of local damage affecting the main frequencies of a structure is addressed by investigating the dynamic behaviour of a steel-concrete composite bridge deck and a one-bay 4-storey frame made of steel. Both the experiments shared the same idea of planning one, or more than one, damage configuration during the design phase providing cuts in the main girders (e.g. steel bridge) or having a reduced size of the columns (e.g. steel frame), replacing the stiffness corresponding the undamaged condition properly designing bolted plates or bracing, respectively. The experimental campaign carried out on the steel bridge deck model and presented in Section 3.2.1 has shown a very good agreement between the six vibrating modes and those provided by the FE model in the range up to 100 Hz except for the third and fourth modes, which are switched between the experiments and the calculations. The swap in the mode order is even pointed out by convolving the two sets of numerical and identified modal shapes in the MAC computation, which collects good cross-correlation values. The local damages simulated in two of the three main girders produced important shifts in the values of the first two main frequencies, detecting their high sensitivity to the presence of progressive damage. In particular, the studied experimental model permitted not only to gather a wide set of data in several bridge damage configurations but through the comparison with a 3D FE model did establish a link between the dynamic properties and the damage features which will be useful in planning the condition assessment through dynamic monitoring of real deteriorated full-scale bridges. However, since the investigation of the damaged configurations involves only two accelerometers, no information about the location of damage and the evolution of the mode shapes have been here discussed.

This is the reason why even the identification of a steel frame tries to provide more details about the damage localization, including an original setup for the dynamic investigation of small and highly deformable structures. Contemporaneously to the use of the classic EMA approach associated with the use of accelerometers for the structural characterization, the displacements of several markers diffused on the frame are collected by the high-speed camera mentioned in Section 3.2.2. Consistent outcomes have been obtained from the two approaches, even though the use of several markers increases the spatial resolution of the experimental mode shapes compared with those obtained from the data collected by the four accelerometers. In this context, MAC and COMAC are used to detect the presence and the location of damage over the height of the frame, corresponding to the removal of the steel bracing and the reduction of the cross-section of the columns.

3.3 Diffused damage: theory of breathing cracks

During the lifespan of critical structures, owing to their safety, repeated inspections are fundamental, especially for the maintenance management delivered by bridge owners. Regarding concrete structures, several threats can adversely affect their bearing capacity and stability. First, the material ageing is mainly due to the combination of an aggressive environment with a lack of maintenance works, often producing corrosion of steel rebars and concrete cover losses. Dealing with bridges, The increasing traffic demand of the last decades certainly influences the fatigue behaviour of the materials involved in the construction, even if concerning the entity of loads, the occurrence of cracks is often due to the transit of exceptional transports or heavyweight drops on bridge deck surfaces [188].–Cracks could be often not visible to naked eyes or unskilled inspectors, which means that field testing is usually required for an unbiased damage grading.

Static and dynamic field tests strongly help in assessing the health of an existing structure, but often they require the experience of skilled people able to properly design and schedule the activities required for a sound interpretation of the outcoming data.

The tests should be carefully planned by taking into account the operability of the structure object of investigation. For instance, concerning bridges and highways, the stop of the traffic flowing on them produces large distress to the users, and sometimes, huge profit losses. It is the reason why many researchers choose to carry out ambient vibration tests dealing with this class of structures. Besides, very useful information is gathered by investigating the behaviour of scaled models [189][190] or existing structures nearly to be demolished [170][173]. These studies are still the only possibility for research validation in the field of structural monitoring of heavily damaged structures. The advantage of scaled bridges or small structural components built in the laboratory is to freely deal with any kind of sensor (or networks) and to easily handle, or simulate, the presence of damage, confirming damage identification algorithms. No significant restrictions, or constraints, can limit the possibility of investigating structural behaviour or material mechanics. The level of detail of a structural replica typically depends on the purpose of the study. For example, dealing with Reinforced Concrete (RC) structures *Maeck et Al.* [191] addressed the problem of cracked RC beams by investigating their static and dynamic behaviour.

Even if from the probabilistic point of view, the problem of estimating the residual bearing capacity of structures is still in progress, many studies are already present in the literature concerning the assessment of the life cycle performance and the benefits of Structural Health

Monitoring (SHM) [192]–[194]. However, no deterministic relationship exists for assessing the remaining life of an existing structure.

This section discusses from a deterministic point of view the links between the frequency decay of an RC beam with the damage produced by increasing loads according to the breathing cracks theory, focusing on its validation with experimental data collected on a small replica of a concrete bridge deck and a set of concrete beams.

3.3.1 Damaged concrete beams: the breathing crack theory

Dealing with concrete structures, the occurrence of damage may be related to many reasons mainly associated either with environmental agents or the load exerted on the structural elements. Typically, freeze/thaw cycles or the development of rust as a consequence of the corrosion of the steel rebars may produce cracks on the concrete covers. Concurrently, one structural element may be subjected to an exceptional load, overcoming the cracking bending moment and causing the occurrence of a first crack along with that element. The evolution of the first crack, as a consequence of the stiffness reduction and repeated loads, increases the severity of existing damages leading to the potential structural collapse.

In the past, many experimental investigations pointed out that reinforced concrete structures in the non-linear range, starting with the crack formation and ending at the yielding of rebar, show a reduction of the natural frequencies from 0 to 25% of the uncracked values. This interval, however, is significantly less than expected, due to the presence of opening and closing cracks, the so-called effect of “breathing cracks”.

Although the onset of cracking is characterized by a first significant frequency drop, temperature changes, chemical attacks and cyclic loading can modify the recorded values, hiding or emphasizing in some way the damage that occurred in the structure.

In recent contributions, the problem of eliminating the temperature effect on the recorded signals has been solved effectively. On the one hand, the statistical analysis of the initial long term characterization of the bridge can allow for setting up a reference curve that expresses the natural frequencies as a function of temperature [168]. On the other hand, algorithms based on the co-integration concept can eliminate the temperature influence on the recorded signals [195].

The deterioration occurring inside cracks mainly involves loss of tension stiffening of the concrete and aggregate interlock across crack faces. Therefore the bond deterioration caused by cyclic loading or bar corrosion can increase the crack opening, thus reducing the crack closure stiffening effect [196]. Although these non-linear effects can be significant, the dynamic stiffening due to breathing remains dominant when the crack opening is sufficiently small, as in the elastic range of the steel reinforcement with negligible rusting.

This section addresses the fundamental problem of expressing the stiffness deterioration in terms of frequency shift. The initial step is the study of a large set of experiments on simply supported ordinarily reinforced concrete beams discussed in the literature. The collected data encompass a wide range of material properties, beam geometries, loading patterns, and frequency extraction methods. In these investigations, the beam frequencies have been extracted at each loading step, up to the ultimate state of steel reinforcement yielding. By comparing the normalized non-dimensional load-frequency curves, a significant agreement can be observed among all the experiments. This is a key aspect allowing a robust comparison of the theoretical and numerical interpretations with the existing experimental data.

Lastly, in the framework of damage mechanics, the phenomenon of the "breathing cracks" is solved in an approximate but energetically consistent format. In this way, it is possible to build an analytical formula that expresses the frequency shift in terms of the maximum load experienced by the beam. It is to cite that simulations based on even complex models, able to predict the rigidity decay of cracked sections, fail in predicting the natural frequency of cracked beams if they disregard the crack closure stiffening effect.

Analysis of the available experimental data

The selection of the comparison data set presents several problems due to the difficulties of retrieving missing values and as a consequence of the digitalization of data published in diagram form. Naming with b, h, L, the width, the depth, and the length of each beam; collecting the amount of steel reinforcement A_s, the mechanical properties of the materials and the data involved in the experiments concerning the ultimate shear V_{exp}, the ultimate and cracking bending moments M_u and M_{cr}, and the corresponding natural frequencies, Table 3.7 presents the data extracted from the literature [191], [196]–[204]. In addition, naming with λ and k_D the non-dimensional ratios M_{max}/M_y and f_D/f_0 stating the maximum moment acting on the beams during the test with respect to their yielding moment M_y and the corresponding frequencies, the load-frequency data of each experiment are collected in Table 3.7 and then plotted in Figure 3.38.

Table 3.7. Data of the collected experimental tests.

author	Ref.	Code	b	h	f_{ck}	A_s	f_{yk}	L	c	V_{exp}	f_{exp}	M_{cr}/M_u	$L_{D,max}$
			mm	mm	MPa	mm	MPa	m	m	kN	Hz	-	%
Askegaard	[197]	VBF	150	100	50	2ø10	500	3.00	1.00	6.0	22.5	0.258	83%
Askegaard	[197]	VXR	150	100	15	2ø10	500	3.00	1.00	5.0	19.1	0.130	91%
V. Abeele	[196]	1	250	60	33	2ø10	500	0.99	0.15	5.7	161.0	0.187	84%
Maeck	[191]	1	250	200	25	3ø16	500	3.60	0.00	50.7	22.3	0.193	81%
Maeck	[191]	2	250	200	25	3ø16	500	5.70	2.00	25.3	21.9	0.193	87%
Neild	[198]	A	200	105	38	3ø12	410	2.80	0.00	8.2	21.7	0.177	82%
Neild	[198]	B	200	105	38	3ø12	410	2.80	0.00	8.2	22.4	0.177	82%
Tan	[199]	1	135	210	35	3ø10	500	2.80	1.00	21.5	92.0	0.282	82%
Koh	[200]	1	500	150	44	6ø13	560	2.70	0.90	48.8	29.5	0.219	85%
Massenzio	[201]	-	50	85	25	2ø5	500	0.67	0.23	5.0	530.0	0.195	87%
Baghiee	[202]	B1-B3	150	200	20	2ø12	494	2.20	0.60	15.0	114.5	0.218	84%
Baghiee	[202]	B4-B6	150	200	20	2ø16	483	2.20	0.60	30.0	108.8	0.177	87%
Musial	[203]	B-I	150	250	52	2ø12	563	3.00	0.00	14.0	91.0	0.378	62%
Musial	[203]	B-II	150	250	51	2ø12	563	3.00	0.00	14.0	90.0	0.376	62%
Musial	[203]	B-III	150	250	45	3ø10	548	3.00	0.00	14.0	91.0	0.349	65%
Musial	[203]	B-IV	150	250	41	3ø14	555	3.00	0.00	29.0	81.0	0.192	81%
Hamad	[204]	BS-I	130	210	37	3ø10	541	2.70	0.70	20.9	43.0	0.223	83%
Hamad	[204]	BS-II	130	210	37	3ø10	541	2.70	0.70	21.3	41.9	0.225	83%
Hamad	[204]	BS-III	130	210	35	3ø10	541	2.70	0.70	20.3	42.6	0.216	84%

Askegaard &Langsoe [197] examined the frequency variation for the load in beams deteriorated by freeze-thaw cycles. *Van den Abeele & De Visscher* [196] determined modal curvatures by using resonant acoustic spectroscopy. *Maeck et Al.* [191] defined a parametric form of the length-wise variation of beam rigidity and evaluated the parameters by minimizing the error of the predicted modal frequencies through the inversion of the sensitivity matrix. *Neild et Al.* [198] pointed out the strong frequency variation in correspondence of the cracking load. *Tan* [199] discussed the effect of "breathing cracks" in terms of bilinear and non-linear models. *Koh et Al.* [200] used partitioned beam models for the interpretation of their observation, but it is fair to mention that their results do not match completely with the trend shown by all the other investigations. *Massenzio et Al.* [201] examined the variation of five natural frequencies, but some inconsistencies are visible around the cracking point. *Baghiee et Al.* [202] considered ordinary and FRP reinforced beams and used modal assurance criteria to detect the damage. *Musial* [203] presented results for beams with two reinforcement ratios but some inconsistency appears by comparing the two sets. *Hamad et Al.* [204] presented very detailed experimental results, although the obtained frequencies are biased by the use of rubber supports for the beams. The interpretation is worked out by using fracture mechanics and partitioned beam elements. The model however does not incorporate breathing cracks, and therefore a specific adjusting coefficient is introduced owing to match the experimental results.

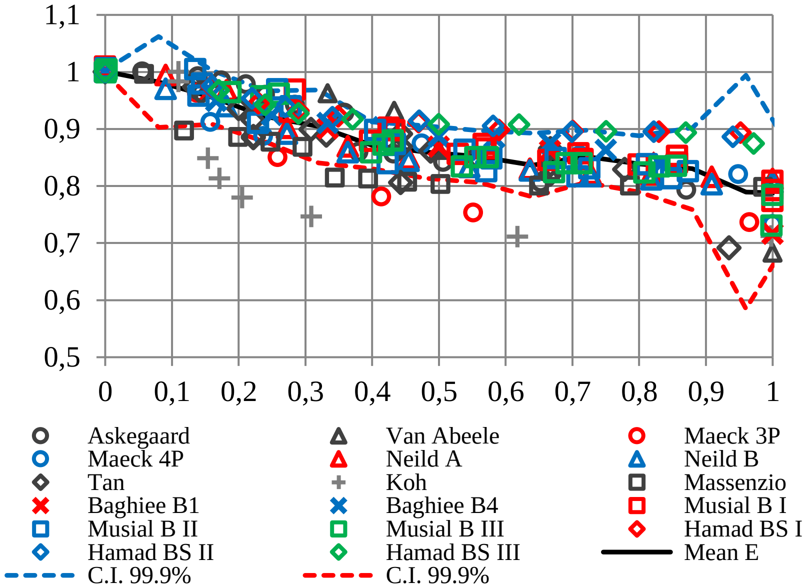

Figure 3.38. Load – Frequency plot of the selected experimental tests.

The statistical analysis of the results indicates that almost all the data fall in a confidence interval of 99.9% of the mean, while the coefficient of variation COV is less than 5% over the whole range of data. Moreover, the data highlight a sharp increase in variance at the onset of cracking and near the failure. As is apparent, Koh data [200] have a large deviation from the overall trend and exit from the confidence interval. Since the tested elements are very thin, this mismatch is probably due to the lack of crack closure effect.

In what follows, by using the principle of static equivalence of the kinetic energy, the mechanics of the damaged RC section will be used to set up the beam's natural frequency. Some experiments with beams with a single crack will be reviewed to validate a model for the breathing crack phenomenon. The obtained interpretation will be used in building a formula able to characterize the relationship between load level increase and frequency decay.

Table 3.8. Non-dimensional load-frequency curves.

Askegaard &Langsoe [197]						Massenzio et Al. [201]						Tan [199]	
VBF-1		VBF-3		VXR-1		F_1		F_2		F_3		1	
λ	k_D	λ	k_D	λ	k_D	λ	k_D	λ	k_D	λ	k_D	λ	k_D
0.0565	1.0000	0.0568	1.0003	0.0557	1.0005	0.0000	1.0000	0.0000	1.0000	0.0000	0.9988	0.0000	1.0000
0.1230	0.9841	0.1395	0.9987	0.1390	0.9923	0.0606	0.9943	0.0585	0.9960	0.0691	0.9945	0.1338	0.9739
0.1725	0.9748	0.1819	0.9969	0.1743	0.9850	0.1191	0.8881	0.1188	0.8971	0.1296	0.9522	0.1438	0.9638
0.2161	0.9375	0.2115	0.9935	0.2114	0.9780	0.2005	0.8468	0.1997	0.8859	0.2188	0.9449	0.2003	0.9355
0.2322	0.9357	0.2457	0.9853	0.2400	0.9600	0.2524	0.8387	0.2478	0.8770	0.2734	0.9388	0.2220	0.8955
0.2931	0.9318	0.3089	0.9636	0.2847	0.9426	0.2974	0.8211	0.2960	0.8682	0.3280	0.9290	0.3083	0.8992
0.3138	0.8341	0.3312	0.9080	0.3590	0.9284	0.3476	0.7938	0.3442	0.8143	0.3777	0.8762	0.3315	0.8892
0.3734	0.8159	0.3924	0.8860	0.3800	0.8600	0.3978	0.7881	0.3941	0.8127	0.4414	0.8713	0.4429	0.8556
0.4955	0.8072	0.4376	0.8711	0.4323	0.8564	0.4567	0.7833	0.4527	0.8071	0.5051	0.8658	0.4877	0.8611
0.5000	0.8060	0.5000	0.8600	0.5063	0.8418	0.5070	0.7784	0.5026	0.8031	0.5560	0.8610	0.5558	0.8511
0.6144	0.8068	0.6442	0.8574	0.6526	0.8058	0.6560	0.7767	0.6506	0.8006	0.7234	0.8520	0.6671	0.8411
-	-	-	-	0.8710	0.7929	0.7946	0.7742	0.7866	0.8006	0.8743	0.8552	0.7784	0.8292
-	-	-	-	-	-	0.9905	0.7676	0.9862	0.7982	1.0425	0.8487	0.9347	0.6914

Neild et Al. [198]				Hamad et Al. [204]						Baghiee et Al. [202]			
A		B		BS-I		BS-II		BS-III		B1-12D-0L		B4-16D-0L	
λ	k_D	λ	k_D	λ	k_D	λ	k_D	λ	k_D	λ	k_D	λ	k_D
0.0000	1.0000	0.0000	1.0000	0.0000	1.0000	0.0000	0.9994	0.0000	1.0006	0.0000	1.0011	0.0000	1.0000
0.0909	0.9942	0.0909	0.9703	0.1594	0.9749	0.1605	0.9754	0.1703	0.9674	0.3333	0.9008	0.1667	0.9488
0.1818	0.9677	0.1818	0.9402	0.2299	0.9451	0.2202	0.9537	0.2397	0.9424	0.5000	0.8688	0.2500	0.9243
0.2727	0.9019	0.2727	0.8920	0.2896	0.9317	0.2701	0.9391	0.2896	0.9273	0.6667	0.8613	0.3333	0.9104
0.3636	0.8695	0.3636	0.8595	0.3492	0.9224	0.3406	0.9203	0.3709	0.9169	0.8333	0.8411	0.4167	0.9029
0.4545	0.8486	0.4545	0.8440	0.4696	0.9119	0.4707	0.9145	0.5000	0.9081	1.0000	0.7163	0.5000	0.8869
0.5455	0.8334	0.5455	0.8336	0.5900	0.8979	0.5813	0.9051	0.6204	0.9076	-	-	0.5833	0.8848
0.6364	0.8301	0.6364	0.8272	0.7007	0.8961	0.6996	0.8951	0.7505	0.8959	-	-	0.6667	0.8752
0.7273	0.8218	0.7273	0.8173	0.8297	0.8949	0.8221	0.8951	0.8698	0.8936	-	-	0.7500	0.8635
0.8182	0.8205	0.8182	0.8117	0.9523	0.8938	0.9403	0.8863	0.9718	0.8744	-	-	0.8333	0.8389
0.9091	0.8164	0.9091	0.8033	-	-	-	-	-	-	-	-	-	-
1.0000	0.8122	1.0000	0.8060	-	-	-	-	-	-	-	-	-	-

Musial [203]						Maeck et Al. [191]				V. Abeele [196]		Koh et Al. [200]	
B-I		B-II		B-III		1		2		1		1	
λ	k_D	λ	k_D	λ	k_D	λ	k_D	λ	k_D	λ	k_D	λ	k_D
0.0008	1.0031	0.0008	1.0023	0.0013	1.0008	0.0000	1.0000	0.0000	1.0000	0.0000	1.0000	0.0000	1.0000
0.2807	0.9492	0.1404	0.9806	0.1880	0.9640	0.1379	0.9633	0.1581	0.9120	0.3333	0.9747	0.1099	1.0000
0.4185	0.8928	0.2552	0.9397	0.2475	0.9593	0.2586	0.8505	0.2372	0.8874	0.4333	0.9618	0.1099	0.9833
0.5556	0.8649	0.4211	0.8702	0.4156	0.8702	0.4138	0.7816	0.4743	0.8747	0.5000	0.9220	0.1542	0.8489
0.6963	0.8497	0.5631	0.8456	0.5547	0.8451	0.5517	0.7534	0.7115	0.8537	0.6667	0.9000	0.1713	0.8133
0.8379	0.8438	0.7030	0.8321	0.6930	0.8343	0.9655	0.7363	0.9486	0.8204	1.0000	0.8367	0.2055	0.7799
1.0000	0.7917	0.8446	0.8256	0.8317	0.8310	_	-	1.0000	0.7329	_	-	0.3088	0.7465
_	-	1.0013	0.7894	1.0000	0.7714	_	-	_	-	_	-	0.6178	0.7111
_	-	-	-	-	-	-	-	-	_	-	-	0.9979	0.7121

The natural frequency of a damaged beam

The natural frequency of an Euler-Bernoulli beam with distributed or concentrated mass can be obtained through the equivalence of the kinetic energy of the vibration mode, and the potential energy of one equivalent deflected shape of the beam under a concentrated force [205] illustrated in Figure 3.40. If the mass of a simply supported beam is concentrated at the mid-span, the equivalent force to be applied on the beam, leading to the equivalent vibration frequency, corresponds to 17/35 of the beam weight G.

Thus, the natural frequency of a simply supported beam can be expressed as a function of the maximum displacement occurring under this force. Considering a beam of length L, the displacement is:

$$\delta_0(L/2) = \frac{17G}{35} \cdot \frac{L^3}{48 \cdot EJ_0} \tag{3.5}$$

where E and J_0 are respectively the elastic modulus and the inertia moment of the beam section in undamaged condition. The frequencies of the natural modes are finally obtained as:

$$f_n = \frac{n^2}{2\pi} \cdot \sqrt{\frac{g}{\delta_0}} \tag{3.6}$$

with g the gravity constant 9,81 m/s^2, and n the number of half sinusoids contained in the beam length for a given mode.

If the beam presents a damaged part, the displacement is increased by the concentrated curvature spike resulting from the local loss of rigidity of the damaged length [198] and a decrease in the natural frequency is observed.

As an example, Figure 3.39 shows the evolution of the experimental curvature obtained in [191] for a beam damaged with subsequent increasing load steps, while Figure 3.40 shows the reference geometry for the damaged beam, used in the following analytical elaboration. The beam displacement under the equivalent force is computed as the sum of the undamaged beam displacement δ_0 plus the incremental displacement δ_D caused by the localized curvature spike.

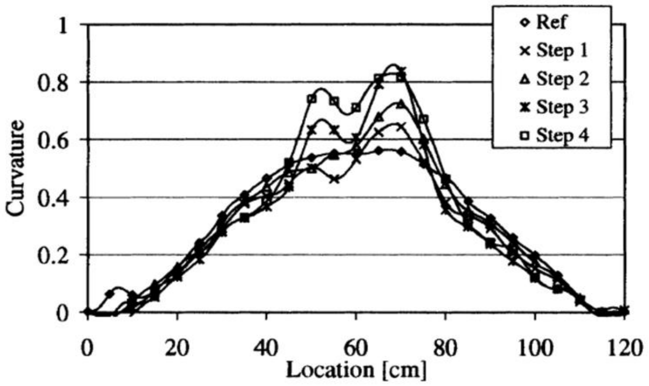

Figure 3.39. Modal curvature spike obtained by the vibration mode of a damaged beam.

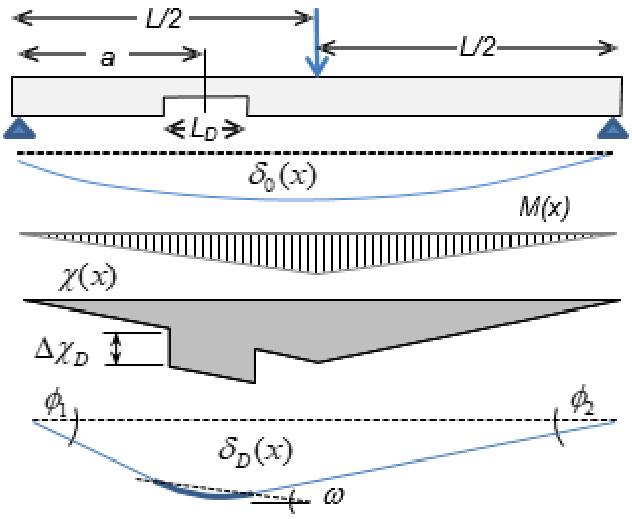

Figure 3.40. Displacement components in a damaged beam.

The damage engenders a total rotation $\Delta\chi \cdot L_D$ between the two rigid beam arms connecting the damaged zone to the supports. By enforcing the continuity equation of the rotation at the connecting sections, the displacement increase δ_D can be computed straightforwardly. If the average tilt of the curved segment is indicated as ω, the compatibility equation is:

$$\left(\frac{\chi L_D}{2}+\omega\right)\cdot\left(a-\frac{L_D}{2}\right)=\left(\frac{\chi L_D}{2}-\omega\right)\cdot\left(b-\frac{L_D}{2}\right)-\omega\cdot L_D \tag{3.7}$$

The solution is easily computed as:

$$\omega=\frac{1}{2}\Delta\chi_D L_D\frac{b-a}{L} \tag{3.8}$$

and hence, the increase of displacement at the mid-point of the damaged zone, due to the curvature spike caused by the damage, holds:

$$\delta_D = \Delta\chi_D L_D \frac{L\left(2L - L_D\right)}{8L + 4L_D} \tag{3.9}$$

By assuming that the bending moment is approximately constant on L_D, the curvature spike $\Delta\chi_D$ can be evaluated in terms of section rigidity variation:

$$\Delta\chi_D(a) = \frac{M(a)}{EJ_D} - \frac{M(a)}{EJ_0} = \chi(a)\cdot\left(\frac{EJ_0}{EJ_D} - 1\right) \tag{3.10}$$

where EJ_0 is the section rigidity of the undamaged zones, while EJ_D is the one of the damaged part.

In conclusion, the shifted frequency due to the localized damage can be evaluated from the total displacement $\delta_0 + \delta_D$ of Eq. (3.5) and (3.9), in which the curvature spike is expressed as in Eq. (3.10); by factoring out the original first frequency, the damaged one holds:

$$f_D = f_0 \cdot \left[1 + 12\frac{L_D}{L}\cdot\frac{2L - L_D}{8L + 4L_D}\cdot\left(\frac{EJ}{EJ_D} - 1\right)\right]^{-1/2} \tag{3.11}$$

A previous approximated version of this formula considered the rotation $\Delta\chi_D L_D$ concentrated in a hinge [206]. It has been extensively checked by the authors through numerical simulations, showing very good predictive behaviour even in the case of circular arches [206].

Calculation of the damaged length

The evaluation of the damaged length requires the consideration of the bending moment distribution across the beam. When a beam is loaded in laboratory experiments, the positions of the forces are fixed, so that the bending moment varies proportionally among beam sections. However, in a real bridge beam, the diagram varies in a domain encompassing all cases from the dead weight distribution, to the load pattern of maximum intensity and extension in the serviceability conditions.

The damage in the beam cross-sections occurs as an irreversible phenomenon once the cracking moment is exceeded under any of the possible loading patterns. If the maximum bending

moment experienced by the beam is indicated as M_{max} and the cracking one as M_{cr}, the damaged length can be easily evaluated, if the shape of the diagram is known.
In the two relevant cases of uniformly distributed load and four-point bending tests (4PBT) with a load spacing *c*, the damaged lengths are computed as:

$$L_D = L\sqrt{1-\alpha} \text{ (uniform load)} \tag{3.12a}$$

$$L_D = c + (L-c)(1-\alpha) \text{ (4PBT)} \tag{3.12b}$$

Where α is the ratio $M_{cr}/M_{\max}$. If we consider a reference load distribution, with an amplification factor λ holding 1.0 when the yielding condition of the beam mid-span section is met, the link between α and λ is easily established:

$$\lambda = \frac{M_{\max}}{M_y} = \frac{M_{\max}}{M_{cr}} \cdot \frac{M_{cr}}{M_y} = \frac{\lambda_{cr}}{\alpha} \tag{3.13}$$

The ratio λ_{cr} is expressing the fraction of the maximum load causing the first cracking of the beam.
In [191], [196]–[204] the distributions of the beam section rigidity at different load levels have been reconstructed based on complete dynamic investigations. It is clearly shown that the damaged length is evolving up to 70% - 80% of the whole length approaching the yielding of the reinforcement. When $M_{\max}$ attains the yielding value, α decreases to λ_{cr} with values in the range 0.20-0.30. As is indicated by Eq. (3.12a), the damaged length increases to $L\cdot(1-\alpha)$, i.e. more than 70% of the beam length.

Calculation of the damaged section rigidity

The calculation of the rigidity of the damaged sections requires the consideration of the loading path in the beam. Once the loading history pushes the bending moment distribution above the boundary of the local maxima experienced in the past, the size of the damaged region increases and the rigidity decreases. However, the load at which the beam frequency is measured is normally near to the case of dead load only. Consequently, the damaged rigidity depends on the maximum moment that occurred on the beam section, and this rigidity is larger than the tangent one given by the fully cracked section (see for instance [207]).
A detailed description of the rigidity evolution can be found in [207], [208] as a function of the initial rigidity EJ_0 and the fully cracked section rigidity EJ_T. It is evident that bridges subjected

to self-weight, with cracks formed by the previous loading history, will show beam stiffness values related to the section rigidity of the unloading branch (Figure 3.41).

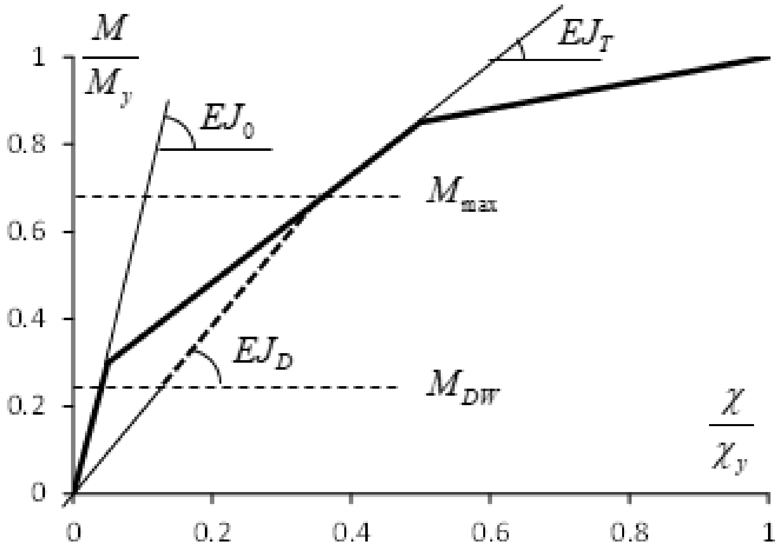

Figure 3.41. Calculation of the damaged rigidity in the Moment-Curvature diagram.

The secant rigidity is easily calculated from geometrical considerations:

$$EJ_D = \frac{M_{\max}}{\dfrac{M_{cr}}{EJ_0} + \dfrac{M_{\max} - M_{cr}}{EJ_T}} = \frac{EJ_T}{1 - \alpha\left(1 - \dfrac{EJ_T}{EJ_0}\right)} \tag{3.14}$$

The smooth variation of the section rigidity after the first crack is pointed out in experiments described in [191], [206], where the evolution of the dynamic modulus is obtained from experimental data. This can be related to the progressive reduction of the concrete tension stiffening when the bending moment increases up to the yielding limit.

Frequency shift in a damaged beam

Consider a beam progressively damaged by increasing the load on it, but its natural frequency is measured in a reference situation with only the dead load present on the beam. Then the previous analyses can be linked together to derive a general formula for the natural frequency of a cracked beam, based on the load level experienced in the past by the beam. This is easily worked out by introducing in Eq. (3.11) L_D and EJ_D defined by Eq. (3.12a) and (3.14) in terms of α and λ.

As a particularization, a localized damaged zone is considered at the mid-span of the beam, caused by a concentrated load, such that $L_D = L \cdot (1- \alpha)$. By introducing in Eq. (3.11) the cited expressions, the shifted frequency is obtained as a function of α:

$$f_D = f_0 \cdot \left[1 + 12 \frac{(1-\alpha)^2 \cdot (1+\alpha)}{12 - 4\alpha} \cdot \left(\frac{EJ_0}{EJ_T} - 1 \right) \right]^{-1/2} \tag{3.15}$$

This damaged frequency is valid only when the cracks do not close during the vibration. This is the case for example of a running truck over a bridge such that the dynamic motion occurs without any upward displacement.

In most experimental tests in which the frequencies are recorded with the bare structure under the dead loads, the dynamic motion occurs with the opening and the closure of cracks, and therefore the non-linear effect of the crack face changing contact has to be considered.

The effect of breathing cracks

In literature, the phenomenon of crack opening and closure during the dynamic motion is named "breathing crack". The very first studies were motivated by some fatigue crashes of rotors used in the energy production plants. *Chondros* [209] presented a detailed analysis of the simply supported beam with a crack, showing the difference in response when the crack is open or breathing. One interesting comment of *Tan* [199] is based on *Bendat*'s well-known book [210]. It states that the interpretation of breathing cracks by using bilinear crack constitutive laws, will not produce a non-linear behaviour. It can be concluded that the non-linear content of a breathing crack is concentrated only in the contact and release phases. This is evident from the steady vibration (Figure 3.42) and phase diagrams (Figure 3.43) reported from [211], in which the average harmonic behaviour is added.

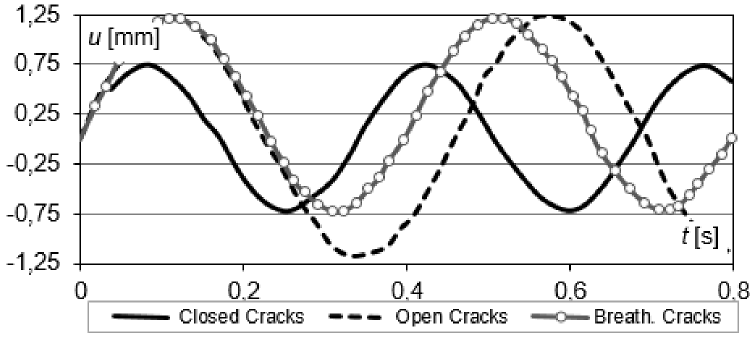

Figure 3.42. The steady vibration of cracked sections (from [212]). The breathing crack response has a period near the average of the open and closed ones.

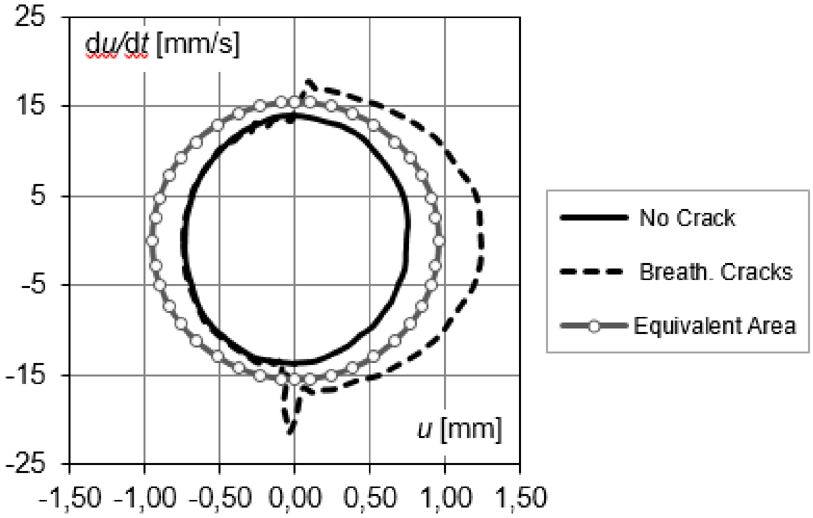

Figure 3.43. The phase plot of the previous signals (from [212]). The average harmonic oscillation of an equivalent linear system is obtained by an equivalent area.

In terms of the effect of a single crack, a suitable interpretation is possible based on the evaluation through the static equivalence. In a damaged vibrating element, the kinetic energy is constant during the oscillation inside the open or closed cracks phases, apart from the dissipation occurring during the locking – releasing phases. Then it exits an average frequency with which the energy is transferred between the two configurations.

A very simple interpretation is based on the assumption that the maximum displacement experienced by the beam during the oscillation is given by the cracked section rigidity when the motion releases the cracks, and by the original solid section rigidity when the motion evolves with locked cracks.

Since these two deformed states are produced by the same energy, the breathing crack response is obtained by averaging the two displacements (*b*=breathing, D=open, 0=closed):

$$f_b = \sqrt{\frac{2g}{\delta_0 + \delta_D}} = \sqrt{\frac{2 f_0^2 f_D^2}{f_0^2 + f_D^2}} \tag{3.16}$$

As a matter of example, some investigations reported by Chondros & Dimarogonas [209] are considered. In the following Table 3.9, the frequency ratios are listed for the three considered cases as a function of the non-dimensional crack size *w/h*; the error resulting from Eq. (3.16) appears very small.

Table 3.9. Comparison of experimental data from Chondros [209] and Eq. (3.16).

w/h	Closed crack	Open crack	Breathing crack	theory	error
0.00	1	1.000	1.000	1.000	0.00%
0.12	1	0.975	0.990	0.987	0.28%
0.20	1	0.941	0.980	0.969	1.09%
0.28	1	0.919	0.979	0.957	2.20%
0.32	1	0.860	0.937	0.922	1.56%
0.42	1	0.818	0.911	0.895	1.70%
0.56	1	0.693	0.855	0.805	5.81%

The extension of the proposed formula to a beam with several cracks affecting the central part of the structure is based on a very simple deduction. Since Eq. (3.11) evaluates the increase of displacement for any extensions of the damaged length, it holds even for the case of multiple adjacent cracks and provides the vibrating frequency of a beam with several always open cracks of Eq. (3.15).

Therefore the averaging of the two displacements generated by the same kinetic energies is correctly carried out by Eq. (3.16), irrespective of the extension of the cracked length.

The static equivalent displacement is easily computed even by considering complex mechanical models of the cracked RC beam that take into account different degradation phenomena such as corrosion or cyclic loading.

For example, the proposed combination formula (3.16) can easily deal with the stiffness degradation due to fatigue of the cracked beam caused by a large number of load repetitions. As a matter of fact, *Kim* [211] reported experimental values of frequency variation with the number of loading cycles, obtaining a significant decay:

Table 3.10. Data of the fatigue frequency decay given by *Kim* [211].

Load Cycles [n]	Frequency [Hz]	Decay [%]
0.00	45.35	0.00
$0.20 \cdot 10^6$	39.29	13.36
$0.35 \cdot 10^6$	35.28	22.21
$2.00 \cdot 10^6$	32.13	29.15

It is easy to compare the frequency decay Δf of the measured frequency $f(n)$ at n cycles, with the reduction of the stiffness $k(n)$ extracted from the experimental displacements after n loading cycles. By computing the frequency variation as the square root of the stiffness variation, the comparison of Table 3.11 is obtained.

Table 3.11. Comparison of static and dynamic experimental data from [211].

n /10^6	k(n)/k(0)	f(n)/f(0)	Err_f	Exper.	Error
0.00	1.000	1.000	0.0%	-	
0.10	0.763	0.874	12.6%	-	
0.20	0.691	0.831	16.9%	13.4%	26.0%
0.35	0.571	0.756	24.4%	22.2%	10.1%
0.60	0.459	0.678	32.2%	-	
1.00	0.460	0.679	32.1%	29.2%	10.3%
2.00	0.460	0.681	31.9%	29.2%	9.4%

It is to cite that the effect of breathing cracks can be inferred even indirectly from literature results. For example, consider the data of *Xu & Castel* [208]; they introduce a crack stiffening factor D_{cc} that is in the range {0, 1} with increasing values corresponding to an increase in beam deformability. The presented static loading cycles show the best fit with D_{cc} = 1 while the vibration frequencies are in agreement with D_{cc} = 0. The discrepancy can be easily explained by the stiffening effect of the breathing cracks, which let appear the beam deformability in dynamic motion be lower than expected from static loading tests.

In what follows the formula (3.16) will be extensively used in the comparison of a wide set of data previously discussed, with a very good general agreement. Concerning the interpretation of the frequency evolution in RC beams with the cracking stages, very few numerical models that consider breathing cracks are present in the literature.

The comparison of the proposed analytical interpretation is, in any case, in very good agreement even with existing numerical solutions. A precise evaluation of the breathing crack phenomenon in terms of FEM models will be presented in what follows.

Comparison of the theory with experimental literature results

The data presented earlier have been organized by performing the average of the results of each experimental investigation [191], [196]–[204]. The experimental curves are compared with the solution of Eq. (3.15) (no crack closure), and with the solution with crack breathing included, as in Eq. (3.16). In particular, by merging the two formulas, the following opening-closing crack formula is obtained:

$$k_b = \frac{f_b}{f_0} = \sqrt{\frac{2}{2+12\eta \frac{(1-\alpha)^2 \cdot (1+\alpha)}{12-4\alpha}}} \tag{3.17}$$

η is the factor $\left(\frac{EJ_0}{EJ_T} - 1 \right)$, normally in the range {0.7, 1.5}, and α is obtained as λ_{cr} / λ by Eq. (3.13). Figure 3.44 shows the comparison.

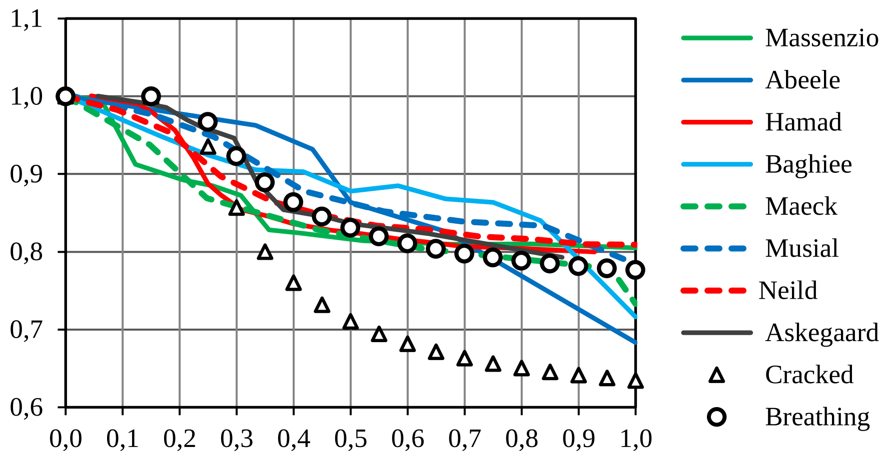

Figure 3.44. Load – Frequency plot of the proposed theory compared with the experimental tests.

The collected data can be approximated by using a logistic function. By performing a best fit analysis, the following form is obtained:

$$k_D(\lambda) = \frac{f_b}{f_0} = 1.025 - \frac{0.25}{1+9 \cdot e^{-6.6\lambda}} \tag{3.18}$$

The error of the suggested interpolation form concerning the whole data set is, on average, less than 0.33%. A numerical evaluation of the breathing crack phenomenon has been proposed by *Gao et Al.* [213], by using an Expanded Distinct Element Method (EDEM). The software UDEC is used in forming a particle swarm mesh with connecting non-linear springs. The best fit interpolation, the EDEM solution [213] and the analytical representation are compared in Figure 3.45.

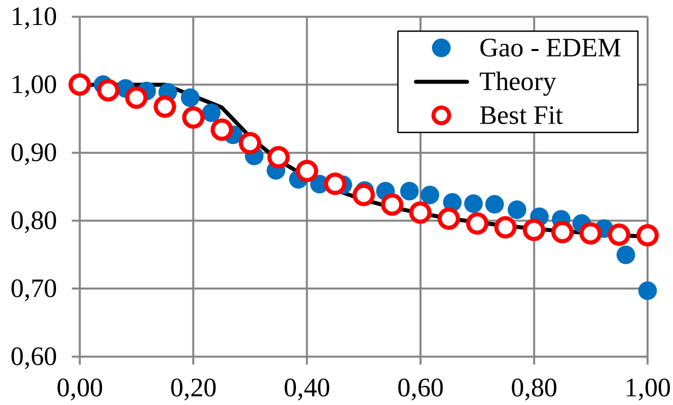

Figure 3.45. Comparison of the proposed model with the best fit of data and a numerical model.

As is evident, the agreement among the three solutions is noticeable.

A simple approximated formula can be obtained by developing in series the function α given in Eq. (3.17) around the value 1.0, i.e. when λ is near λ_{cr}:

$$\lambda = \frac{\lambda_{cr}}{1-\sqrt{\frac{2}{3\eta}\cdot\frac{1-k_D^2}{k_D^2}}} \tag{3.19}$$

By assuming by definition that λ holds 1.0 when the reinforcement is at the limit stress, this formula allows evaluating $k_{D,\min}$, in terms of λ_{cr} and η only:

$$k_{D,\min} = \frac{1}{\sqrt{1+1.5\cdot\eta\cdot(1-\lambda_{cr})^2}} \tag{3.20}$$

The formula (3.20) gives an approximated bound of the frequency shift that is to be expected when the beam enters the collapse phase.

Verification by a new test

The previous theory has been verified with some experimental tests and numerical simulations completed by the authors. In particular, some concrete beams with dimensions 150x200x2200 mm^3 were tested and simulated with different models to verify the proposed analytical results. The laboratory tests concerned beams loaded in a 4PBT set up at different load levels up to yielding of the reinforcement. The loads corresponding to the cracking moment (M_{cr}) and the yielding moment (M_y), resulted in a maximum shear of 20 and 70 kN, respectively (Figure

3.46). Before and after the loading test, a set of signals given by ambient vibration were acquired and processed to extract the frequency content.

Figure 3.46. Load cycle of the 4PBT performed on the experimental beam up to reinforcement yielding.

The vibration tests have been validated with three non-linear finite element models, namely: the solid beam, the beam with cracks steadily open and the one with breathing cracks.
The three FE models shown in Figure 3.47 have been created by considering the crack pattern of the real beam as a reference to place the cracks at a realistic distance along the beam. The behaviour of the breathing cracks has been modelled by using compression cut-off elements filling the slots simulating the cracks. The steel rebars have been included in the model by introducing truss elements at the distance from the beam bottom equal to the cover.

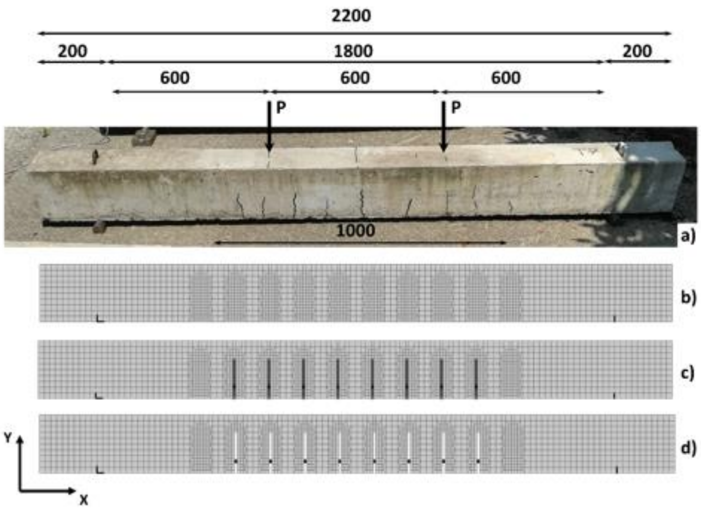

Figure 3.47. Sketch of the loaded beam (a) and the three numerical models: solid beam (b), beam with compression-only contact elements (c), beam with steadily open cracks (d).

The bar debonding in the cracked zones has been simulated by considering a total length of 70 mm of the bars, bridging over the slots included in the numerical models. The data of the beam and the parameters that characterize the numerical models are listed in Table 3.12.

Figure 3.48 shows the FFT spectra of the non-linear calculations. Table 3.13 compares the experimental values with the numerical values and the predictions given by the proposed formulas. A very good agreement can be observed among the three different analyses. As is evident, the breathing crack hypothesis is supported not only by analytical theory but also by the non-linear numerical models. Furthermore, the proposed model mock-up can be easily extended to more complex situations in order to study non-linear vibration problems.

Table 3.12 Materials of the beam and parameters assigned to the models.

Material	Class	fk [MPa]	E [MPa]	ρ [kg/m^3]	As [mm^2]	Ac [mm^2]
Concrete	C 20/25	20	29500*	2400	-	30000
Steel	B450C	450	210000	7850	226	-
Link	Compr. Only	20	20000	2400	-	1500

* Value determined from ultrasonic tests

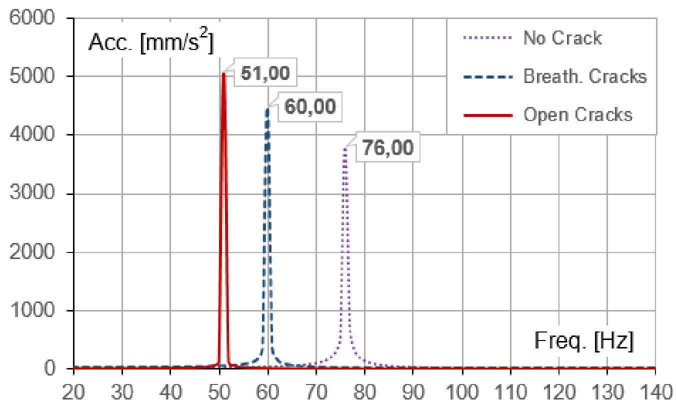

Figure 3.48. Comparison between the fundamental frequencies of the three numerical models.

Table 3.13. Comparison among the experimental frequencies and the numerical model results.

Crack	Dyn. Test	FE model	Err	Eq. (3.16)	Err
Solid	75.60	76.00	0.53 %	79.00	4.49 %
Breathing	59.96	60.00	0.06 %	60.80	1.40 %
Open	51.21*	51.00	0.41 %	51.90	1.34 %

* Value obtained through the eq. (3.16)

Further investigations on concrete beams

The original set of concrete beams consisted of four beams with the same geometry and materials. One of them has been identified as the reference beam associated with the undamaged condition, and then the other three beams were loaded according to the setup illustrated in Figure 3.47 with a length equal to 2.0 m instead of the original 1.8 m aiming lower frequencies. Concerning the load exerted on the beams during the 4PBT, 50 kN, 62 kN, and 70kN have been set as the load for achieving the values of bending moment corresponding respectively to the stabilization of the cracks in concrete, the yielding moment and the failure bending moment. The experimental load-displacement curves are illustrated in Figure 3.49.

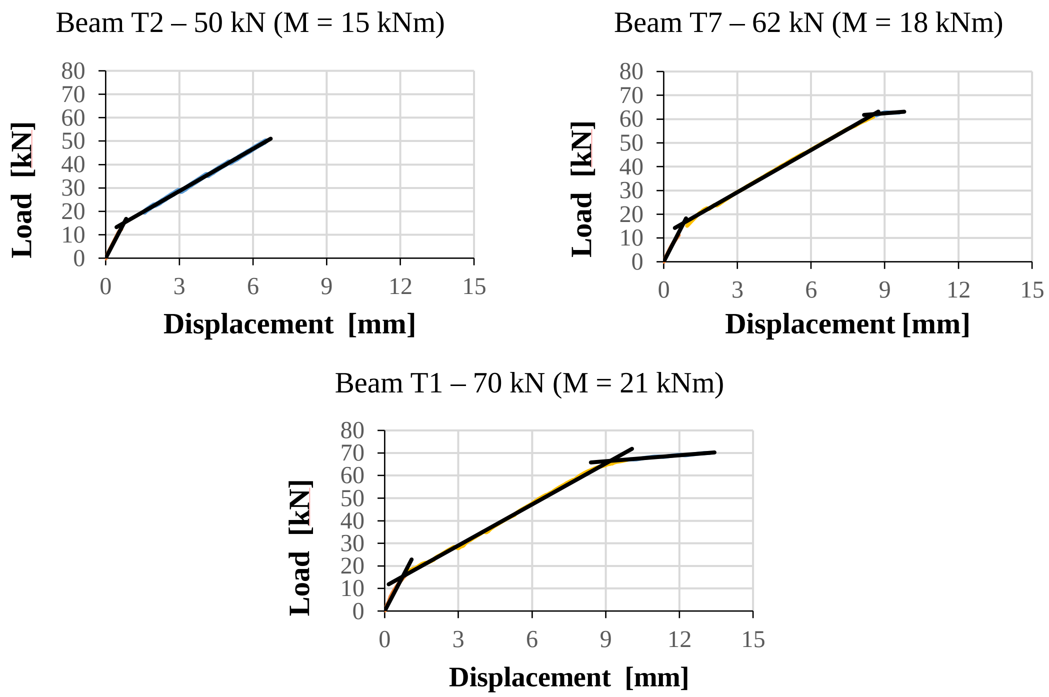

Figure 3.49 Load-Displacement curve from the 4PBT

Even in the current stage, all the dynamic tests have been performed collecting the acceleration with 2 CX1 tri-axial accelerometers. The first one is at the beam midspan, whereas the other is at one-quarter of the beam length. The analysis of the frequency content of the accelerometric signals measured on the undamaged beam (D0) led to three main frequencies equal to 53.22 Hz, 72.63 Hz and 98.88 Hz. The second one is associated with the first vertical bending mode of a simply supported beam, while the other two are respectively the first and second bending modes out of the vertical plane.

The aim of the study is the detection of the frequency decay induced by progressive damage states. Indeed, naming D1, D2, and D3 the damage states associated with the three levels of load, the evolution of the first three main frequencies led to the plots of Figure 3.50 which suggest a quite linear dependence of the lateral bending modes with the increasing severity of the damage. On the other hand, the vertical bending mode follows frequency decay similarly to what was discussed previously. Lastly, even the frequency reduction induced by cyclic loads is investigated: after the firsts load cycles leading to the cracking of the beam and the aforementioned maximum loads P_{max}, further load cycles in the range 0-P_{max} have been carried out on the concrete beams increasing the level of damage. The evolution of the first three frequencies corresponding to 1, 100, 1000, and 10000 cycles have been tracked and then plotted in Figure 3.51.

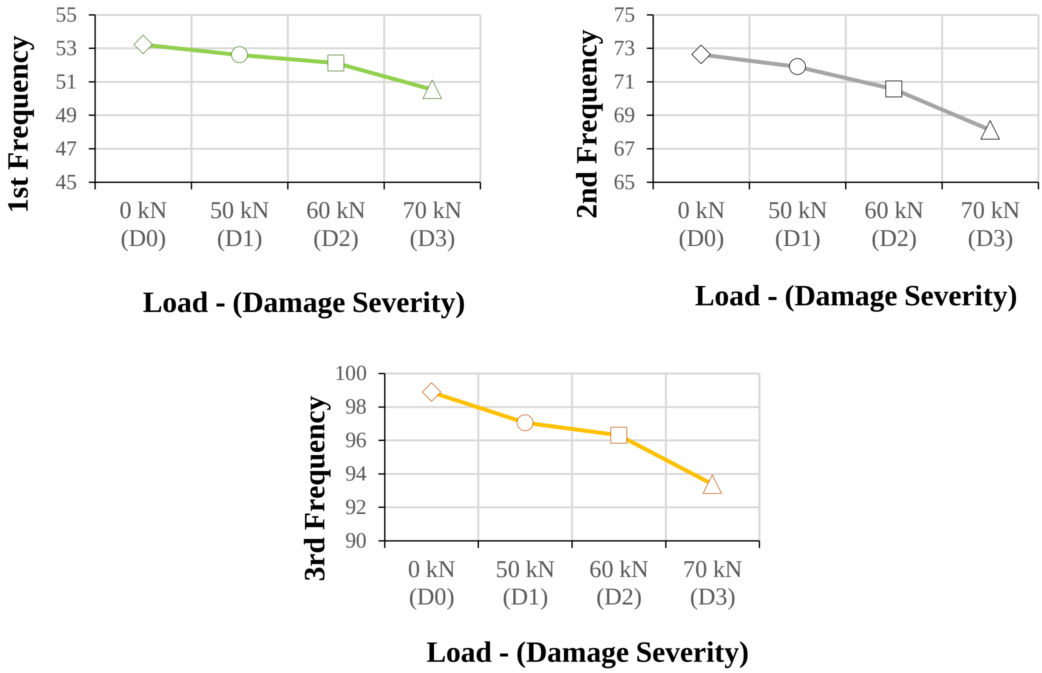

Figure 3.50 Frequency decay over the damage severity (Load)

The three plots show a similar reduction of all the three frequencies associated with the same load, even if at a certain time a diagonal crack occurred during the load tests and a biased last frequency has been collected for the beams D1 and D3. It is the reason that only the frequencies associated with 100 and 1000 cycles of beam D1 have been collected in the plot.

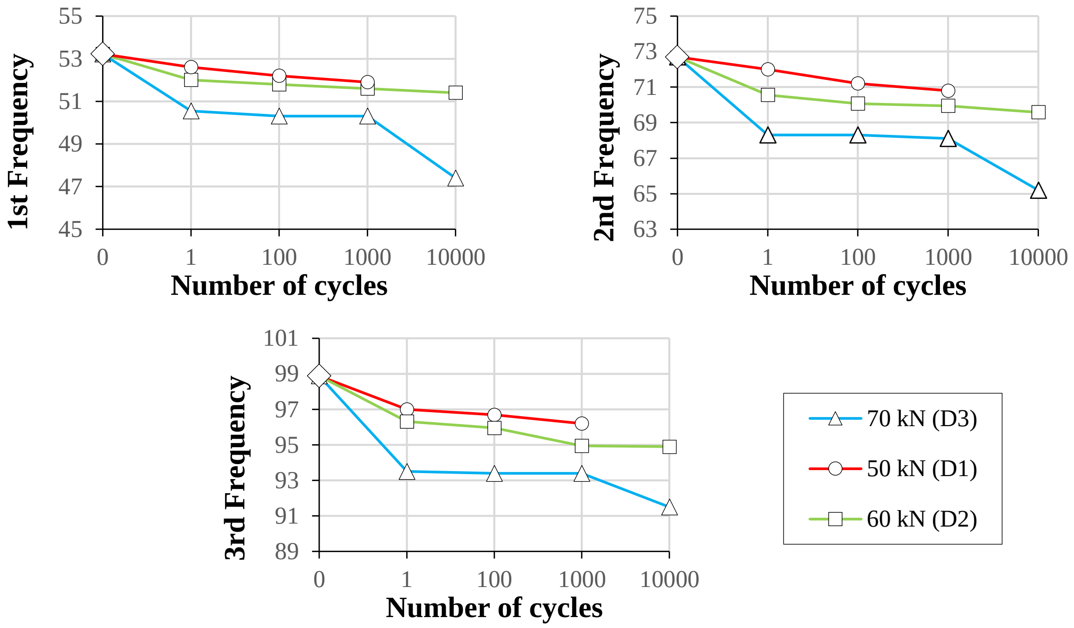

Figure 3.51 Frequency decay over the damage severity (n° Cycles)

Validation of a hybrid sensor network developed in Bologna

Contextually to the previous experimental campaign, another concrete beam with the same geometry is chosen for validating the performances of a small-sized sensor network (SHM–Lab) developed within the SHM research group of the Advanced Research Center of Electronic Systems (ARCES) of the University of Bologna concerning the outcomes provided by the commercial systems. The two networks addressed two issues: firstly, accelerations have been recorded by some accelerometers aiming at the assessment of the dynamic behaviour of the beam in its undamaged configuration. Then a set of Piezo-electric sensors is used for detecting acoustic emissions induced by the crack occurrences during a loading phase.

- **SHM–Lab system:** The SHM–Lab system is a hybrid sensor network (SHM–Lab) based on three groups of elements: two series of compact sensor nodes, one based on a lead-zirconate-titanate (PZT) piezoelectric transducer and another on a triaxial MEMS inertial measurement unit (ACC), and a network interface, also called gateway. All these devices are connected in a daisy-chain fashion through a Sensor Area Network (SAN) bus exploiting data-over-power (DoP) communication. Meaningful information is transmitted to a PC connected through the gateway employing a lossless encoding technique. The wired connection here adopted is chosen to ensure highly synchronized data acquisition, with a synchronicity error lower than 50 μs. Synchronization between measurements is a fundamental concern in the majority of applications, such as vibration-based inspection techniques, in which it was found [214] that the maximum tolerable delay should be inferior to dozens of μs avoiding alteration in the accuracy of processed data.

  The inertial node is designed to gather highly accurate acceleration data thanks to a maximum dynamic range programmable from ±2 to ±16 g, coupled with a linear sensitivity of 61 μg/LSB and a high-performance mode noise density of 80 μg/√ Hz. The angular counterpart operates with a gyroscope sensitivity of 4.375 mdps/LSB, an angular velocity range varying from ±125 to ±2000 dps and a noise level of 4 mdps/√ Hz. Available Output Data Rates (ODR) for both the linear and angular acquisitions are comprised between 12.5 Hz and 6.664 kHz, with a flat frequency response in the whole sampling band, specifically including also the zero Hz static component. It is worth underlining that the network is designed to be extremely versatile and tunable in each specific application context, being the operational parameters completely reconfigurable in real-time. As a result, the SHM–Lab inertial equipment is compliant with the design and operative parameters stated in [215] about electronics for civil SHM applications. The core of the PZT sensor node is a STMicroelecronics mixed-signal STM32F3 microcontroller unit (MCU), which also integrates high-performance analogic circuitry, i.e. comparators, amplifiers, analogic–to–digital, and digital–to-analogic converters. The PZT sensor node features three acquisition channels connected to a custom-designed, multi-electrode PZT transducer with a flat frequency response over a large frequency band. Each transducer is connected to an embedded Programmable Gain Amplifier (PGA) which provides nine different gain levels, from ×1 to ×23. Each analogic signal is then sampled by an embedded 12 bit, rail-to-rail ADC with a programmable sampling frequency up to 800 kHz. A 128 KiB SPI serial SRAM is used for data storage while program instructions are stored in the MCU embedded 256 KiB flash.

The PZT and ACC sensor nodes share the same architecture, lightweight (4 g), small size 201 (30 mm × 23 mm) and low power consumption (40 mW). Thanks to the units embedded in the MCU, capable of DSP and FPU instructions, each node, independently form the sensing technology adopted, can autonomously process onboard the recorded signals.

- **Commercial systems:** It includes the CX1 Accelerometer previously introduced and the Vallen Acquisition system. The AMSY-5, developed by Vallen Systeme, is an AE multi-channel system. This instrument provides a complete analysis of the AE phenomena inside different kinds of structures. Each channel consists of an AE sensor, a pre-amplifier, which could either be external or internal to the AE sensor and an Acoustic Signal Processor (ASIP), which is the core of the platform. The ASIP embeds an analogic signal conditioning circuit to maximize the signal-to-noise ratio of the input signals. Before passing through an integrated 16 bit ADC, a bandpass filter is applied to the incoming signals both for noise reduction and anti-aliasing purposes. The main AE signal features, such as the time of arrival, the amplitude and the duration time, are extracted by the processor at a sampling rate of 20 MHz. In parallel to the feature extraction block, a burst signal can be recorded up to 5 MHz and stored into the internal memory. To control every aspect of the measurement process, front-end software running on an external PC is interfaced with the AMSY-5. The resulting AE parameters can be plotted in diagrams and manipulated through a user-friendly GUI. Vallen

Systeme also provides all the necessary tools to perform AE analysis, such as PZT transducers, amplifiers, and clamps. In particular, the VS-150RIC sensor, used in the experimental setup, is a piezoelectric AE-sensor with an integrated 34 dB gain pre-amplifier. It is suitable for almost all AE applications due to the wide frequency band, with a resonance peak at 150 kHz.

Dynamic tests, as well as AE tests and the four-point bending test (4PBT) here, performed involved two identical simply supported RC beams, with a cross-section area of h =150 mm x b =200 mm and a free span length L =2000 mm. One of the beams (DB) is already damaged with a uniformly distributed crack pattern, whereas the latter (UDB) is not damaged.

As displayed in Figure 3.52(a), both the specimens were reinforced with two 12 mm diameter reinforcing bars inserted in the top and bottom layers, with 40 mm of nominal cover at each side of the structure and a series of 8 mm stirrups placed at a step of 200 mm along the beam length.

While the Poisson's ratio and the density of the concrete were assumed as $\upsilon = 0.2$ and ρ =2500 kg/m3, respectively, Young's modulus was estimated experimentally by performing ultrasonic tests. The procedure involved the following steps: (i) considering that ultrasonic waves (UWs) propagate across the beam section with a specific Time of Flight (ToF), UWs were firstly measured along with the main directions of the beam plus several horizontal positions; (ii) secondly, the dynamic elastic modulus was estimated as $E = v^2\rho$. As usual, the value of the static elastic modulus is roughly 30% lower than the dynamic one, which consequently yielded an experimental Young's modulus of 29500 MPa, Considering typical concrete of class C 20/25.

With the primary aim of assessing the accuracy in modal parameters estimation, the vibrational behaviour of the UDB beam was simulated based on a bi-dimensional Finite Element (FE) model created with the FE software STRAND. The specimen was discretized into 44 beam elements sliced with a uniform offset of 75 mm, equal to half of the beam depth. Each of these elements is modelled 261 adopting the geometrical properties of Figure 3.52, while its flexural rigidity EJ was assumed to equal to $1{,}02\cdot10^6$ Nm2. The distance between the supports, together with the centre of gravity of the cross-section was also taken into consideration; the vertical direction was fixed at both of those supports. The numerical simulation output two main vertical bending modes corresponding respectively with $f_{1,\ \text{flexural}}$ = 45,80 Hz and $f_{2,\ \text{flexural}}$ = 182,42 Hz, whose respective modal shapes are drawn in Figure 3.52. Since the spectra computed during a preliminary frequency investigation evidenced also a peak at 15 Hz due to the loading frame, one elastic spring with stiffness of 1480 kN/m was included in the model to simulate the effect of the flexibility of the loading frame carrying the beam and responsible for spurious vertical modal displacements at the beam's ends in the following (Figure 3.55).

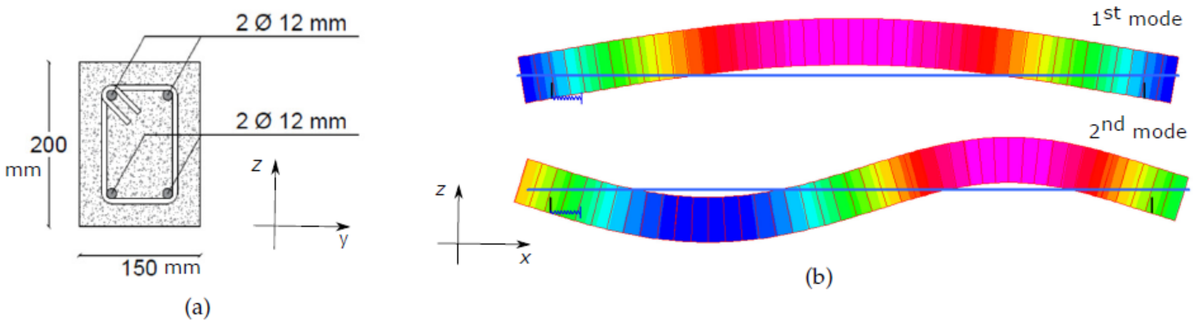

Figure 3.52. (a) Schematic view of the cross-section area and (b) theoretical modal shapes related to the first two flexural modes on the x-z plane.

The installed monitoring equipment comprises five SHM–Lab inertial sensors, glued on the upper surface of the beam (Figure 3.53a) and uniformly distributed at the nodal and antinodal points of the first two flexural frequencies. In compliance with the maximum admitted sample number for the simultaneous collection of 3D accelerations and 3D angular velocities from 6 channels [216], SHM–Lab sensors were configured to gather 2500 data points. Full-scale ranges of ±2 g and ±125 dps were imposed to capture the linear dynamic ranges obeying the expected dynamic response. A data rate $f_{s,ODR}$ = 3,33 kHz was chosen among all the available settings as the closest sampling frequency higher than the one of the used reference commercial sensor. Considering an effective signal bandwidth of 200 Hz, recorded data were then smoothed and downsampled to a sampling frequency of $f_{s,SHM}$ = 1 kHz thus providing an oversampling ratio of 2.5. Concurrently, two CX1 Sensr accelerometers were installed respectively at the mid-span and a quarter of the total length, hence increasing the accuracy in the detectability of the second mode of vibration. The maximum allowable sampling rate $f_{s,CX1}$ = 2 kHz and acceleration range of ±1.5 g were adopted.

The beam finally resulted to be instrumented as reported in Figure 3.53b.

The RC beam was repeatedly excited by hitting the top surface of that beam in several positions depending on the specific modal shape to be evidenced. Both the networks were programmed to acquire samples simultaneously. The analysis of the signals recorded by CX1 and SHM–Lab was intentionally limited to the same time frames recorded by both the devices. Furthermore, a pre-processing step was considered for the extraction of solely the ambient vibration of the beam, a procedure which is recommended in OMA processing [181] to filter out spurious frequencies which can be induced during the shaking itself.

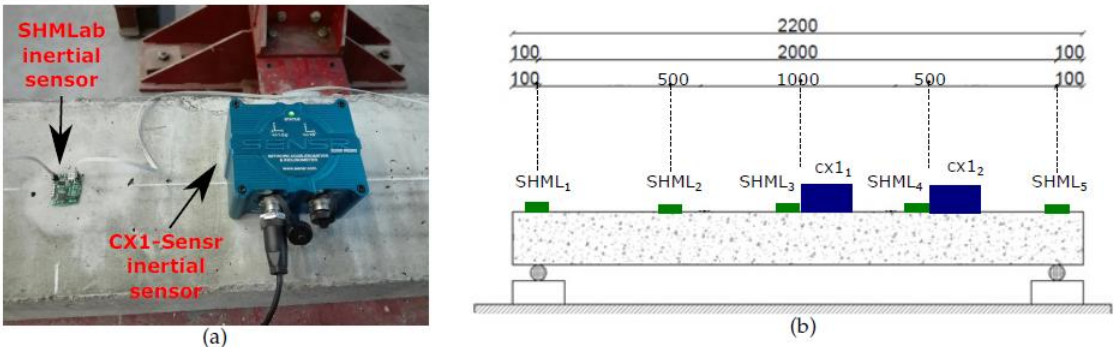

Figure 3.53. Experimental setup aiming at performing a preliminary vibration-based analysis of the undamaged beam: (a) inertial SHM–Lab prototype (left) and CX1-Sensr accelerometer (right) instrumentation installed on SD for vibration-driven structural inspection and (b) sensor deployment.

From a signal processing perspective, the spectral content of the in-plane orthogonal a_x and a_z accelerations, respectively collected along the longitudinal and vertical axis, were primarily processed for the computation of the Power Spectral Density (PSD). Spectra were extracted through the non-parametric Welch's estimator, deemed as a powerful spectral tool whenever a reduction of the noise floor is desired. This is the case of RC structures, where noise could even exceed meaningful signals in the case of low-amplitude vibrations. Subsequently, the experimental modes of the beam were considered coincident with the most energetic peaks crowding spectral trends. This kind of investigation was performed in parallel on time series deriving from the two acquisition networks.

Secondly, even if modal displacement curves can provide important spatial-dependent information about structural integrity, their extraction implies a highly dense engineering plan. Beyond the high-resolution and great sensitivity of the commercial instrumentation exploited, it still represents an expensive solution that may limit the number of devices to be concurrently installed. Consequently, the sensor-grid here obtained after CX1 deployment was not sufficient to precisely inspect modal shapes about the minimum spatial resolution and number of acquisition points. For this reason, the reconstruction of the first two flexural modal shapes only involved vibrations collected using SHM–Lab's architecture. In particular, among the available algorithms theorized for the extraction of modal coordinates, the classical Frequency Domain Decomposition (FDD) [181] technique and the Second Order Blind Identification (SOBI) method [217], the latter belonging to the class of unsupervised modal approaches, were considered. Finally, a quantitative measure of modal correspondence between empirical and simulated displacement curves was point-wise calculated according to Modal Assurance Criterion (MAC) [187].

Spectral trends computed through Welch's algorithm along the x and z direction axis are shown in Figure 3.54, in which the upper line is related to samples coming from SHM–Lab architecture, whereas the lower graphs pertain to commercial CX1 accelerometers' signals. Proved by a clear vertical alignment between dominant peaks, the most important outcome of such an analysis concerns the extreme level of consistency between research and commercial equipment, the main difference among them being fundamentally a matter of smoothness associated with the available number of samples. More precisely, the ratio between the chosen sampling rate and the length of the observed time window was fixed to ensure an identical frequency resolution, yielding the amount of CX1 data inside each frame to double that recorded employing SHM–Lab sensors.

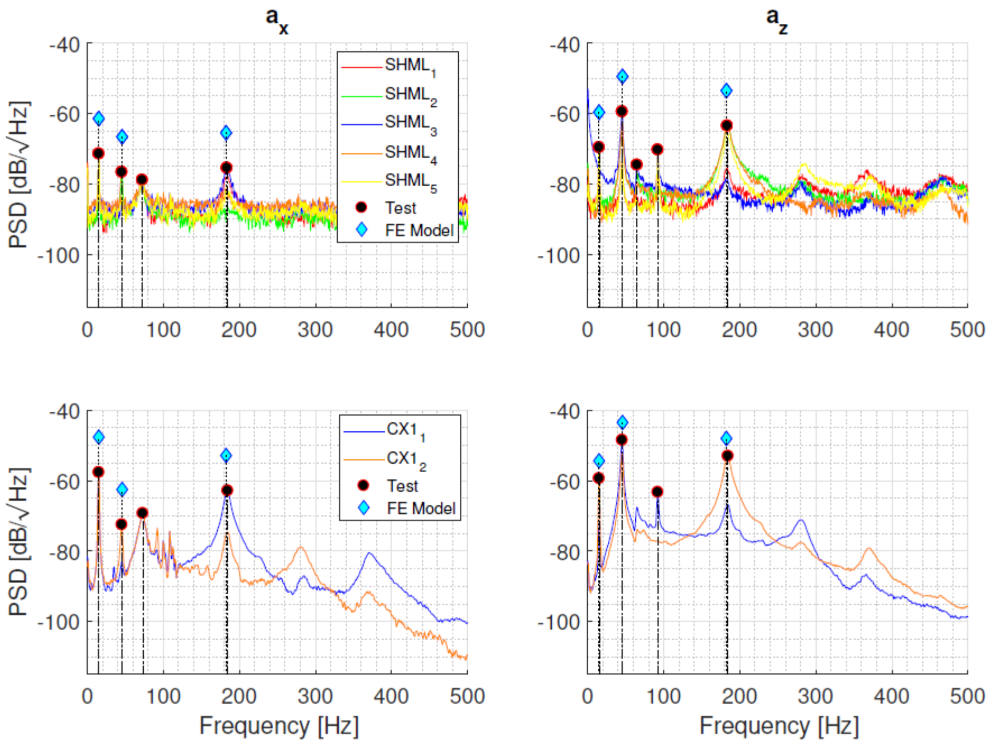

Figure 3.54. Natural frequencies estimation: comparison between PSD trends obtained with SHM–Lab instrumentation (upper plots) and commercial CX1 sensor nodes (lower plots).

Extending the comparison, two additional factors need to be underlined. The former concerns a minor difference in the signal-to-noise ratio, which appears slightly lower in SHM–Lab-driven spectra. Such a deviation is globally quantifiable in less than 5 dB/√ Hz and can reasonably depend on the intrinsically higher noise density of the prototype device. Similarly, the second aspect characterises the magnitude of computed spectral signatures: CX1-gathered signals appear at least an order of magnitude (i.e. an amplification factor almost equal to 10) more intensive than those collected by SHM–Lab nodes, probably related to a different signal conditioning strategy and sensitivity characterizing these two technologies. Nonetheless, apart from the aforementioned amplification coefficient, the noticeably equivalent shape and width of the dominant peaks ideally allows for an almost perfect superimposition between curves computed with quite different sensing architectures. The advantageous form factor of the former, whose state of development imposes a more stringent trade-off between time window and exploited storage capabilities, combined with its light-weight, high versatility and onboard processing capabilities, does not lose any significant structural information compared to the latter architecture, which provides longer time series at the expenses of a steady-deployed, invasive and more energy-consuming solution.

As a result, it may be argued that SHM–Lab inertial instrumentation can effectively compete with much more expensive and quite invasive commercial electronics. To address frequency estimation purposes, the relative error concerning theoretical predictions was assumed as the main metric of accuracy. Percentage variations are listed in Table 3.14, in which the highest deviation of SHM–Lab estimation inferior to 0.9% distinctly attests to its deep level of superimposition among empirical and simulated vibrational behaviour. Besides equivalent performance in detecting the in-plane fundamental modes, commercial sensors seem to capture a less precise response around the second flexural component. What's more, concerning both of the sensors, it is important to underline that additional frequency components crowd the spectra both in the vertical and longitudinal direction. Because of the sharpness and presence in all the produced spectra, these peaks could fairly be addressed to rigid motions. However, values reported again represent a direct quantification of the agreement between the employed networks, numerically enforcing their interchangeability for vibration-based monitoring plans despite their undoubtedly different features.

Finally, modal shapes were reconstructed concerning the first two flexural modes of vibration (Figure 3.55). Despite the smoothness of the curves, which depends on the interpolation method to be used, displacement shapes are totally compliant with numerical expectations. This observation is confirmed by MAC percentages listed in Table 3.14, from which it can be inferred how experimental data related to the first displacement curve fit the model almost perfectly. Conversely, a lower correlation index affects the second mode, primarily due to a major deviation occurring in correspondence of the fifth node. Additionally, it should be pointed out that the high synchronicity between sensors in data recording leads to a great coherence between supervised (FDD) and unsupervised (SOBI) techniques, verifying the suitability of the developed network to operate efficiently even in absence of any apriori structural information. This evidence supports the effectiveness of highly synchronized and tightly embedded circuitry to inspect the dynamic response of structures, extracting meaningful structural information even when signals exhibit weak amplitude.

Table 3.14. The relative error in terms of frequency for CX1 and SHM network and the MAC values concerning the modal component given by FDD and SOBI.

	Frequency		MAC	
Mode	**SHM–Lab**	**CX1**	**FDD**	**SOBI**
$f_{1,longitudinal}$	0.795%	0.795%	-	-
$f_{1,\ flexural}$	0.850%	0.850%	99.83%	99.79%
$f_{2,\ flexural}$	0.642%	0.642%	57.70%	58.88%

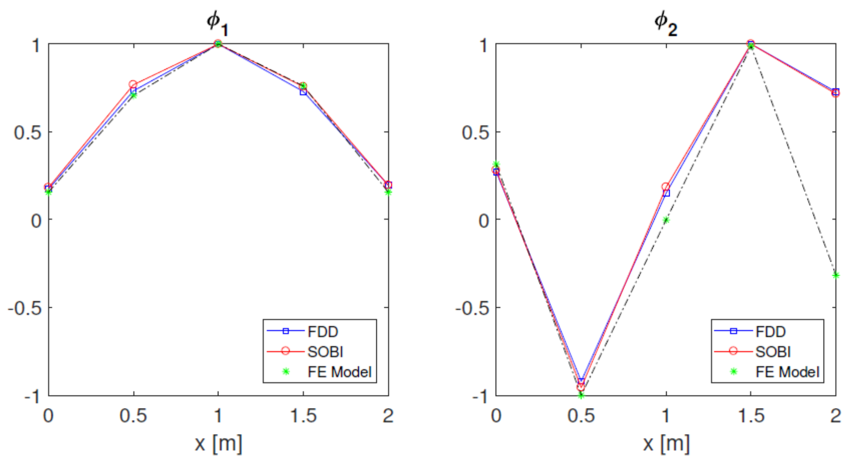

Figure 3.55. Reconstructed modal shapes related to the first two vertical modes.

Concerning the acoustic emission viewpoint, the most important AE parameters are extracted and further compared to those provided by commercial instrumentation (AMSY-5) which are taken as reference. In the NDE field, it is widely known that the estimation of damage in concrete structures may be correlated with the type of AE source through different AE indices [218], [219].

Moreover, the possibility to detect AE phenomena under operating conditions makes AE inspection one of the key methods of SHM. The basic working principle of this technique is the detection of elastic waves due to an AE event, such as cracking, delaminations, cleavage, and fretting in the material [218]. Among the very few AE approaches for the assessment and classification of active cracks in concrete structures, standards and recommendations issued by The Federation of Construction Materials Industries, Japan and the Japanese Society for Non-Destructive Inspection are generally accepted. From this point of view, a classical practice to monitor structures is performed by measuring AE parameters, or signal based AE technique. Recent studies on reinforced concrete demonstrated that specific AE features, such as rise time (or rise angle), peak amplitude, duration and counts are well correlated with the cumulative damage [220] and the cracking mechanisms [218]. A typical AE signal and its most important AE parameters are shown in Figure 3.56.

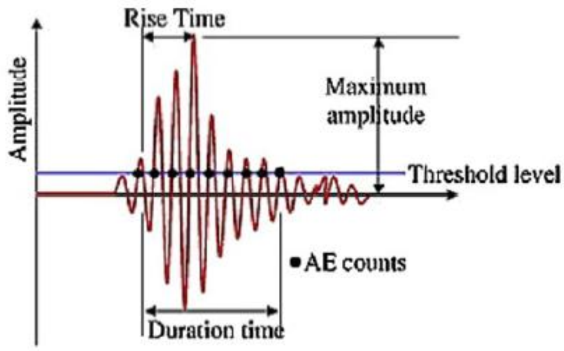

Figure 3.56. Acoustic emission parameters extraction [221].

A commonly used approach in concrete structures to evaluate the crack formation and propagation through AE is the loading test [222], [223], an approach which is here adopted on the previously damaged beam. The AE analysis was performed to characterize SHM–Lab AE prototype, taking an AE commercial system as reference.

The possibility to detect AE events using low-cost, low-power and stamp-size sensor nodes is crucial in those scenarios where remote and long-term monitoring of existing structures are primary issues. In preserving such convenient features, but achieving high performances, the design of the sensor node is highly application dependent. The performance evaluation starting from acquired data will be the reference point for further development processes of such an evolving circuitry. For this reason, the tested prototype needs to be intended as an intermediate step of the design process, which will be perfectly tuned on concrete AE analysis for future studies.

Additionally, preliminary characterization and classification of damages already existing inside the DB were performed in terms of fracture direction during the bending.

The rate of AE activity is often used as the primary criteria because it is highly correlated to the high rate of crack propagation indexes so the absence of AE activity implies a lack of serious cracks in the structure [224]. As a consequence, in the context of beam bending tests, the total number of AE hits recorded in the time domain is a fundamental parameter. Another important feature to be considered is the peak amplitude, which is normally correlated with the intensity of the crack propagation event. As it is provided in RILEM, peak amplitude was successfully used for the characterization of the fracture mode [218]. Conversely, since this phenomenon in concrete structures typically depends on the shape of the initial part of the waveform, the so-called RA value is extremely important. This parameter characterizes the type of cracks in the unit of ms/V and is calculated from rising time divided by maximum amplitude. Furthermore, as reported in [225], the combination of RA values and average frequency of individual hits allows for providing a classification of occurred cracks. Thereby, in this study, the trends of peak amplitude, cumulative counting of hits and RA parameters provided by SHM–Lab AE prototype and Vallen AMSY-5 are presented.

For testing the SHM–Lab AE prototype on concrete, one sensor node equipped with three different channels was attached to one lateral surface of the beam. Similarly, two VS-150RIC Vallen sensors with 34 dB integrated pre-amplifier were fixed on the upper surface of the beam, as shown in Figure 3.57. The loading test was performed following different criteria and phases. During the first step, AE signals were acquired by the Vallen AMSY-5 during preliminary analysis. Starting from 10 kN, six load cycles were carried out with a maximum increasing load of 10 kN in each cycle. After reaching a progressive load of 60 kN, also SHM–Lab AE sensor node was activated. One hundred further cycles were performed at 60 kN by setting the automatic loading machine. Finally, the last four cycles were executed stably at 70 kN. Both AMSY-5 and the SHM–Lab system were set taking into account the specificity of this experimental setup. The AE emission parameters were acquired by AMSY-5 at 10 MHz, while the acquisition of the entire transient waves was performed at 5 MHz: to maximize the total amount of information, and high sample rate is required to further extract AE parameters, whereas a lower sampling rate was preferred during the acquisition of the entire waves thus minimizing the memory occupation. After a preliminary measurement campaign, the threshold value of the trigger was set at 32 dB. The sensors were fixed to the beam with ultrasound coupling gel and adhesive tape. Also, the entire SHM–Lab AE system was configured to provide the best response in this application context.

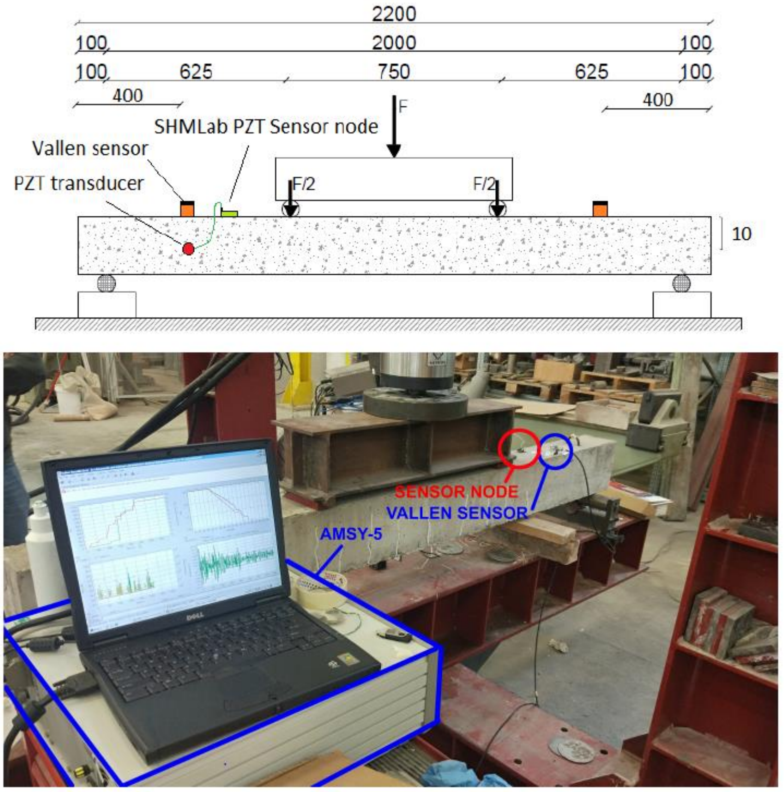

Figure 3.57. Acoustic Emission setup.

Consequently, since the most important frequency content of AE signals in concrete is typically under 300 kHz, waveforms were acquired at a sampling frequency of 500 kHz. The embedded conditioning PGAs were set at 23, which is the maximum gain attainable by the amplifier. Once the PZT signal exceeded the threshold level, all of the three channels simultaneously started the acquisition providing time windows of 10 ms. A total amount of 5000 samples were acquired at each crossing threshold. After every acquisition, data were transferred to a laptop, with a transfer time of about five seconds. During this blank time, the sensor node was not able to detect any AE signals. It is worth underlining that, being quite different either the sampling frequency, the frequency response of the transducer, and the transmission time, a direct comparison between the Vallen system and the SHM–Lab instrumentation was not possible. Nevertheless, a qualitative analysis of the behaviour of the SHM–Lab sensor node was performed, taking into account Vallen's estimated parameters as reference values. Figure 3.57 outlines the entire AE experimental setup.

During the preliminary test comprising six successive loading and unloading cycles, AMSY-5 was used to monitor the AE activity, study the feasibility of the experiment and characterize the AE phenomena inside the beam. From a typical curve given in Figure 3.58, in which the first 2000 s of loading are shown in comparison with the diagram of the cumulative hits, it can be seen that each cycle is followed by a significant increase in AE activity. With a slight change in the distribution of peak amplitude values, which depend on the loading level, the number of cumulative hits replies with explosive growth in AE events, especially in the rising and falling phase from 0 to 20 kN and vice versa.

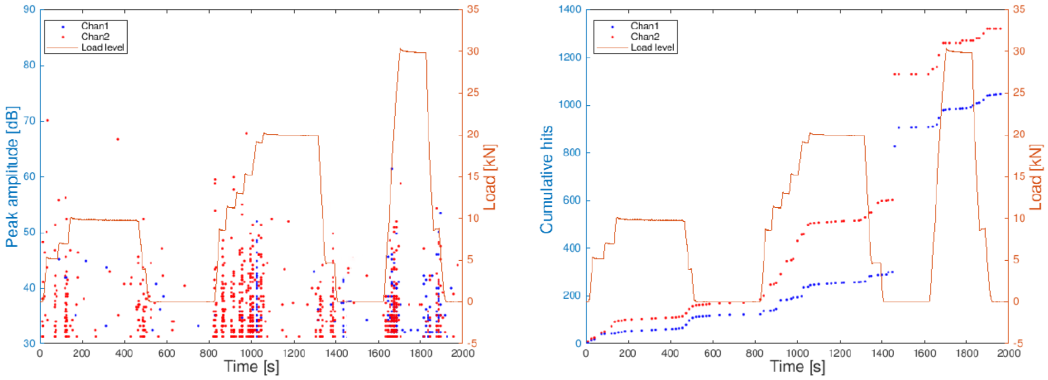

Figure 3.58. The behaviour of the AE peak amplitude and cumulative count, recorded by the AMSY-5, in comparison with the level of load in the time domain.

In the final stage, after performing a series of one hundred automatic cycles, a manual cycle up to 70 kN was executed. During this phase, AE signals were concurrently acquired by both the SHM–Lab AE sensor node and the AMSY-5 from Vallen.

Figure 3.59 displays the cumulative hits diagrams of the AE systems with the load. Regarding the graph on the left, which is referred to as the automatic cycles, the number of hits radically increases. It can be seen how meaningful information about AE activity is efficiently provided by both the AE instrumentation. Besides, the trends reported in the figure on the right, a great deal of agreement occurs between the increase in the AE activity recorded exhibited by SHM–Lab sensor and that displayed by Vallen’s curves, even if a slightly different sloping rate can be noticed. Other useful information to characterize SHM–Lab sensor node is provided in the diagrams of Figure 3.60. The normalized amplitude of hits acquired by the sensor node is plotted in the time domain, superimposed on the current load. The perfect fitting between the phases of loading and the AE activity provides the reliability and consistency of the SHM–Lab system. Therefore, the sensibility in terms of the peak amplitude of the two systems is highly comparable. The SHM–Lab sensor provides signals from 61.6 dB to 111.6 dB with an average value of 87.04 dB. The AMSY-5, instead, during the same phase of the experiment, provides signals from 32.04 dB to 104.8 dB with an average of 71.16 dB.

Finally, because over the observed period the number of recorded events significantly differs between two AE systems, as described in the previous paragraph, normalized histograms distribution of different ranges of the RA indices were given in Figure 3.61.

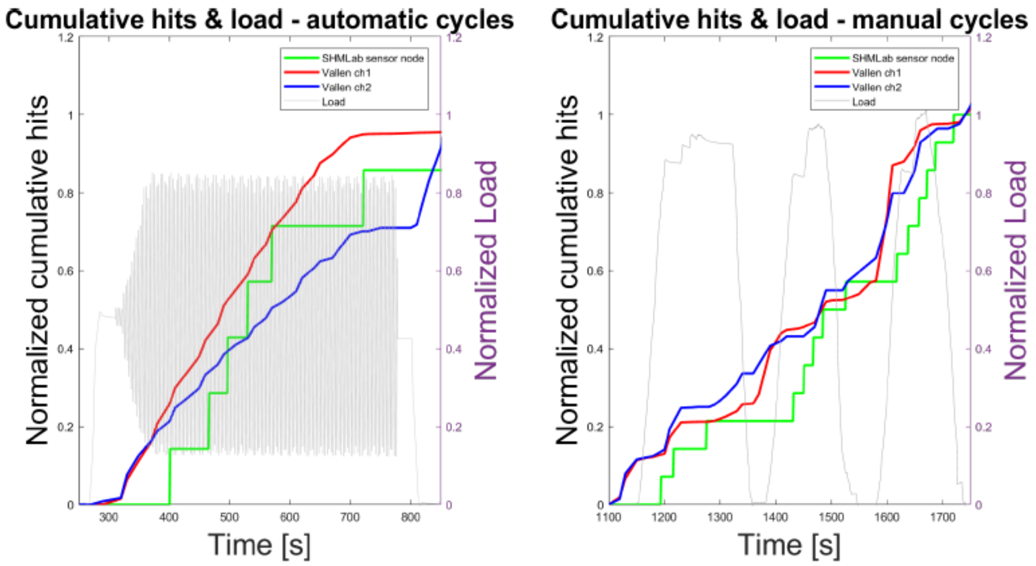

Figure 3.59. Comparison between the normalized cumulative hits diagrams of both the SHM–Lab sensor node and Vallen during the automatic cycling load phase (left) and the last three loading cycles (right).

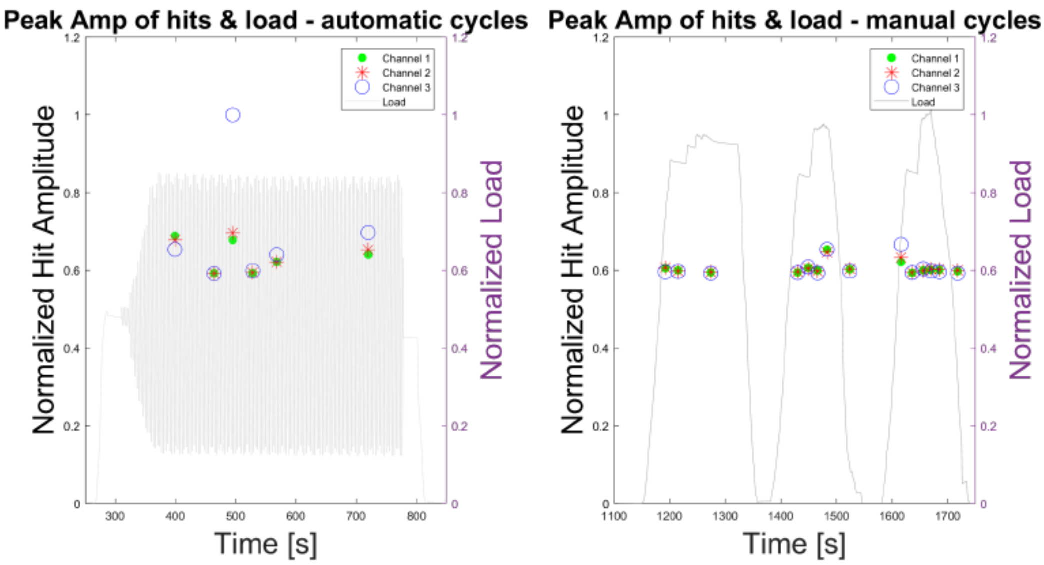

Figure 3.60. Comparison between the normalized amplitude hits diagrams of the SHM–Lab sensor node during the automatic cycling load phase (left) and the last three loading cycles (right).

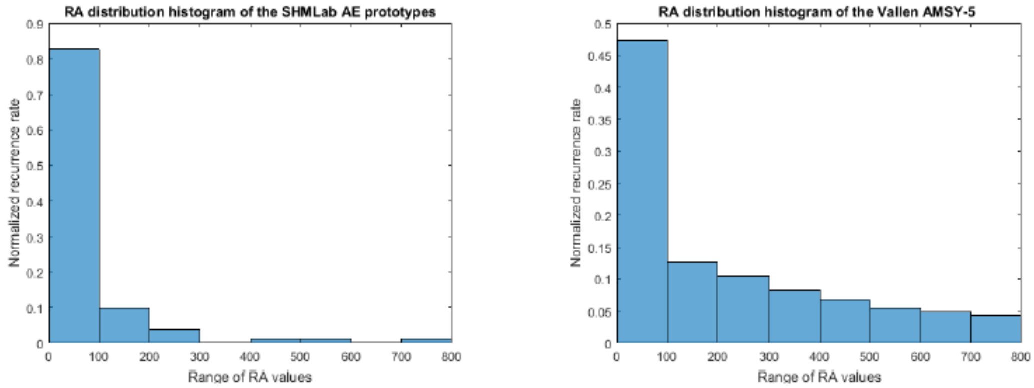

Figure 3.61. Comparative analysis of the distribution histogram of the RA parameter.

On a comparative scale, it can be argued that obtained data greatly correlate with each other. In both cases, the RA index, which is used as a classifier for the types of cracks, shares a similar distribution. The larger contribution to RA values is approximately located in the range from 0 to 300 V/s, with a coherent decreasing exponential trend. These results show that the SHM–Lab AE system is not only able to detect the acoustic emission source inside the concrete beam but also to characterize, within certain degrees of approximation, the AE activity to provide to the user meaningful information, such as the severity of cracks and their correspondent classification, after a set of meaningful parameters has been extracted.

3.3.2 Investigation of a concrete bridge deck

The bridge model was set out to study the effect of a diffused crack pattern on the fundamental natural frequency, estimating the bridge residual bearing capacity by looking at the frequency decay due to the presence of damage. The laboratory campaign consisted of both static 4 Point Bending Tests (4PBT) and dynamic tests for the material property characterization, and then a bridge numeric counterpart is used for the experimental data validation concerning the undamaged condition only.

Static load test: 4 Point Bending Test (4PBT)

The loading system illustrated in Section 3.1.5 was adopted for performing a static load test of the concrete deck (Figure 3.62). The load acted directly on each of the four main girders thanks to the eight loading points illustrated in Figure 3.63. The model bridge was firstly loaded up to 100 kN staying in the linear-elastic stress range of the materials and avoiding any crack occurrence. The forces exerted at each loading point were figured out by solving the equilibrium problem. However, the loading setup was not fully symmetric compared to the bridge longitudinal axis, so the forces applied at these points resulted in different fractions of the total load. Forces equal to 14%, 21%, 29% and 36% of the total load *P* acted on the four beams instrumented with the Linear Variable Differential Transducers (LVDTs) 1, 2, 3 and 4, respectively. A total of six vertical displacements were recorded during the experimental campaign. The positions of the LVDTs are marked in Figure 3.64 and Figure 3.65: while four transducers measured the vertical deflection at the mid-span of the main beams, the remaining two recorded the vertical displacements near the supports due to the shortening of the rubber bearings.

Figure 3.62. Static load test setup: on the left is shown the static loading system.

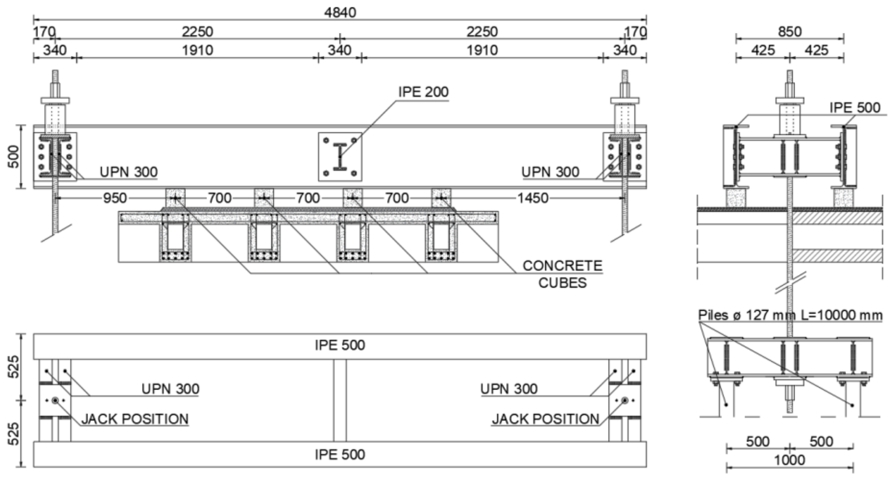

Figure 3.63. Experimental setup for the loading system.

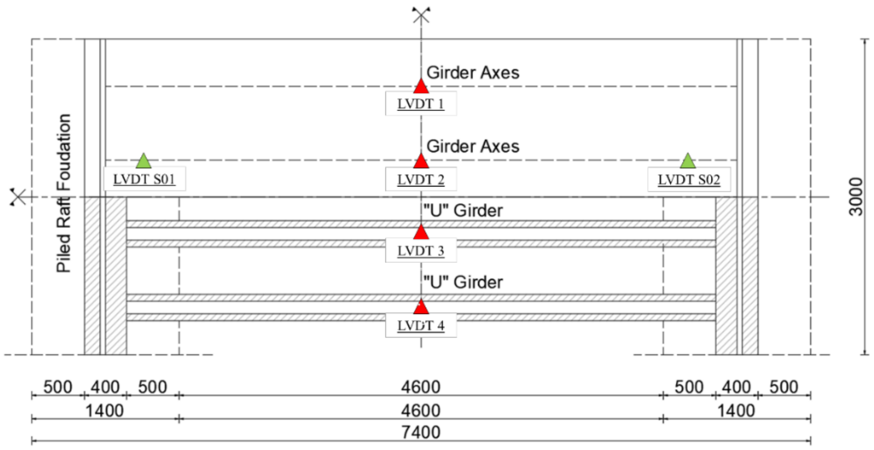

Figure 3.64. Plan view of the concrete bridge and the position of the LVDTs adopted for the static load test (measurement range: red marks 0-100 mm, green marks 0-20 mm).

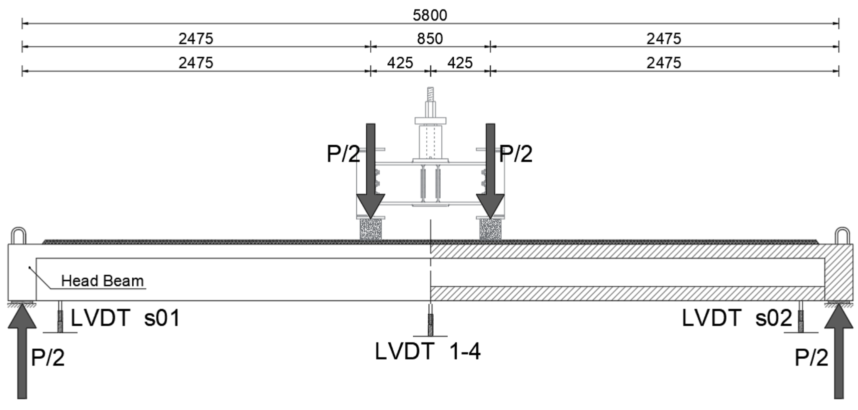

Figure 3.65. Setup for the static load test.

The measurement range of the LVDTs transducers (1 to 4) placed at the beam mid-span was set to 100 mm, while the two LVDTs “s01” and “s02” were placed near the supports, had a range of 20 mm. In conclusion, the bridge elastic behaviour is described by six load-displacement curves of six reference points.

Solving the equilibrium of the concrete cross-section and following the guidelines introduced in Section 3.1.1, the initial bending rigidity of the bridge and the axial stiffness of the rubber pads were analytically computed and then compared with the values inferred from the two experimental curves. The analytical bridge rigidity EJ_0 matched exactly with $2.55 \cdot 10^5$ kNm^2, the one reckoned from the mid-span load-displacement curve. Concerning the stiffness of the rubber pad, the comparison with the support load-displacement curves proved a biased estimation of the neoprene axial stiffness: the backhand stiffness calculation suggested a proper value for the axial stiffness equal to $2.8 \cdot 10^5$ kN/m. This means that the lateral confinement exerted by the concrete surfaces on a single pad was higher than the one considered by the Standards, and highlights the prerequisite of executing load tests for assessing the correct support stiffness, to be included in the dynamic calculations.

Dynamic Identification of the bridge model

The sensors layout employed in this paper involves the eight SENSR CX-1 tri-axial MEMS accelerometers [180] of Figure 3.66 for the identification of the modal features associated with the first vibrating modes. Although the choice of using more sensors, or the one concerning the fusion of data provided by different setups (multi-setup technique), might lead to a more clear representation of the mode shapes due to a better spatial resolution, the selected minimal setup was able to detect and clearly distinguish the first six mode shapes of interest. Each sensor acquired 2000 samples per second for 8 minutes, a time-lapse greater than 2000 times the fundamental period of the bridge [226].

A set of random hammer hits was used as an excitation source for the bridge. By hitting the hammer at the bridge intrados in several positions a large number of dynamic modes was excited. The first six frequencies were estimated through the time-series data processing both in time and frequency domains, by using the Covariance Stochastic Subspace Identification method (SSI-COV) [46], [182], [183] and the Frequency Domain Decomposition technique (FDD) [27], [181], respectively. Both SSI and FDD algorithms are available in a MatLab Environment [184], [185] and the needed input parameters were set accordingly to what was suggested by *Magalhlaes et Al.* [183], [186].

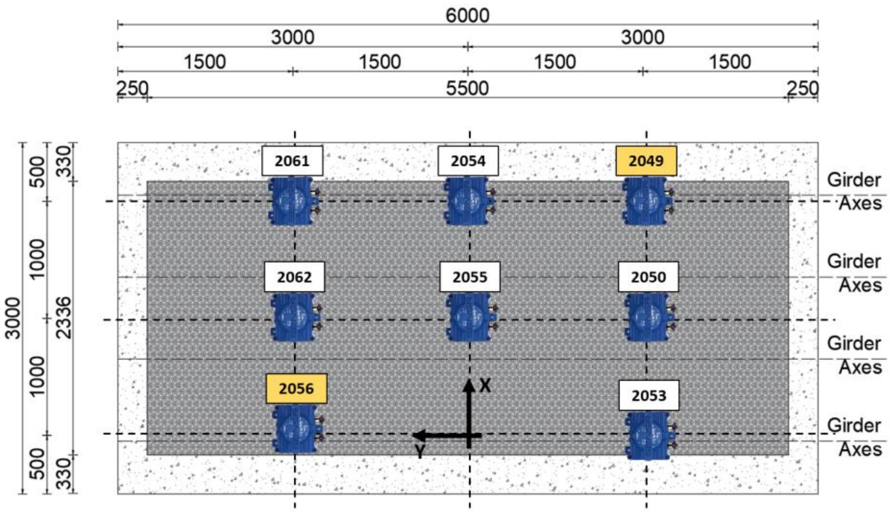

Figure 3.66. The setup used for the dynamic test.

Concerning the case under investigation, by setting the model order and the time lag equal to 100 and 1 second, the results in terms of stable poles validated the frequencies detected by the FDD algorithm. All the recorded time series were processed either considering each hammer hit separately, or processing the entire length of the recorded signal. The use of the Hanning window of 4096 samples and a 50% overlap between two subsequent intervals reduced the leakage effect in the time series processing. Because no significant differences in terms of estimated frequencies, damping ratios, and modal shapes were observed, thus all of these quantities were averaged.

Figure 3.67 collects the result of the two procedures: the solid line representing the first singular value computed through the Singular Value Decomposition (SVD) of the spectral matrix decomposition, leading to the estimates of the frequencies associated with the bridge vibration modes of interest. Instead, the red stars represent the stable poles given by the SSI procedure, and their alignment is normally associated with a natural frequency of the system. Lastly, the dashed line refers to the coherence computed among the time series giving information about the reliability of the frequency detected once its value becomes higher than 0.80. Moreover, the information contained in the singular vectors at the position of each local maxima provided the coordinates of the modal shapes related to each frequency (Figure 3.68).

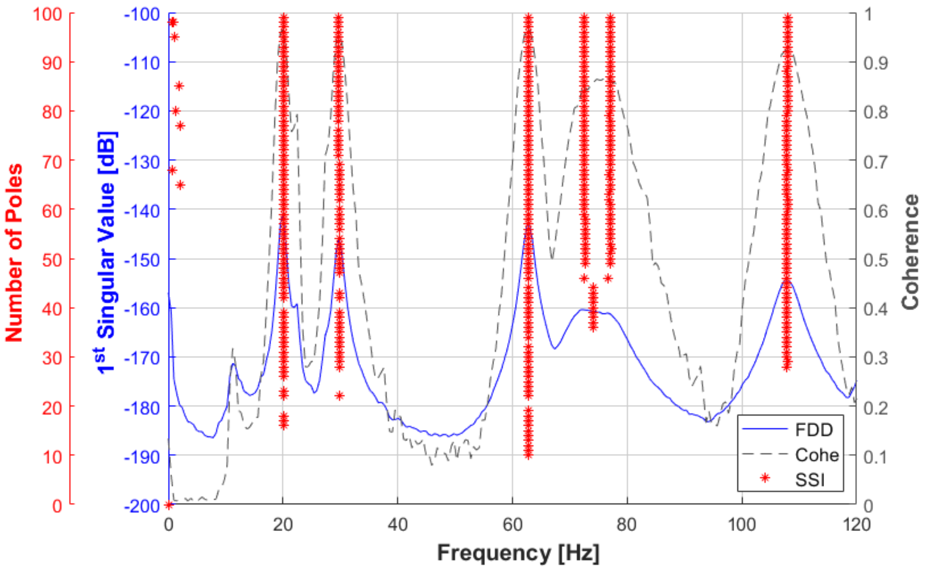

Figure 3.67. First singular value of the spectral matrix (solid line), Coherence (dashed line) and stable poles given by the SSI procedure.

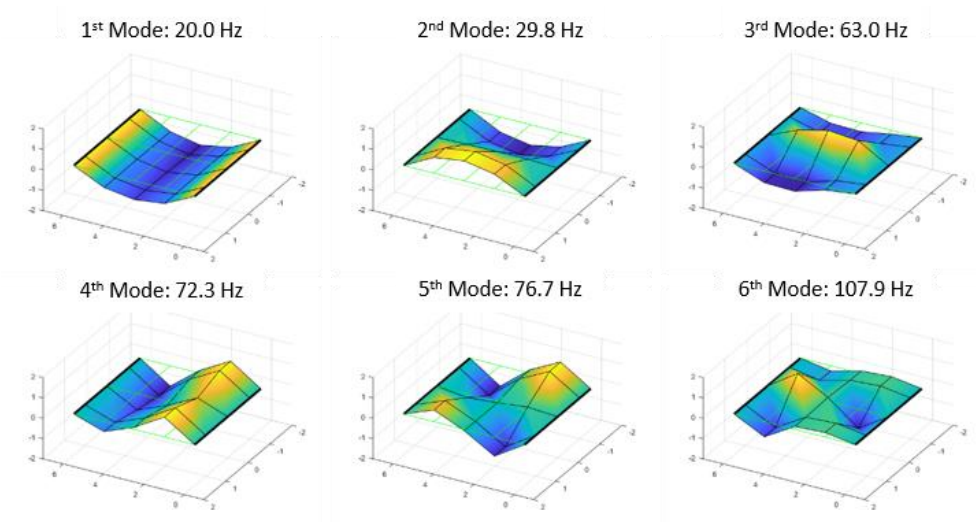

Figure 3.68. Lowest six mode shapes identified through the operational modal analysis.

Numeric interpretation of the experimental tests

The numerical representation of the model bridge is then built with the Italian version of the commercial FE software STRAND (Figure 3.69) for supporting the mechanical parameters obtained through the tests. Three-dimensional solid 8-node brick elements were selected to model the geometry of the concrete deck, then the element properties were assigned combining the test outcomes and the reference properties presented in Section3.1.1.

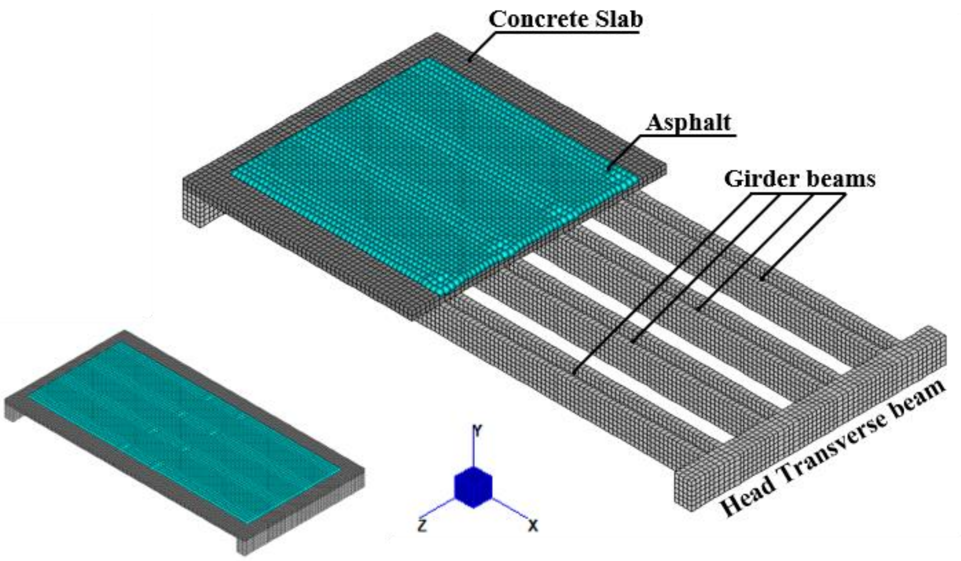

Figure 3.69. FE numerical model of the concrete deck.

Regarding the loads, while the asphalt layer laying above the concrete slab was defined as a distributed surface mass, the force acting on each concrete cube was spread as equivalent pressure in 150x150 mm^2 square area on the bridge slab. Lastly, the rubber pads placed below each main beam were modelled by using equivalent elastic springs.

Then, linear static and modal analyses were carried out simulating the load test and extracting the dynamic features, respectively.

Concerning the static load test, Figure 3.70 and Figure 3.71 endorsed the perfect fit among the load-displacement curves at the supports and the bridge mid-span, respectively, with their numerical counterparts.

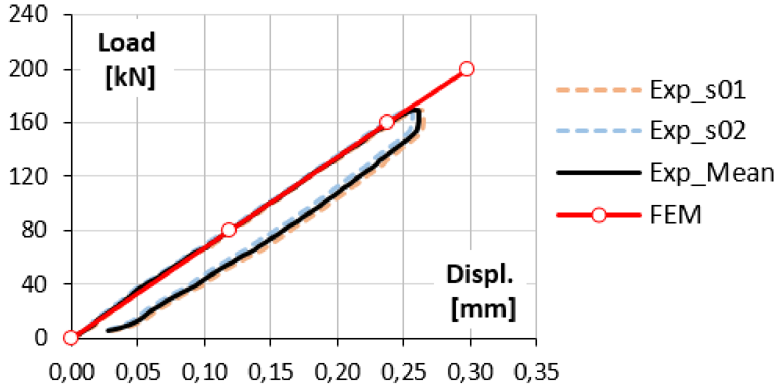

Figure 3.70. Load-Displacement curves measured at the supports "Exp_s" compared with the results of a set of linear static analyses performed on FE model "FEM".

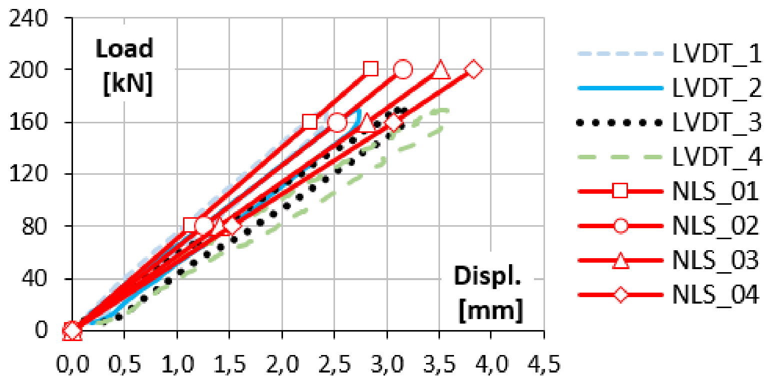

Figure 3.71. Load-Displacement curves measured at the midspan of the four main beams “LVDT_” compared with the results of a set of linear static analyses performed on FE model “NLS_”.

A good match was even observed for the dynamic behaviour: Table 3.15 collects the values of the fundamental frequencies, either estimated through the dynamic investigation or obtained carrying out the modal analysis on the FE model. The corresponding modal shapes are illustrated in Figure 3.72. The differences between the presented data are always lower than 10% for all the modes and fit exactly for the first frequency which was used to assess the initial and the residual carrying capacity of the bridge deck.

Table 3.15. List of identified modal shapes, modal frequencies and damping ratio.

Mode	Modal Type	FDD [Hz]	SSI [Hz]	Damping [%]	FEM [Hz]	Error [-]
1	Bending	20.0	20.1	3.1%	20.0	0.0 %
2	Torsional	29.8	29.7	2.7%	31.9	-7.1 %
3	Plate-like	63.0	62.7	1.4%	62.1	1.4 %
4	Bending	72.3	72.6	5.9%	69.9	3.3 %
5	Torsional	76.7	77.1	4.9%	76.7	0.0 %
6	Plate-like	107.9	107.9	2.1%	111.1	-3.0 %

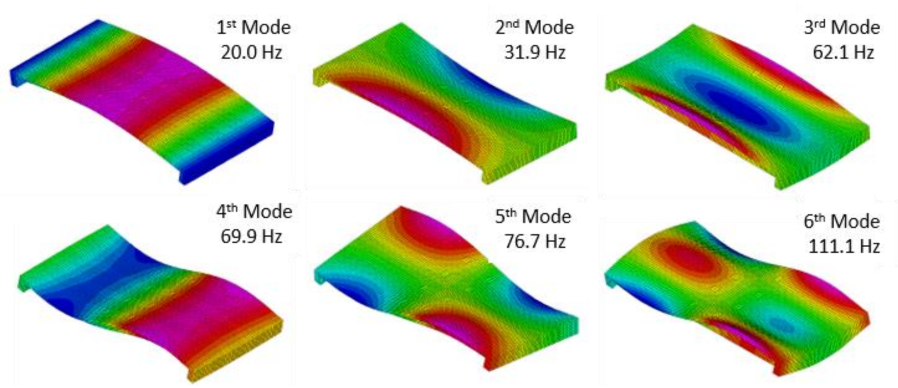

Figure 3.72. Lowest six mode shapes of the FE model.

The accuracy of the FE model in terms of comparison among the mode shapes resulting from the application of FDD and their numerical counterpart can be validated by the computation of the well-known Modal Assurance Criterion (MAC) [187]. The Modal Assurance Criterion is applied by convolving the identified modal shapes with the numerical ones (Figure 3.68). Even the consistency of the FE model was proved, with all the values in the MAC matrix main diagonal higher than 85%. Therefore, the obtained FE model can describe accurately either the static or the dynamic behaviour of the laboratory bridge by itself.

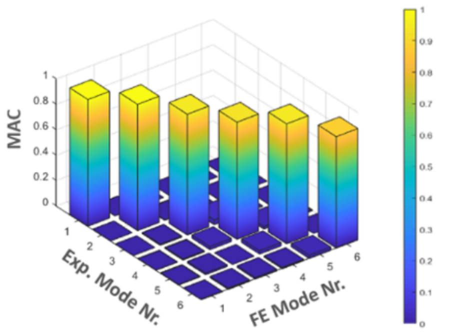

Mode		FE Modes					
		1	2	3	4	5	6
Experimental Modes	1	0,998	0,001	0,000	0,000	0,000	0,000
	2	0,001	0,995	0,003	0,000	0,001	0,000
	3	0,000	0,009	0,951	0,037	0,002	0,001
	4	0,002	0,007	0,025	0,923	0,021	0,005
	5	0,004	0,014	0,000	0,026	0,945	0,000
	6	0,001	0,010	0,014	0,010	0,026	0,878

Figure 3.73. Bar-plots of the MAC and its value obtained by convolving the experimental modal shapes with those provided by the FE model.

Description of progressive damage states

Due to the complex handling of the test apparatus, only three damage conditions were considered in the study. The load was increased steadily, naming "D0" the undamaged state, the initial limit state of concrete cracking (D1) was achieved through the first load step, then an intermediate step up to a fully stabilised crack pattern (D2), and finally reaching the yielding of the steel rebars (D3) with a deck residual deflection of more than 100 mm. Although the value of the total bending moments acting on the bridge can be easily computed by solving the equilibrium problem, the value associated with each damage step was inferred from the experimental load-displacement curve of Figure 3.74, leading to 430 kNm, 910 kNm and 1300 kNm, for the states D1, D2, and D3, respectively. The final condition of the concrete bridge showed the residual deformation and the set of cracks illustrated in Figure 3.75.

Each damaged configuration was then investigated by performing dynamic tests accordingly to the previous identification phase by using some random hammer hits as a source of excitation. The three levels of damage severity reached during the static load test produced frequency losses equal to 5%, 18.1% and 21.6% compared with the one associated with the undamaged state.

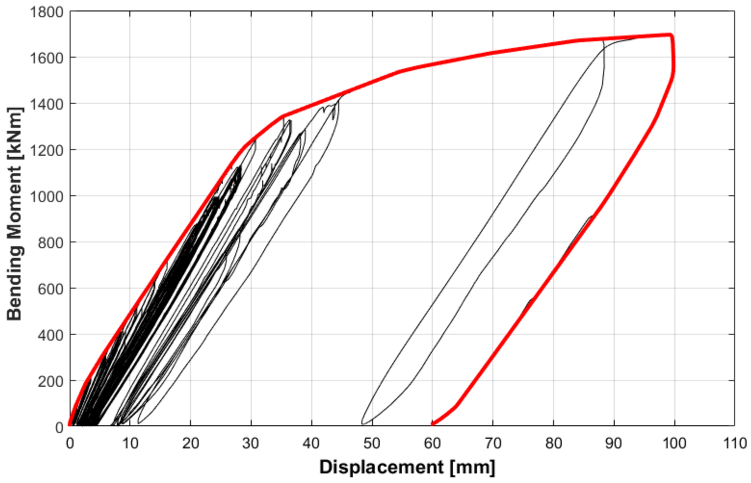

Figure 3.74. Bending moment – Mid-span displacement curve achieved during the load test.

Figure 3.75. Residual deformation experienced at the end of the load test (a) and the observed crack pattern (b).

It is well known that the natural frequencies of a structure are strictly dependent on its stiffness when mass and temperature changes can be neglected. For the examined case, because all the dynamic tests were performed at the same temperature, roughly equal to 30°C, the frequency shifts are the direct consequence of a stiffness loss caused by the occurrence of damage. The ongoing continued monitoring of the bridge will quantify the frequency trends over the daily temperature variations, essentially due to the changes in concrete and asphalt stiffnesses.

In this study, only the two accelerometers named 2056 and 2049 (Figure 3.66) were used for the frequency identification at the end of each damage step, even if only one sensor can be used for detecting frequency changes. Because the influence of the damage on higher modes is not of concern for this paper, those modes were neglected.

However, dealing with more complex real cases, a higher number of sensors or the roving sensor technique [227] can help in achieving a detailed stiffness change distribution along with the bridge structure.

Assessment of the residual bending capacity

The typical crack pattern associated with a distributed load acting on a bridge was replicated experimentally by performing a load test on the deck model in the non-linear range beyond the onset of the concrete cracking.

The stiffness and the frequency changes detected in the experiment allow checking the theoretical analysis previously presented [84]. The predicting formula indicated by Eq.(3.21) mainly depends on the factor η quantifying the bending rigidity loss due to the damage $\left(\frac{EJ_0}{EJ_T} - 1\right)$ and the ratio α between the cracking moment M_{cr} and the maximum bending moment M_{max} achieved during the test. Moreover, the value of α is strictly related both to the damaged length of the beam and the amplification factor λ as the ratio between M_{max} and the yielding bending moment M_y.

$$f_D = f_0 \cdot k_D = f_0 \cdot \sqrt{\frac{1}{1+6\eta \cdot \frac{(1-\alpha)^2(1+\alpha)}{12-4\alpha}}} \tag{3.21}$$

Although in a simply-supported beam, the value of the average stiffness can be easily computed from the fundamental frequency, in general disregarding the so-called “crack breathing effect” due to the crack closure during the dynamic vibration, the analysis can lead to large errors in estimating the stiffness change.

All the data of the three increasing damage phases were processed, by recording the deviations of the lowest frequency for each step. The resulting frequency decay over the ratio λ is illustrated in Figure 3.76 and underlines the three damage states by red stars. The first step of damage (D1) produced a deviation of 5% of the reference value, while the following drops fit with the formula of breathing cracks proposed in Section 3.3.1 and the foreseeing errors remain lower than 5% for each damage condition.

Starting from the original bending rigidity EJ_0, the rigidities associated with the three increasing damage states resulted in a stiffness decrease, based on the breathing crack theory, of 9%, 33% and 38% for the damage conditions D1, D2 and D3, respectively.

This is consistently far from the frequency decay calculation based on the stiffness reduction identified by the red square in Figure 3.76 since stabilised cracking let the stiffness drop by 51% with a frequency shift of 28%, while the yielding state usually reduces the stiffness to 20-30% with a supposed frequency drop of more than 60%.

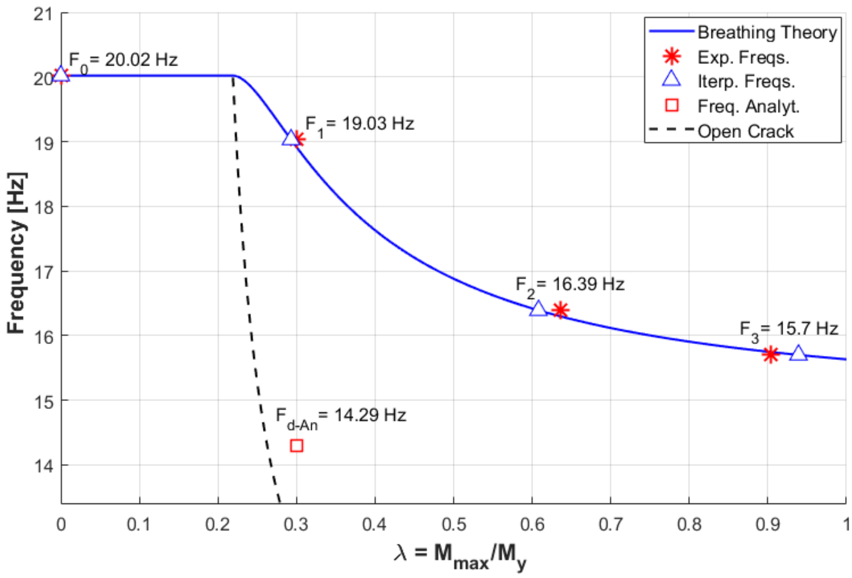

Figure 3.76. Frequency decay due to the presence of damage.

The frequency calculations which involve analytical values of bending stiffness do not consider the effect of crack closures on the modal behaviour of the bridge. This is the reason why the red square representing the damaged frequency computed with the cracked section rigidity is more similar to the black dashed line describing the condition in which the cracks remain open.

3.3.3 Contribution in the field of diffused damage identification

Moving to concrete structures, the consequences on the fundamental frequency of a diffused crack pattern is addressed by dealing with either single concrete beams of Section 3.3.1 or the concrete bridge deck of Section 3.3.2.

Concerning one of the concrete beams, the early assessment of its dynamic behaviour is carried out by using two CX1 accelerometers. Moreover, during the further step, the beam was subjected to a 4PBT producing the typical crack pattern of a damaged simply supported RC beam. The occurrence of the cracks was observed through the Wallen system dealing with the acoustic emission. The commercial devices used within those two phases were combined with the hybrid miniaturized sensor network illustrated in Section 3.3 comparing their performances. The outcomes evaluation of the performance of the tested SHM–Lab system outperformed similar but more expensive and invasive instrumentation, standing out for its compactness and versatility. Despite being in presence of rather different hardware and software features, the extracted structural information proved to be extremely coherent and consistent with its commercial counterparts. In detail, experimental results related to the inspection of the reinforced concrete beams demonstrated the capability to accurately address both the dynamic vibrational behaviour and the acoustic emission activity of concrete-based structures. As a consequence, SHM–Lab smart nodes appear to be extremely promising in those scenarios where size, weight, power and costs are crucial.

Then the analysis of the data collected by the CX1s has been processed for a mechanical explanation of the damage-induced frequency decay. The evaluation of the main frequencies for simply supported RC beams with a cracked region is a challenging problem. Usually, non-linear formulations based on the reduced rigidity of the cracked sections underestimate the frequency values due to the open–closure cycles of the cracks usually termed as "breathing cracks". On the contrary, other factors such as freeze-thaw degradation or fatigue cycles can reduce consistently the natural frequency of cracked beams due to the weakening of the concrete surrounding the tensile reinforcement. The static equivalence principle of the kinetic energy helps in building up a model in which all the influences are factored in the equivalent displacement evaluation, leading to a general analytical formulation of the phenomenon. Since energy is a scalar quantity, a very simple hypothesis can be introduced for the evaluation of the alternate opening and closure of the cracks, based on the energy averaging of the two different phases. It is to cite that this hypothesis complies with the displacement averaging of the two configurations. The formula proposed in Section 3.3.1 describes the behaviour observed experimentally and explains the contribution of the crack cyclic closure to the final result. Moreover, the formula is validated with a very large database of experimental tests present in the literature dealing with simply supported RC damaged beams. Although the configurations show a wide range of the main parameters, the detected frequencies point out a well-defined trend as a function of the damage level. The comparison of the proposed formula with the statistical best fit of the population, and with a numerical solution based on the distinct element method, highlights the effectiveness of the adopted hypotheses. Then, the use of FEM models with non-linear elements reproducing the crack closure allowed explaining the observed experimental behaviour in quantitative terms.

The detection of dangerous conditions in real structures requires a good sensitivity to the monitored parameters. It is evident from the discussion that frequency drops can appear only at the onset of cracking or yielding. However, when the structure is close to collapse it is extremely risky to wait for a further frequency drop. The onset of a stable 10%-15% frequency reduction (which probably is even steadily slightly increasing due to progressive bond deterioration), is the key response to look for. At this event, an immediate inspection and maintenance activity must be planned and carried out. The same formula, extending the problem of breathing cracks to a simply supported concrete bridge deck, may be used even for assessing its residual bending capacity through frequency data.

Section 3.3.2 presents the assessment of the dynamic behaviour of the concrete bridge deck where the first six vibration modes were detected in the range of up to 100 Hz. Then, the two sets of modal coordinates corresponding to the numerical and identified mode shapes have been convolved by computing the MAC matrix and finding a good match among the two datasets. The 4PBT performed on the bridge produces a diffused crack pattern along the main girders inducing significant shifts in the values of the lowest frequencies, especially for the first one strictly associated with the stiffness of the deck. Concerning the observed frequency decay, the "breathing cracks" theory and the analytical formulation discussed in Section 3.3 can predict the actual level of load exerted on the bridge based on the experimental frequencies, assessing the remaining capacity to respect the load associated with the yielding moment.

4 Assessment of the dynamic behaviour of existing bridges

4.1 Annibaldi Bridge: Dynamic Identification

On the anniversary of the Jubilee year in 2000, Rome was expected to attract many pilgrims and tourists. A public building competition was held for creating three temporary walkways along with strategic points of the pilgrimage route to facilitate movement limited by the Capital's regular traffic. Because of the ongoing restriction of the Archeological Superintendence, only one pedestrian bridge was built on *"Via degli Annibaldi"* (Figure 4.1). This recreates the historical axis of *"Via della Polveriera"*, interrupted by *"Via degli Annibaldi"*, and ensures a safe crosswalk for all those wishing to reach the Colosseum Metro Station from "*Via della Polveriera"*. A distinctive feature of this place is that the two retaining walls on which the bridge rests differ in height of about 1 meter along their entire length.

Therefore, the bridge intrados needed to be constantly maintained at a height of 5 meters above the driveway, which involves a minimum radius of curvature of the deck plane. For this reason, the bridge reaches the retaining wall of *"Largo G. Agnesi"*, about 1.20 m lower than the arrival height. The altitude gap was solved by connecting the two heights with a stone staircase, equipped with a stairlift. Among more than 50 projects presented, the winner was Francesco Cellini. The walkway design was twofold: on the one hand, Cellini seeks the utmost structural and visual lightness to integrate into the complex urban skyline; on the other hand, he carefully selected the materials for the ground connection based on the materials and finishes of the surrounding urban fabric.

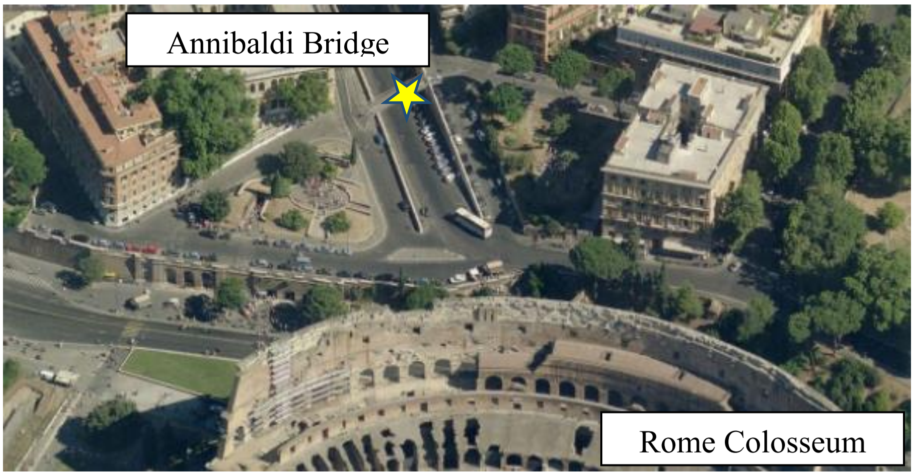

Figure 4.1 Overview of the location of the Annibaldi Bridge.

4.1.1 The geometry of the walkway

The bridge has a continuous beam structure, with a central supporting spine, partly included in the deck intrados, whereas its extrados was transformed into a continuous central bench. The solution reduces the thickness of the deck and minimizes the impact of the architectural body on the Colosseum (Figure 4.2). It is to note that, the pedestrian bridge is not straight because of the issue described in the previous section, thus a curvature radius of 123 m was provided in the bridge design. The walkway length is equal to 20 m and 4 m is its width. The path is divided according to the flows, accompanied along the route by the continuous central bench (accessible along its entire length as an element of rest, relaxation and viewing of the Roman historical panorama), and assisted by a servo-ladder for an easy crossing. While the bench has a roof in sandblasted stainless steel, the walking surface and the coating of the bench are made of lava stone, whereas wood planks cover the bench seat for improving the level of comfort. The access ramps and stairs are made of masonry and covered with materials that are uniform to those of the surrounding area.

The original drawings and the technical report were provided by the *"University La Sapienza"* of Rome during the *"12th Asia-Pacific-Euro_Summer_School"* [228], and then presented in Figure 4.3 and Figure 4.4. In particular, Figure 4.3 shows the piled foundation used for supporting the Annibaldi retaining walls and the layout of the bearing devices supporting the bridge: on the left, a mono-directional sliding device was placed allowing the longitudinal displacement, while on the right a multi-directional device was added to the fixed hinge provided granting the lateral motion. As is commonly used in the bridge design practice, some directions need to be left free to move to afford the problem of thermal deformations or other horizontal displacements caused by different nature (e.g. horizontal deformation induced by the settlements of the arch). For this reason and design purposes, its behaviour may be similar to the one associated with a simply supported beam, neglecting the arch effect.

Moreover, one parapet with a height equal to 1.0 m was designed to ensure the safety of the people crossing the walkway, avoiding any accidental falls. Each parapet pillar is placed at a distance of 2 m from each other, in continuity with the deck diaphragms, and then bolted to the floor using four bolts of ø12 mm. In what follows, the additional stiffness to the bending stiffness of the bridge deck provided by the parapet was considered negligible, thus even the parapet was not considered during the modelling phase.

Figure 4.2 Front views of the Annibaldi pedestrian bridge [229].

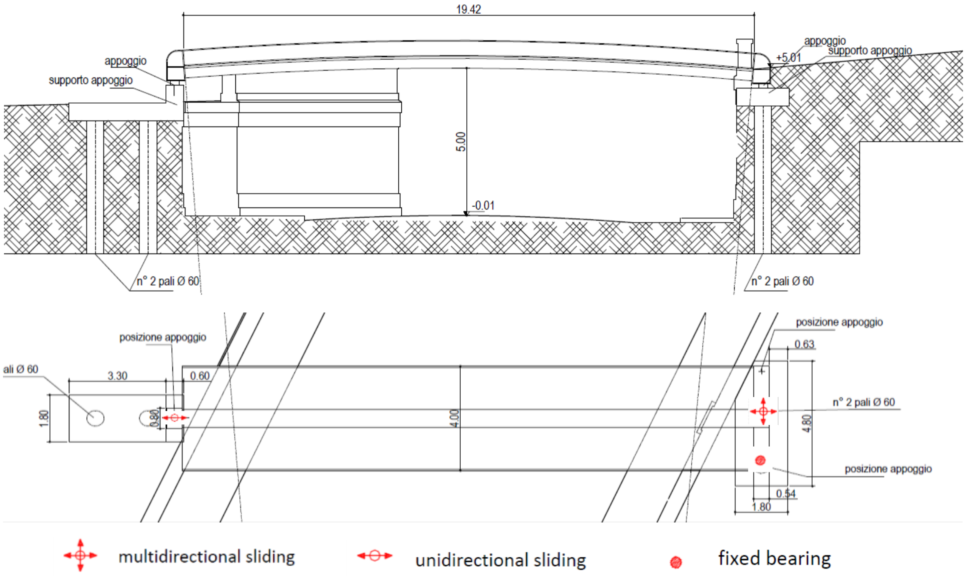

Figure 4.3 Lateral view, sagittal sections and overview of the Annibaldi Walkway, including the restraint conditions [228].

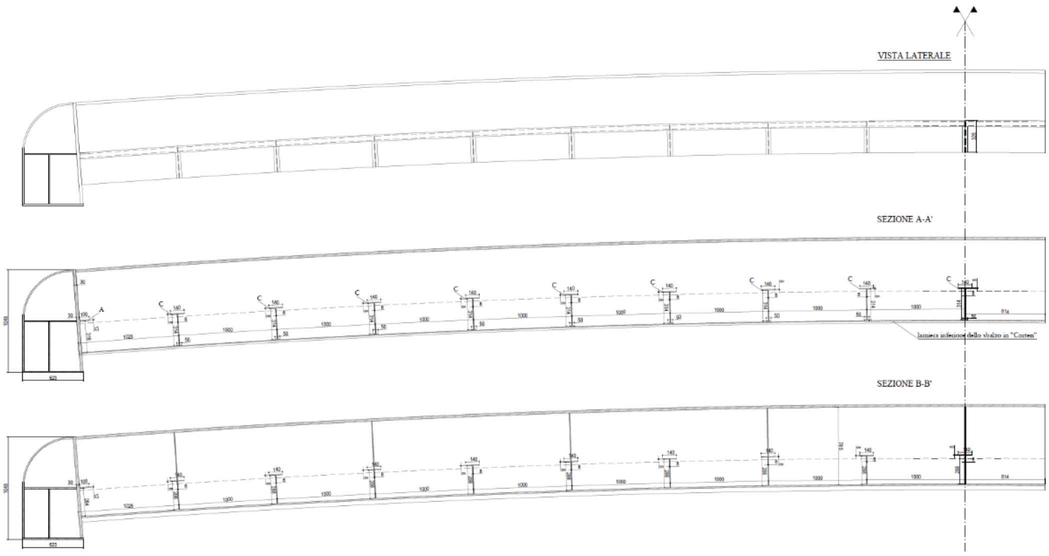

Figure 4.4 Lateral view and sagittal sections of the Annibaldi Walkway[228].

4.1.2 Cross-section details and Materials

According to the technical report [228], the mechanical properties of all the building materials used for the construction of the bridge are listed in Table 4.1, including their density. Regarding the cross-section of the bridge, several plates of different thicknesses were welded together for creating the structure, starting from the central core and then adding a diaphragm every 2 meters. The bridge cross-section was designed to be rigid in its plane, aiming for the values of 5.65e05 cm^4, 1.96e05 cm^4 and 3.8e05 cm^4 respectively for the inertia moment along the main direction, the one related to the secondary direction and the rotational inertia. Figure 4.5 illustrates the steel cross-section and the views concerning the structural components of the bridge.

Table 4.1 Mechanical properties of the material of the Annibaldi bridge [228].

Deck and Piers					
Material	Class	f_{yk} [MPa]	f_{tk} [MPa]	Young Modulus [MPa]	Density [kN/m^3]
Steel	Fe 510	355	510	210000	78

Abutments and Foundations					
Material	Class	f_k [MPa]	R_{ck} [MPa]	Young Modulus [MPa]	Density [kN/m^3]
Concrete	C25/30	25	30	30000	24
Steel	FeB 44 k	430	-	210000	1

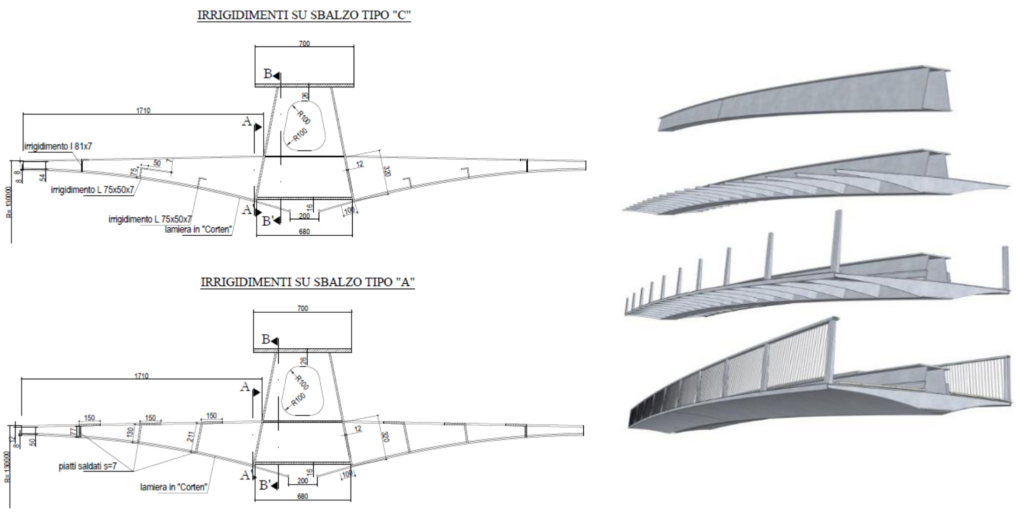

Figure 4.5 Cross-section (left) and the overview of structural and non-structural components of the bridge deck (right) [228].

4.1.3 Finite Element Model

Knowing the mechanical properties of the material and the inertia properties of the cross-section collected in the report the Finite Element Model of the Annibaldi bridge was created with the SAP2000 FE Software. The criteria followed for creating the numerical model are depicted in Figure 4.6. The numerical model is mainly a beam-based FE model: the core of the section consists of several beam elements with the box section of Figure 4.5 with the corresponding inertia moments and density; then, the taped "wings" of the cross-section are placed every 2 meters completing the geometry. Since the centres of gravity of the core and the wings are not aligned, several rigid links are inserted for placing the element in the correct position. Lastly, an equivalent diaphragm is inserted between two subsequent wings corresponding to the steel plates used in the existing bridge for creating a closed section. Each diaphragm is split into four parts for allocating the ribs running along the steel plates to increase their stiffness. The views of the numerical model are presented in Figure 4.7.

Concerning the boundary conditions, equivalent horizontal and vertical elastic springs take place of the bearing devices.

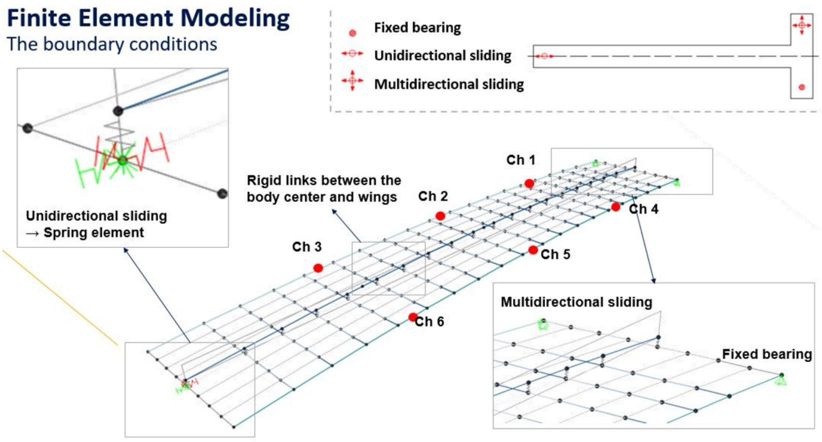

Figure 4.6 Criteria for modelling the Annibaldi bridge deck.

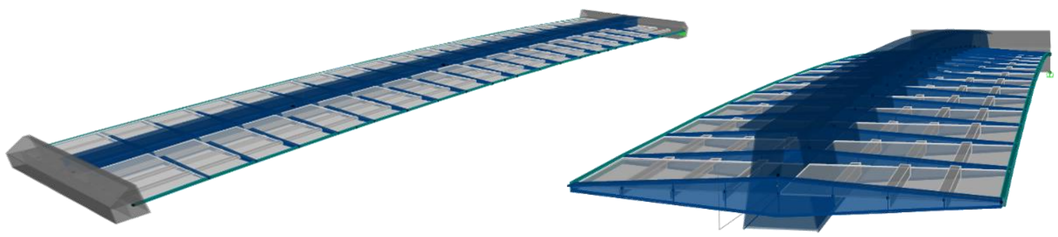

Figure 4.7 Views of the Finite Element Model

4.1.4 Experimental setup for the Operational Modal Analysis

The experimental investigation involved six mono-directional piezoelectric accelerometers arranged into three complementary setups (Figure 4.8). The advantage of using more than one setup overcomes any potential deficiency in the sensor availability even though the time needed for the experiment increases. Each accelerometer of the first and second setups was used for investigating only the vertical direction at the mid-span of the deck and at its quarter, detecting either bending or torsional modes. Since in the third setup the orientation of the three channels 1, 2, and 3 was rotated at 90°, even any horizontal acceleration may be collected.

It is to note that each setup shares the location of channels 4, 5, and 6 keeping them as reference for merging all the setups [230]. According to the minimum length of the recorded signals suggested by [226], 20 minutes of ambient vibration were collected by the six sensors at the same time, with a sampling frequency equal to 200 Hz.

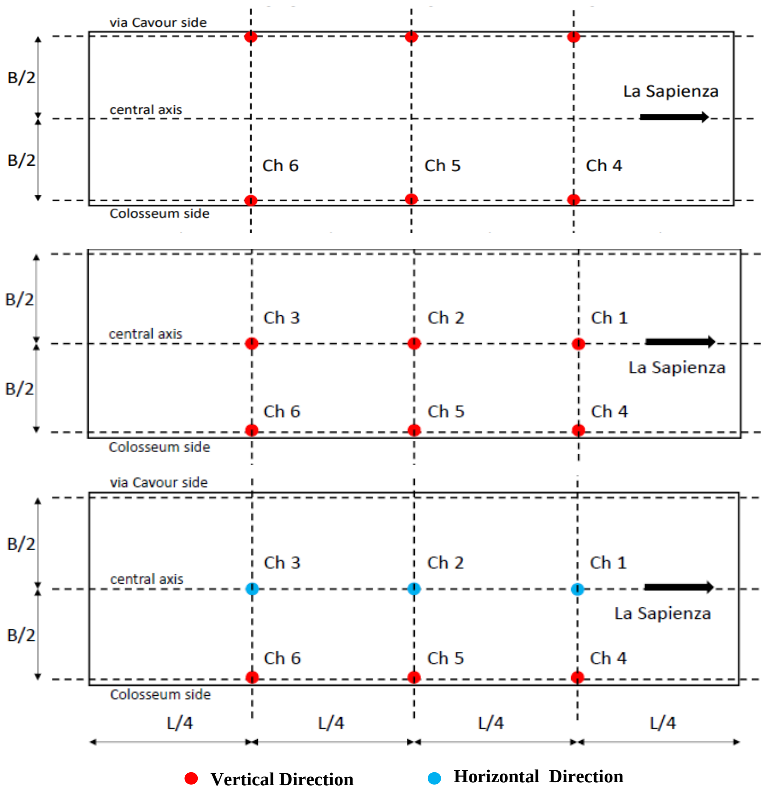

Figure 4.8 Layout of the six accelerometers according to the three setups used for the identification (Red=Vertical, Blue=Horizontal)

4.1.5 Results of the OMA identification and the comparison with the FE model

The well known Frequency Domain Decomposition is combined with the Stochastic Subspace Identification for detecting the modal features of the bridge. The removal of potential trends in the signal, the signal resampling, and a 50% overlapped Hanning's window is implemented before extracting the frequency content through Welch's method and carrying out the singular value decomposition of the Power Spectral matrix. Dealing with the SSI procedure, all the parameters selected for the signal properties are chosen according to Magalhaes et Al. [186] including the techniques used for merging the three setups [230]. The OMA outcomes are illustrated through the plot of the first singular value and the stabilization diagram in Figure 4.9. Then, the experimental mode shapes chosen for the comparison with the numerical model are illustrated in Figure 4.10 whose frequency and damping ratios are listed in the following Table 4.2.

Table 4.2 Natural frequencies and Damping ratios of the Annibaldi bridge.

Mode	Frequency (FDD) [Hz]	Frequency (SSI) [Hz]	Damping Ratio
1° Bending	4.3	4.1	2.1%
1° Torsional	8.9	8.8	3.6%
2° Bending	11.4	11.5	2.2%
2° Torsional	14.5	14.5	1.6%
3° Bending	22.3	22.2	1.5%

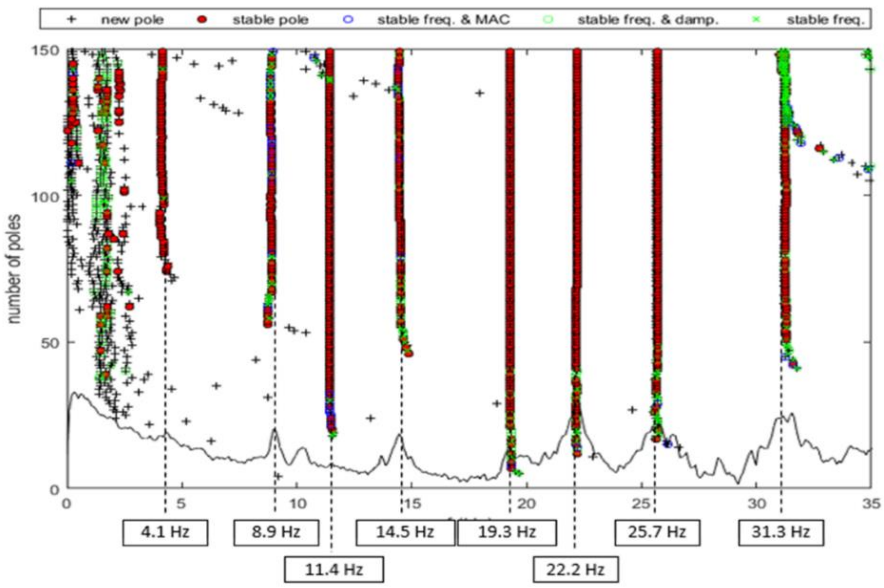

Figure 4.9 Plot of the first singular value (FDD) and the stabilization diagram from the SSI algorithm

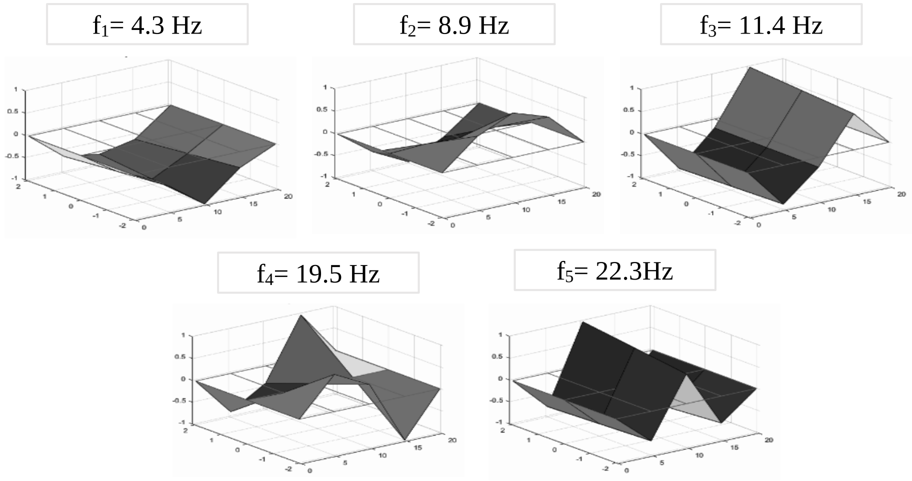

Figure 4.10 Experimental modal shapes resulting from the signal processing,

The obtained experimental mode shapes are then compared with those provided by performing the modal analysis with SAP2000. The results are collected in Table 4.3 with the picture corresponding to the numerical mode shapes illustrated in Figure 4.11, finding a good match with the experimental outcomes.

Table 4.3 Comparison among experimental and numerical outcomes.

Mode	Experimental Freq. [Hz]	Numerical Freq. [Hz]	Error	MAC
1° Bending	4.1	4.1	0%	0.99
1° Torsional	8.8	8.7	-1.13%	0.98
2° Bending	11.5	11.9	3.36%	0.99
2° Torsional	14.5	15.4	5.84%	0.92
3° Bending	22.2	22.9	3.05%	0.93

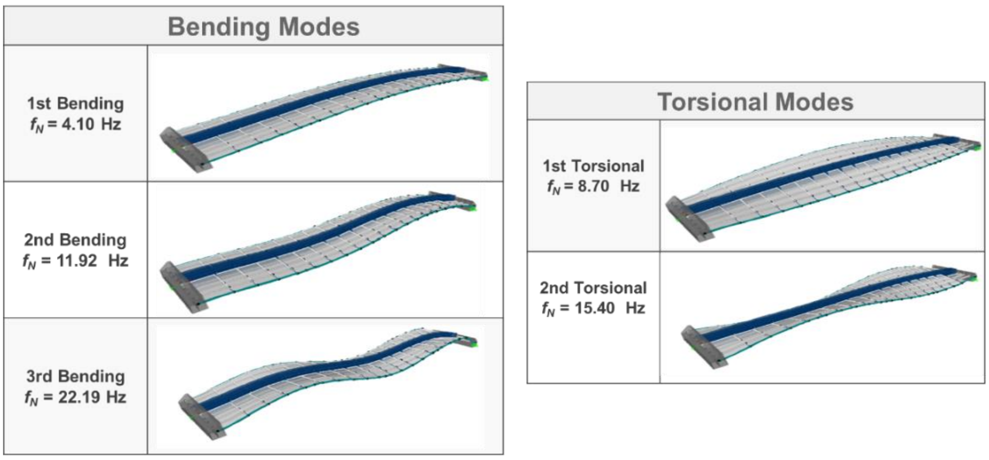

Figure 4.11 First five mode shapes of the FE model

4.2 Bacchelli Bridge: Dynamic Identification and Monitoring

Originally, the *“Sussidiaria_Sud_della_via_Emilia_Ponente”* project consisted of the construction of a small highway in Borgo Panigale and a highway between "Asse Sud Ovest" near "Certosa" in Bologna. The project was submitted to the Municipality of Bologna in the late 1960s, facing the upcoming traffic increase and the increment in the number of large vehicles on regular roads and so improving the road network of Bologna.

The layout of *“Sussidiaria_Sud_della_via_Emilia_Ponente”* extends from west to east 600 meters from the *“Via Emilia”* Street, one of the oldest and most important Italian highways.

Starting from the Borgo Panigale tollhouse, crossing the Casalecchio side road and the Bologna-Pistoia railway to reach the Reno River. As shown in Figure 4.12, the construction of the Bacchelli bridge linked the two river banks allowing the river crossing.

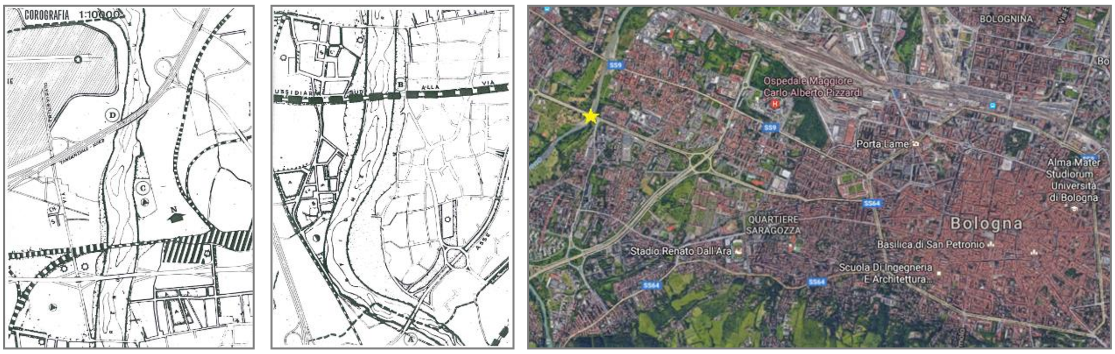

Figure 4.12. Picture of the terrain (left), the bridge over the Reno River (centre) and GPS Position (right).

The shape of *“Sussidiaria_Sud_della_via_Emilia_Ponente”* was defined by examining the size and average velocity of the traffic flows. The width of the street is 30 m and consists of two roadways divided into three lanes and connecting the city of Modena and Bologna.

4.2.1 The geometry of the bridge

The knowledge of one building is essential enabling a correct assessment of its structural health and safety conditions. The original structural state sets the starting point for detecting any potential variation in time associated with the material ageing or the occurrence of damage.

Consulting the original reports and drawings, if they exist, provides basic information about the geometry of the structure and the corresponding material used for the construction, which suggest all the parameters needed for creating a preliminary FE model of the structure of interest. The Bacchelli bridge is a multi-span bridge made of concrete: two simply-supported twin decks cross each span of 30 m, covering the total length of the bridge (320 m), while nine piers and two abutments are the vertical elements (Figure 4.13). Every single deck shown in Figure 4.14 is 30 m long and 15 m wide and consists of a grillage of eight post-tensioned concrete girders and five transverse beams, also post-tensioned. A 200 mm slab made of ordinary concrete completes each deck sustaining a 250 mm tout-venant road pavement and the traffic loads, which are distributed into three lanes and one sidewalk. Figure 4.15 includes some views of the Bridge.

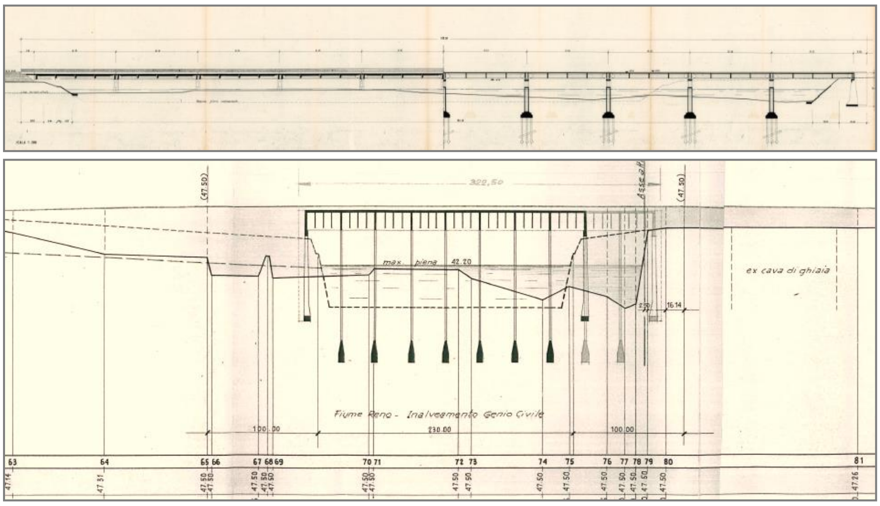

Figure 4.13. Sagittal section of the *"Sussidiaria_Sud_of_Via_Emilia"* on the Reno river and the detail of the Bacchelli Bridge.

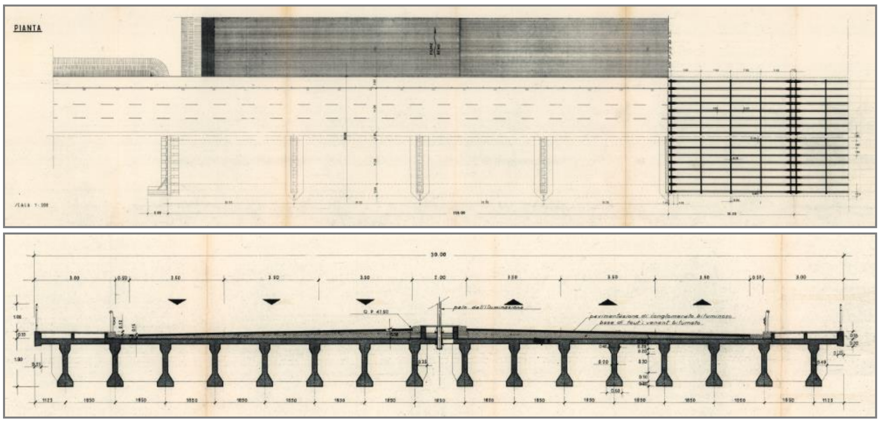

Figure 4.14. Plan view and Cross-section of the Bacchelli Bridge

Figure 4.15. Lateral and bottom views of the concrete deck.

Concerning the vertical elements, the upper part of the piers is a frame-like structure of 16 columns and a single beam, that becomes a box 12 m long after 2 m (Figure 4.16); the abutments act as a cantilever against the ground pressure (Figure 4.17). At the time of construction 4 soil investigations were carried out for the soil characterization: two vertical investigations were performed near the abutment, while the remaining two characterized the soil of the riverbed. Consistently with the typical surrounding area, the internal friction angle of the soil and its strength were estimated at 35° and 0.25 MPa leading to the need for a piled raft foundation for all the vertical elements.

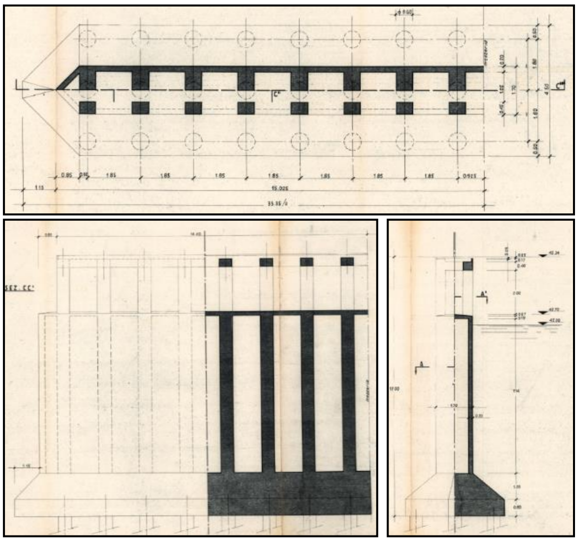

Figure 4.16. Details of a piers

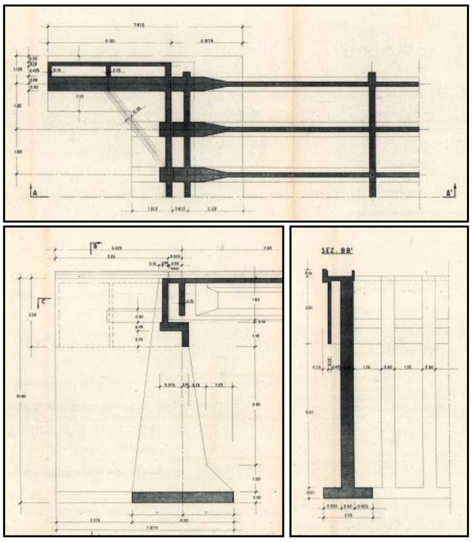

Figure 4.17. Details of the abutments

4.2.2 *Cross-section details and Materials*

The technical report of the bridge provided by the Metropolitan City of Bologna addresses all the calculations and lists all the material properties involved in the bridge construction. The mechanical properties of the materials are collected in Table 4.4 and Table 4.5, while a density of 18 kN/m^3 was adopted for the calculation of an equivalent distributed mass due to the non-structural elements such as the pavement and the sidewalks.

Table 4.4 Mechanical properties of steel bars and wires.

Steel	σ_{max} [MPa]	Young Modulus [MPa]
“Aq 42 ÷ 50”	140	210000
“Aq 50 ÷ 60”	180	210000
“TOR”	200	210000
High strength	1700	210000

Table 4.5 Mechanical properties of concrete.

Concrete	$\sigma_{t,max}$ [MPa]	$\sigma_{c,max}$ [MPa]	Young Modulus [MPa]	Density [kN/m^3]
Ordinary	6.5	20	30000	25
Post-tensioned	6.5	50	37000	25

Each one of the eight girders is a common *"I-Shape"* post-tensioned beam, that is 1.60 m tall and is integral with a 0.2 m concrete slab made of ordinary concrete, whereas the cross-section of the transverse beams is rectangular 1.40 m x 0.25 m. Figure 4.18 illustrates the geometry of main and secondary girders including the layout of the seven steel cables at the ends and the midspan of the beams. Each cable consists of 32 ø6 mm steel wires while the resulting parabolic arrangement of the cables is characterized by a midspan sag of 0.49 m. Then, additional steel reinforcement was added against shear, in particular, ø14 rebars were placed according to the layout of Figure 4.19 with 0.1 m, 0.2 m, and 0.3 m of spacings in the intervals 0-1, 1-2, and 2-4, respectively.

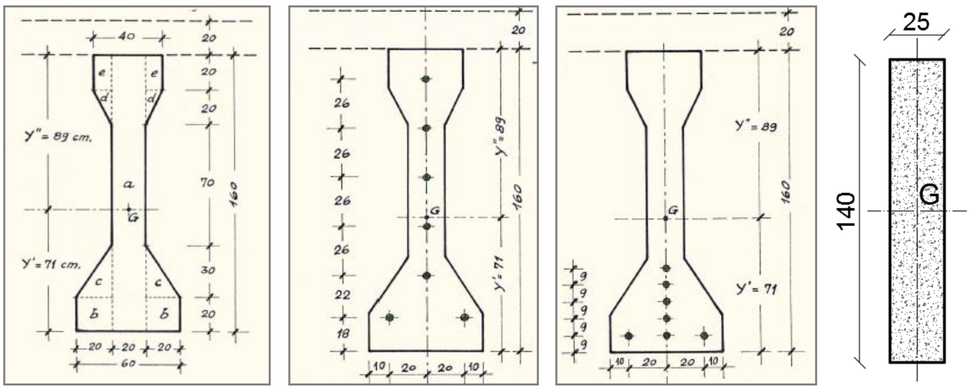

Figure 4.18. Cross-section of the girders and the cable layout at their ends and mid-span.

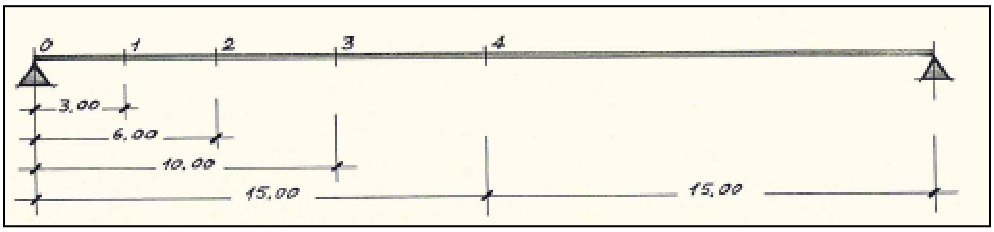

Figure 4.19. The layout of transverse steel reinforcements.

Concerning the reinforcement of the transverse beams and the concrete slab, 2 straight cables of 20 ø6 mm steel wires were adopted as longitudinal reinforcement, and ø14 mm stirrups were used against shear every 0.25 m; whereas 6 and 3 ø12 mm rebars were placed respectively at the top and the bottom of the concrete slab with 3 ø10 mm every meter as transverse reinforcement. According to the geometry and the material properties, the resulting inertia moments become 0.14 m^4 and 0.16 m^4, respectively for the main and secondary girders, and 0.34 m^4 for the main girders when the collaborating width of the slab is considered in the calculations.

Lastly, considering an independent slab for each span and an inspection of the bridge deck, the type of steel bearing illustrated in Figure 4.20 suggests the simply supported behaviour of each deck with an external hinge corresponding to the bottom of each girder.

Figure 4.20 Photo of the detail of the steel deck bearing device

4.2.3 Finite Element Model: definition and selection

As mentioned in the previous section, since each deck is independent of the others, it can be studied separately, and the model of one deck is needed to be able to deal with the calibration procedure. Several numerical models have been investigated to choose the best-compromised solution between model accuracy and computational cost. Starting from the analytical solution of the dynamic equilibrium, additional more sophisticated numerical models were created with the Software Strand7 to improve the accuracy of the estimates by comparing all the frequency sets.

A short description of each studied model is reported below:

- *Equivalent Simply Supported beam – Analytic Solution of the Dynamic Equilibrium*: the first step addresses the frequency calculation based on the dynamic equilibrium of a simply supported Euler-Bernoulli beam with equivalent mechanical and elastic properties from the technical report Figure 4.21.

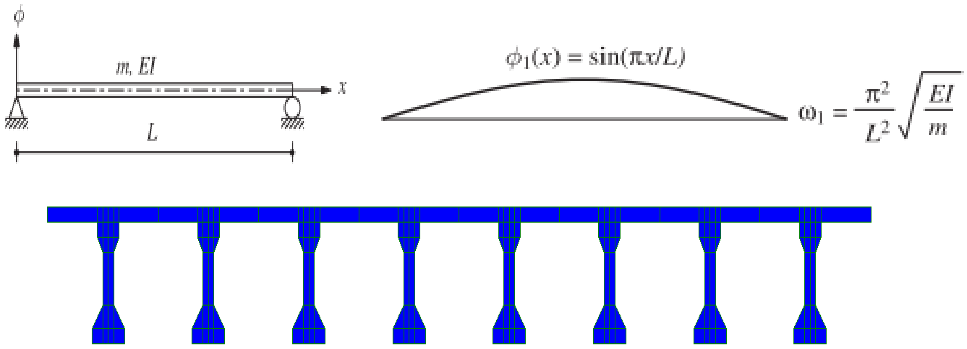

Figure 4.21 Analytical model of the equivalent beam and its cross-section

- *One dimension – Equivalent beam model and Composite equivalent beam mode:* The first model is defined by assigning an equivalent density and a solid cross-section to the beam elements. Then, the cross-section is split into girder and slab portions by using offset or rigid link elements connecting their centres of gravity. That modelling allows the assignment of different Elastic Moduli respectively to the ordinary concrete of the slab and the high strength concrete of the girders. The mass corresponding to each transverse beam is added according to its position (see Figure 4.14). Neglecting the torsional stiffness, mono-dimensional models are usually plane models where only flexural modal shapes are involved. According to Figure 4.22, even the distance between the support and the centre of gravity of the beam is considered by adding one rigid link.

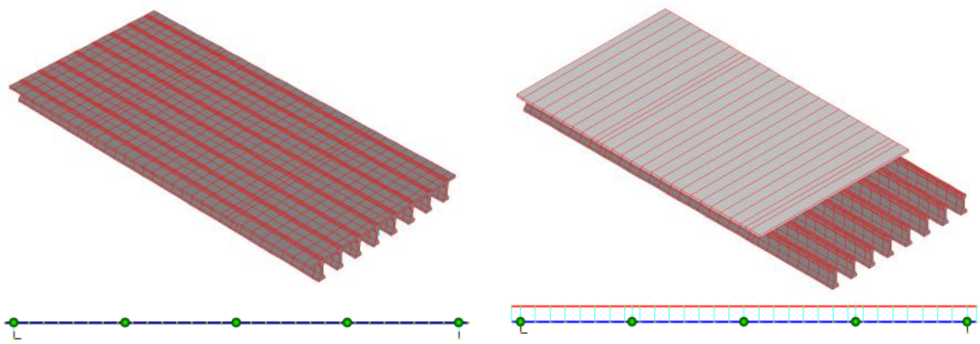
Figure 4.22 Equivalent beam models

- *Spatial grillage of beams:* Spatial models, similar to those shown in Figure 4.23, are created by crossing beam elements in a 3D space, or created by coupling beam and plate elements. In the first model, main and secondary girders have been modelled with beam elements separately, while the slab is created by crossing other beam elements along with the two main directions. The bidirectional bending stiffness of the slab is reproduced within one-dimensional elements, thus the beam elements have the same stiffness in each direction, even though the elements along the shorter direction are massless avoiding the double computation of the slab mass. Typically, the bi-directional problem is solved using plate elements instead of a beam grid, achieving equivalent behaviours.

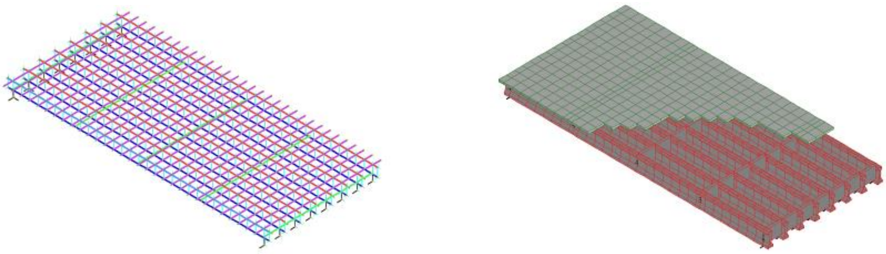

Figure 4.23 Two different spatial models of the deck: only beam grillage (left), beam-plate coupled model (right)

- *Spatial plate/solid model:* two more numerical models are created involving only plate or solid elements only. Since the computational cost grows very fast with the complexity of the model, a beam-plate model is chosen as the most suitable model for having a good approximation of the deck behaviour, even if also the results of the modal analyses carried out on the plate and solid models provided consistent results.

The final FE model illustrated in Figure 4.24 consists of two twin grillages of beam elements modelling the 5 secondary beams and the 8 main girders linked to a concrete slab modelled with shell elements. Then, the weight corresponding to the non-structural elements is applied as equivalent distributed masses on the slabs. Concerning the restraints, according to the simply supported scheme one roller and one external hinge are added below each beam, neglecting the movement orthogonal to the bridge axis. Lastly, an elastic spring is placed along with the longitudinal direction of the bridge in the position of each roller. It is to observe that since the two existing twin decks of the same span share a concrete slab along with one of their side (see Figure 4.14), the model includes both the decks. The model can be reduced considering one deck only by exploiting the structural symmetry, but non-symmetrical mode shapes may be neglected.

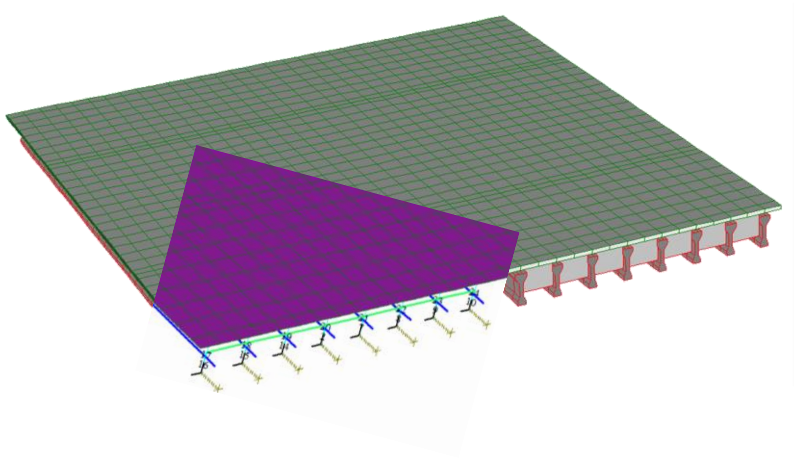

Figure 4.24 Beam-plate numerical model of the Bacchelli bridge deck

4.2.4 Experimental setup for the Operational Modal Analysis

The experimental investigations involved a pair of CX1 accelerometers [180] placed at the midspan and the quarter of the deck length of each span according to Figure 4.25, where also their orientation is illustrated. Since each deck behaves as a simply supported beam, the measurements were collected for each deck separately. The triaxial accelerometers were placed next to the sidewalks as the only location without any interference with the traffic crossing the bridge. A preliminary suggested the value of the first natural frequency of the bridge equal to 3.8 Hz, thus a time length of 5 minutes was chosen for recording the accelerations induced by the traffic flow observing the limits suggested in *Brincker et Al.* [226]. An initial sample rate of 2000 sps was adopted for the measurements, even though each time series was resampled to have a frequency bandwidth of 0-100 Hz.

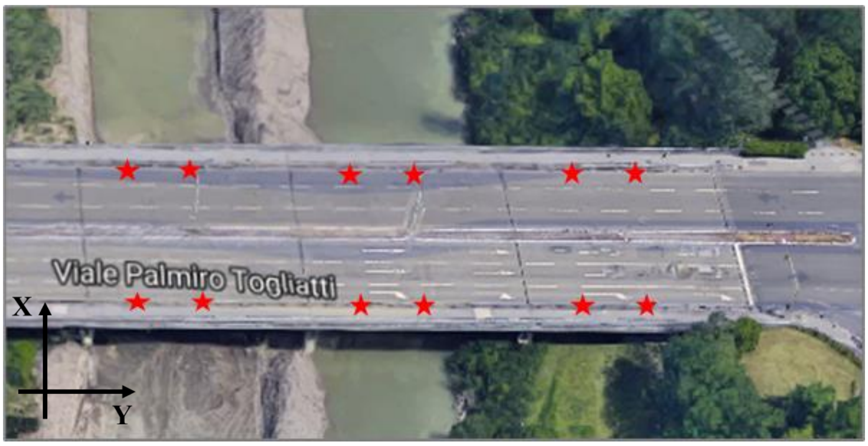

Figure 4.25 Sensor layout for the dynamic investigations

4.2.5 *Results of the OMA identification and updating of the FE model.*

The well-known Frequency Domain Decomposition algorithm is used for the data processing implementing a 50% overlapped Hanning's window before extracting the frequency content through Welch's method and carrying out the singular value decomposition of the Power Spectral matrix. Lastly, the calculation of the coherence [39] among the collected signals validates, with values higher than 0.8, all the natural frequencies listed in Table 4.6 with the corresponding damping ratios.

Table 4.6 Natural frequencies and Damping ratios of the Bacchelli bridge.

Mode	Experimental Freq.	Damping Ratio	Coherence
1° Flexural	3.78	1.9%	0.99
1° Torsional	4.33	2.4%	0.97
2° Torsional	7.20	3.0%	0.90
2° Flexural	13.48	2.9%	0.96

The obtained modal features are used for calibrating some parameters of the numerical model: both Young's modulus and the density of concrete stayed constant because they were validated through nondestructive tests, thus only the non-structural masses and the spring stiffness were hand-tuned and respectively set equal to 4 kN/m^2 and 5e05 kN/m, for fitting the experimental outcomes. Table 4.7 collects the comparison among the experimental estimates and the modal feature of the numerical model, including the calculation of the MAC associated with the two coordinates at which the CX1 were placed. Figure 4.26 illustrates the mode shapes associated with the frequency listed in the table.

Table 4.7 Comparison among experimental and numerical outcomes.

Mode	Exp. Freq. [Hz]	Damping Ratio	Cohe.	Num. Freq. [Hz]	Error	MAC
1° Flexural	3.78	1.9%	0.99	3.79	0.3 %	0.99
1° Torsional	4.33	2.4%	0.97	4.26	-1.6 %	0.97
2° Torsional	7.20	3.0%	0.90	7.02	-2.5%	0.93
2° Flexural	13.48	2.9%	0.96	13.35	0.9%	0.95

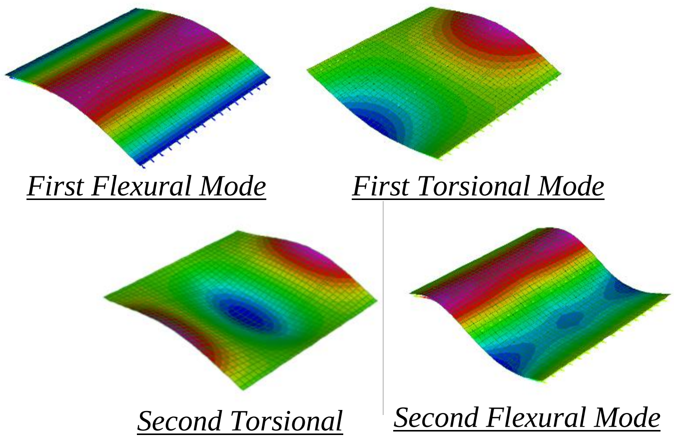

Figure 4.26 Mode shapes associated with the first four natural frequencies

At the same time, all the spans of the Bacchelli Bridge were investigated and the first natural frequencies associated with each deck are consistent along the bridge at both the span sides, showing similar values according to Figure 4.27 and Figure 4.28. Mode three is not always sharp in the frequency spectra, thus it was not possible to detect in some spans.

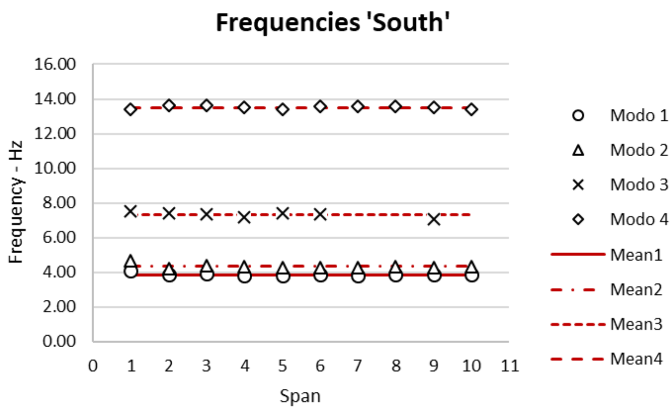

Figure 4.27 Frequencies of the decks from Bologna to Modena - South Side

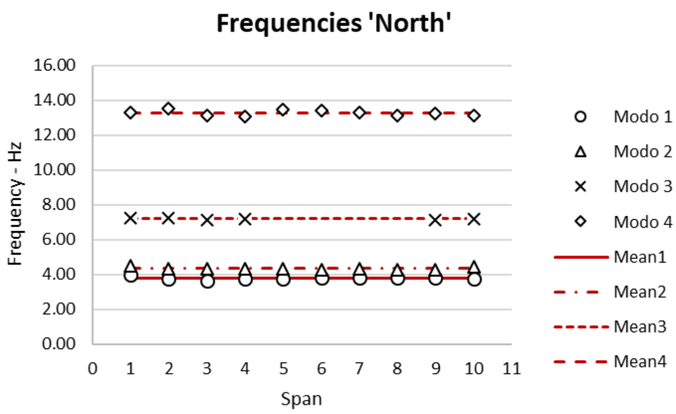

Figure 4.28 Frequencies of the decks from Bologna to Modena - North Side

4.2.6 Monitoring through an accelerometer-based network

After the evaluation of the main frequencies of the Bacchelli bridge, in the context of the European project SHAPE, an accelerometer-based monitoring system was installed in one of the twenty decks of that bridge. The system was designed for low-cost installations, monitoring periodically (e.g. once an hour), using one or two CX1 accelerometers and/or several low-cost accelerometers. This section discusses the characteristics of acquisition and wireless transmission box, named Winet Box. It was designed and manufactured by Winet S.R.L. [231], Italy, with the collaboration of the University of Bologna.

Winet Box is used in the Bridge Monitoring Project to monitor the physical condition of some structures (e.g., bridges) by analyzing data from inertial sensors, such as accelerometers, and inclinometers. Actually, it mainly consists of a single-board computer that is directly connected to the sensors to collect data in predetermined time slots and equipped with a transmission system for the remote data storage on the cloud server. All the collected information was made available for visualization, data processing and analysis based on the final user needs.

The first version of the box discussed in this section involves the CX1 accelerometer, deeply used in this work. Then, two low-cost STM (ST-Microelectronics) sensors took place of the CX1 in the last version providing a cheaper solution. This section addresses the differences between both the solutions, comparing the corresponding outcomes in terms of acceleration, frequency estimation and stability of the system over time.

In the following, some specific requirements for the box design and the component selections are outlined:

- The Shape Box may be installed in outdoor environments, on exposed sites, such as bridges. This requires a careful selection of components capable to work in an extended temperature range from below zero to + 40 °C

- The box design includes the physical container which has been selected based on the International Protection Marking (IP) criteria for guaranteeing the component isolation from atmospheric and external agents, such as rainwater or snow. All the selected connectors and cables for wiring the system components follow the same isolation requirements

- The data acquisition campaign had been performed at some points of a structure that are difficult to physically reach and are in place 24 hours per day. For this reason, the wireless system is used for transmitting data between the sensor and the cell phone. The

> Winet Box is powered independently to cover structure points where cabled power solutions are unavailable. Therefore, the monitoring box is equipped with a battery charged by a solar panel. A power consumption analysis of each device has been performed to estimate battery power capacity and its dimension.

As a consequence of this premise, after the description of the system architecture including each component of the system, a careful power budget analysis is presented for selecting the correct battery capacity size. Lastly, the results collected by the two versions of the monitoring are discussed.

Figure 4.29 shows the system architecture for data acquisition, transmission and processing, while Table 4.8 and Figure 4.30 collect all the devices, including their ID name, size and reference technical documents. The sensor board sends the collected data to the monitoring box in predetermined time slots. At each acquisition time slot, the box collects the received data from the sensors using a Single Board Computer (SBC). The SBC has equipped with a Solid State Drive (SSD) memory for the data storage preventing potential data losses. The received information is then delivered to a cloud-based server in which all the acquisition campaign data for the preset periods is available for the final user. Then, an expansion board for smartphone-network/computer connection is equipped to the SBC: the board is a full-size mini Peripheral Component Interconnect (PCI)-e 3G/4G Card with a SIM-Card holder. The data can be downloaded to appropriately perform signal processing.

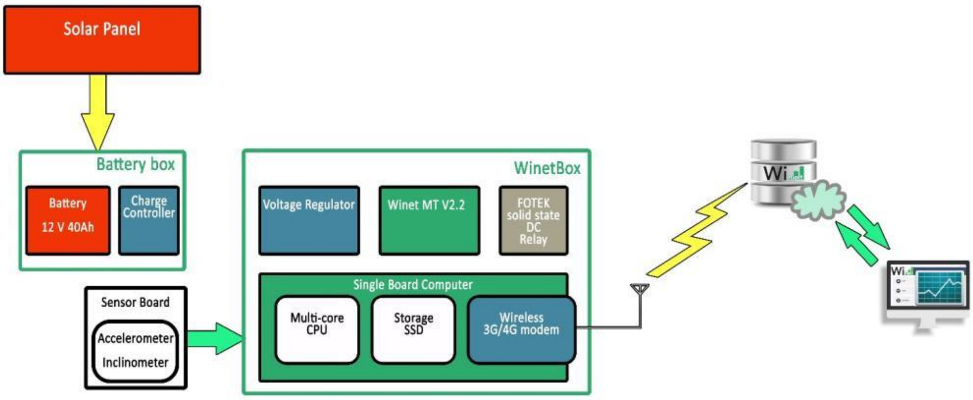

Figure 4.29 Architecture of the monitoring box

Table 4.8 List of the box components

Device type	***Manufacturer***	***ID***	***Size [mm]***	***Ref.***
SBC	Advantech	MIO-3260CZ22GS8A1E	100 x 72 x 26	[1]
3G/4G Modem	Advantech	EWM-C109F601E	51 x 30 x 6	[2]
Battery	FAM	BE 12040	198 x 166 x 174	[3]
Automatic Power Module	Analog	LTC3780	78 x 47 x 15	[4]
Charge Controller	Epever	Ls0512E	93 x 65 x 20	[5]

[1]. http://www.advantech.com/products/1a2b922a-ce03-4960-8b8d-0fe06d0ac6cf/ewm-c109f601e/mod_9d287754-dfb9-4d1c-b7ab-e510d70b2dd5

[2]. http://www.fambatterie.it/prodotti/batterie-agm-e-gel/batterie-standard/batteria-be-12040-detail?lang=it

[3]. http://www.advantech.com/products/mi%7B%7B--o_ultra_single_board_computers/mio-3260/mod_9b95d114-45d5-433a-aab5-33a5dd4f4fda

[4]. http://www.analog.com/media/en/technical-documentation/data-sheets/3780ff.pdf

[5]. http://www.epsolarpv.com/en/uploads/news/201801/1516874037785532.pdf

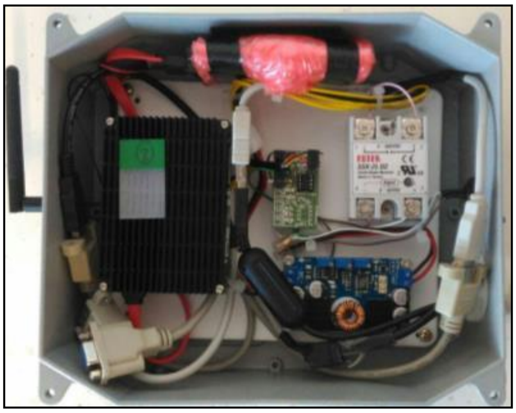

Figure 4.30 Layout of the box components

The monitoring box is then equipped with a rechargeable battery connected to a solar panel to be autonomous in its functioning: the voltage regulator device in Winet Box regulates the power from the solar panel to the battery. Therefore, this task required a careful single device power consumption analysis and estimation of the power budget presented in the following to define the solar panel capacity and the battery dimensions. The Box is kept active only for the acquisition and transmission times for the sake of minimizing energy consumption. To achieve this goal, the monitoring box uses the SBC’s built-in programmable Watch Dog Timer (WDT) which is designed to switch on the acquisition and transmission system only at predetermined times, for a specific period. Once the box is activated, it powers the CX1 (or STM devices) sensor for the amount of time required for the acquisition using the relay on the Winet MTW2.1 Atmel Attiny based board. Then, data from the sensors are cyclically read by the box and stored in the SSD. In the transmission phase, data are sent to the server and a new configuration, if available is downloaded. The sensors are then placed in sleep mode waiting for the next scheduled wake-up.

Concerning the power budget analysis, the proper sizes of the solar panel and the appropriate capacity of the battery are chosen to optimize the device activity: all the system acquisition and transmission devices are active (except for WDT) only for fixed periods, avoiding unreasonable drains of the battery. The list of the operating times associated with each acquisition cycle is provided in Table 4.9, setting the length of the acquisition equal to 300 seconds according to the minimum length of the time series for OMA purposes provided in Brincker et Al. [232].

Table 4.9 Operative time of the monitoring box

Time	[sec]
OS Starting	30
Acquisition	300
Transmission	60

The whole system is switched off during the inactive period. Since the SBC needs some time to boot itself, the acquisition time is defined as 300 seconds for acquiring data from the sensor board, whilst the transmission time is estimated at 60 seconds for establishing a connection with the closest cell and for delivering all the collected information. It means that the SBC and the sensor board (i.e., SENSR CX1 which has power supplied from the SBC) are kept active for a longer time, while the 3G/4G modem is active only for the transmission time.

Table 4.10 summarizes the required current for every single device that has been calculated considering one acquisition and transmission phase in one hour (N. of cycles = 1). Then, the effective operating time in an hour has been calculated in column five.

Table 4.10 Effective current consumption for each device

Device type	Required Curr. [Ah]	Peak Current [Ah]	Operating time [hour]	N. of cycles	Required Curr. [A]
SBC	0.35	-	0.044	1	0.0155
3G/4G Modem	<0.7	1.5	0.018	1	0.0150
Sensor Board	0.2	-	0.044	1	0.00883
Total	**1.25**	**1.5**			**0.03883**

The power/consumption calculation suggested a suitable capacity of the solar panel equal to 10 W, with the features listed in Table 4.11. The effective power of the panel is calculated by taking into consideration the Effective Hours of Full Sun [EHS]. Because of the variation in the intensity of the Sun's radiation during the day and also the variations in the length of the day, it is difficult to make comparisons of the Sun's energy falling upon the Earth at different locations.

Table 4.11 Features of the solar panel

Device Type	Generated Power [W]	Generated Current [Ah]	EHS	Generated Current [Ah]
Solar Panel	10	0.58	1.5-2	0.036

The nominal power of a panel, in this case, equal to 10 W, is calculated in optimal conditions, in particular at midday, with the panel oriented to the South, with solar radiation equal to 1000 W/m2 and cellular temperature equal to 25◦C. However, this condition is not satisfied during all the day lights and it depends on the location and the weather conditions.

For this reason, EHS estimates the number of hours under ideal conditions. Statistically, EHS is equal to 2 during the winter season and 4 during summer for northern Italy. Ensuring the proper power budget an underestimated EHS equal to 1.5 or 2 if the power budget is guaranteed for a limited (158 days) or an unlimited amount of time. The energy calculations and safety margins led to the choice of a 30W solar panel and a 12V and 40Ah battery. The installation of the monitoring box on the Bacchelli bridge is illustrated in Figure 4.31 and Figure 4.32. Figure 4.32 shows the two different layouts chosen for locating the sensors. Both the solutions present the common location on the upper pier for the box containing the Single Board Computer, the storage device and the transmitting platform and the second girder for placing the accelerometers.

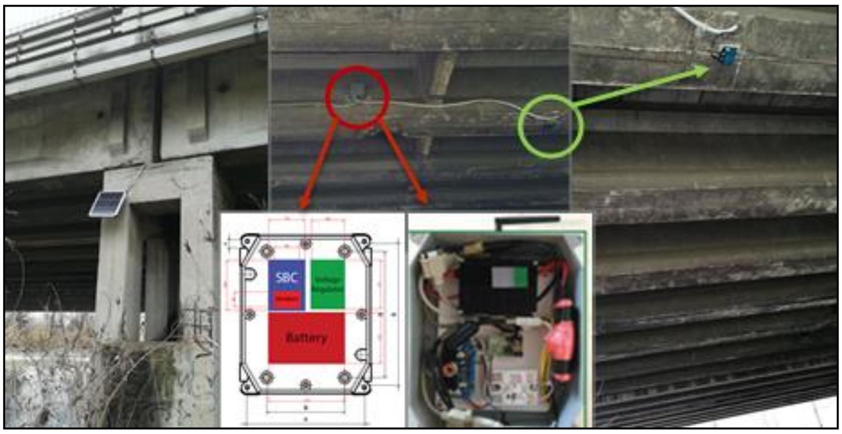

Figure 4.31 Installation of the box on the Bacchelli Bridge

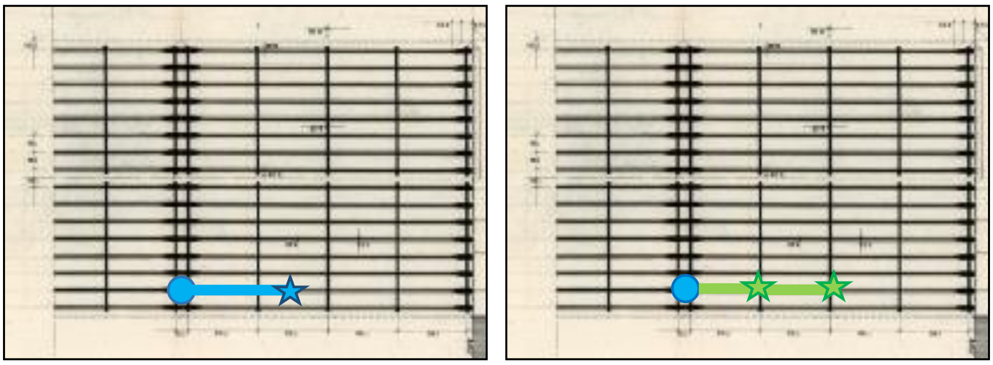

Figure 4.32 Location of the box (blue round) and the two setups: CX1 (blue star) and STM (green star)

Then, having the plan view of the deck chosen for the installation, the CX1 (blue star) is placed at one-third of the girder length, while the two STM devices (green stars) are placed at the mid-span and one-fourth of the span, both the sensors are illustrated in Figure 4.33. Each one is set to record 300s of traffic-induced vibration with 200 Hz of the sampling frequency, while the signal processing is performed offline on a workstation.

CX1 (a) **STM (b)**

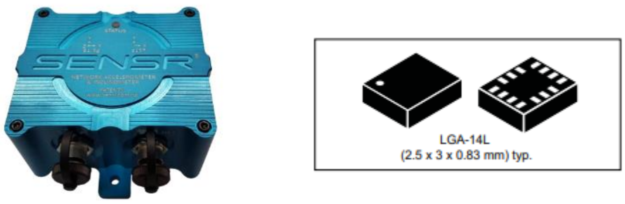

Figure 4.33 Picture of the sensors CX1 (a) and STM (b) [180], [233].

The choice of using STM devices is mainly driven by the attempt to reduce the cost of the whole system increasing the spatial resolution of the measurements. CX1 is a very sensitive MEMS capacitive accelerometer whose no information about its real sensitivity and noise density values are provided in the datasheet. Due to the high cost and the huge energy consumption of the CX1, two cheaper STM sensors are installed on the bridge [233]. The typical samples of recordings are sown in Figure 4.34: on the left the data of the CX1, while the data acquired by the STM are illustrated on the right. No significant frequencies can be detected from the X and Y data for both types of sensors, thus only the discussion of the Z direction is provided. It is to mention that no more significant results have been obtained from the two STM sensors even using the Frequency Domain Decomposition. Concerning the recordings in the direction of the gravity (Z), the CX1 seems more sensitive to detecting the first frequency sharply, while some suggestion about the second bending frequency is provided in the range of 10-15 Hz, even though no clear peaks are present in the spectrum. On the contrary, as expected the peak corresponding to the second bending mode is always absent in the sensor placed at the midspan (node of the second bending mode), whereas it is present in the spectrum corresponding to the other sensor placed at one-fourth of the girder length, even if it is not always detectable.

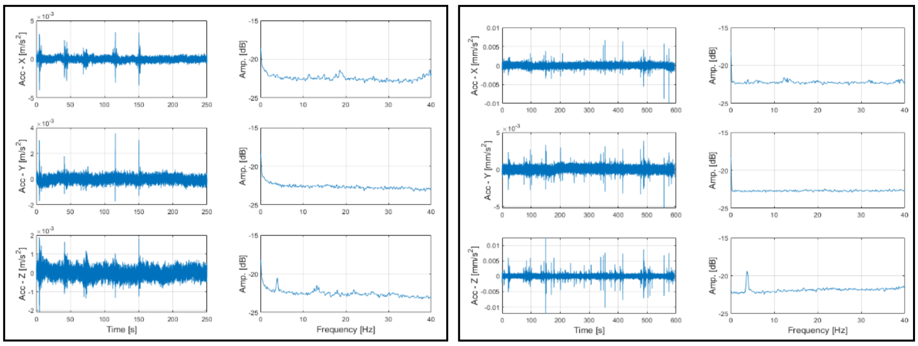

Figure 4.34 Recordings of the acceleration on the 3-axes X-Y-Z and the corresponding power spectra of the CX1 (on the left) and the STM (on the right).

Unfortunately, due to the position of the installed sensors, no information about the torsional mode is detected. For this reason, only the first frequency is collected over time appreciating the typical frequency daily variation caused by the temperature (Figure 4.35, Figure 4.36). The CX1-based monitoring system is tested for two months even appreciating the seasonal variation, while the STM-based system is tested only for three weeks only for the comparison of the recordings: since the testing period was not affected by significant variation in the temperatures, no significant variation of the first natural frequency of the deck is detected, but the first frequency is consistent with the expected values.

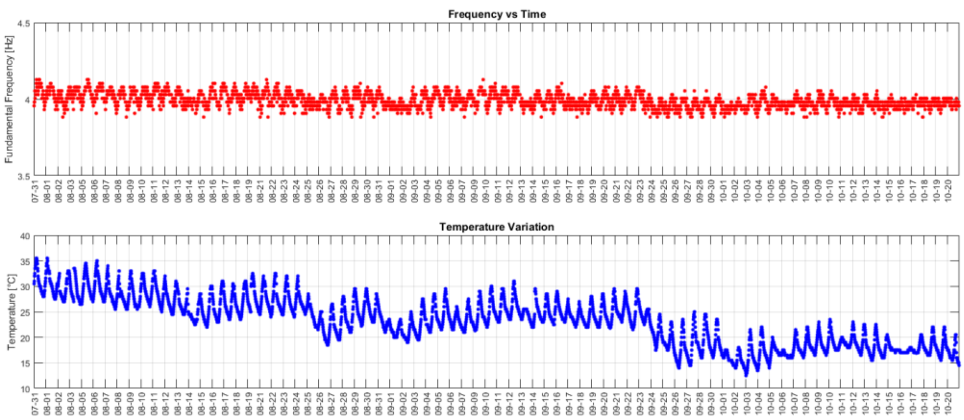

Figure 4.35 Daily frequency variation collected with CX1.

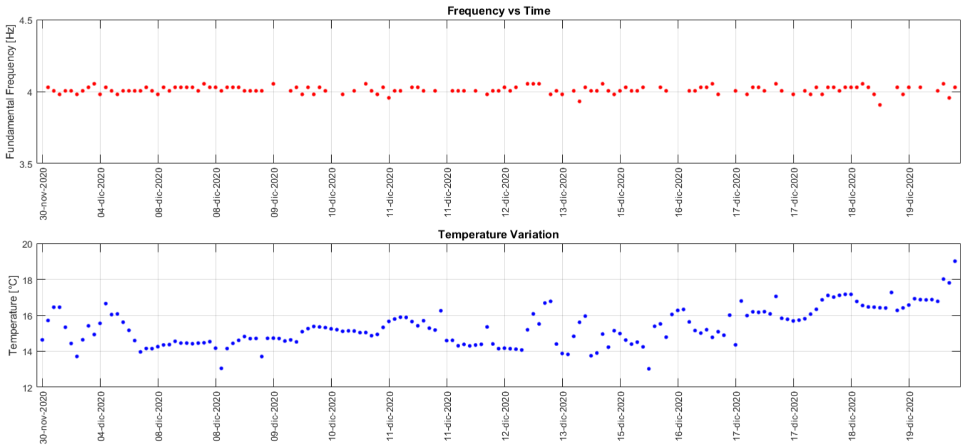

Figure 4.36 Daily frequency variation collected with STM.

4.3 Contribution in the field of dynamic investigation of existing structures

This chapter includes some dynamic investigations carried out on two existing bridges assessing their dynamic behaviour and "calibrating" their corresponding FE models. The Annibaldi bridge is tested using ICP accelerometers placed on the deck surface according to three different setups. Each setup is merged with the other by using the three sensors which were kept fixed in the same position for all the layouts, as reference. The first five modal shapes have been estimated via OMA algorithms from the experimental data, and then used to be compared with those obtained through a Finite Element model, whose cross-section and material properties are calibrated on the experimental outcomes.

A similar approach was followed for the Bacchelli bridge in Bologna, where all its spans were investigated through dynamic tests, even if only two accelerometers were involved in the experimental campaign. The first three main frequencies have been estimated and used for creating the corresponding numerical model of the bridge. Then, having the value of the fundamental frequency, two prototypes of an accelerometer-based monitoring system have been installed on one deck of the bridge deck for track it over time, finding a suitable solution for following the evolution of the health condition of the bridge.

5 Conclusions

5.1 Summary

In the first part of the thesis, the effect of local damage on the modal feature has been discussed mainly concerning a steel frame and a composite steel-concrete bridge. Considering the variation of the fundamental frequency of the small bridge, the effect of increasing severity of two local damages has been investigated. Moreover, the comparison with a 3D FE model is even presented establishing a link between the dynamic properties and the damage features which will be useful in planning the condition assessment through dynamic monitoring of real deteriorated full-scale bridges.

Then, moving towards a diffused damage pattern, four concrete beams and a small replica of a concrete deck were loaded up to the yielding of the steel reinforcement. The fundamental problem of expressing the stiffness deterioration in terms of frequency shift has been reconsidered with the help of a large set of dynamic experiments on simply supported ordinarily reinforced concrete beams discussed in the literature have been collected. The comparison of the normalized non-dimensional load-frequency curves suggested a significant agreement among all the experiments. Thus, in the framework of damage mechanics, the phenomenon of the "breathing cracks" has been discussed and the analytical formula able to explain the observed frequency decay has been proposed. The formula is still valid both for concrete beams and the small bridge deck and showed a good agreement with the worked-out experiments.

Lastly, some dynamic investigations of two existing bridges and the corresponding Finite Element Models are presented in Chapter 4. Moreover, concerning the bridge in Bologna, two prototypes of a network of accelerometers were installed and the data of a few months of continuous monitoring have been processed and then illustrated.

5.2 Concluding remarks and main contribution

The thesis addresses some aspects of the dynamic investigation of structures, especially regarding bridges and dealing with the presence of damage and tries to connect theoretical results, real on-site monitoring architectures and numeric detection procedures.

After introducing the state of the art in system identification and damage detection, several case studies concerning laboratory structures and existing structures are presented and discussed.

The lab structures include the investigation of a steel frame, a set of concrete beams and two small bridges on which it has been performed the identification of the structural features associated with their dynamic behaviour and the evaluation of the damage occurring on the structural elements. In this context, dealing with concrete structures the theory of breathing crack is used for explaining the damage-induced frequency decay. Lastly, some OMA techniques have been used for assessing the dynamic behavior of the Annibaldi bridge in Rome and the Bacchelli bridge in Bologna. Hereafter, some final remarks about the findings and main contributions are described.

The problem of local damage affecting the fundamental frequencies of the structure is addressed by studying the dynamic behaviour of a steel-concrete composite bridge deck and a steel one-bay 4-storey frame. Both the experimental campaigns involved the identification of natural frequency and the corresponding modal shapes in the range of up to 100 Hz. The study of the small bridge involved the use of OMA techniques to assess the loss of stiffness caused by the presence of local damages on the main girders with increasing severity and with the support of a FE model of the small deck. After the calibration of the numerical model, all the damaged configurations have been simulated showing a good match with the experiments.
On the other hand, the discussion about the steel frame has provided more details about the damage localization, including an original setup for the dynamic investigation of small and highly deformable structures. In this context, the EMA approach is used for processing the data acquired by the accelerometers and the high-speed camera. The detection of damage has been addressed via the calculation of MAC and COMAC indexes comparing the performances of the two solutions: the use of several markers with the high-speed camera has provided outcomes very close to those obtained from the accelerometer, even though with an improved resolution in terms of spatial description. This suggests the use of the high-speed camera as a promising procedure for investigating laboratory structures

Moving to concrete structures, the consequences on the fundamental frequency of a diffused crack pattern is addressed by dealing with either single concrete beams of Section 3.3.1 or the concrete bridge deck of Section 3.3.2. Considering the assessment of the structural behaviour, a 4PBT and the CX1 accelerometers were used in both the experimental investigations and the structural stiffness evaluations. Several damaged configurations were realized and then studied with a redundant identification of the corresponding modal features. In the framework of these tests, a small-size sensor network designed by the ARCES Lab at the University of Bologna has been validated demonstrating the capability to accurately address both the dynamic vibrational behaviour and the acoustic emission activity of concrete-based structures.

Then, the mechanical explanation of the damage-induced frequency decay of simply supported RC beams has been provided for the first time. The formula proposed in Section 3.3.1 describes the behaviour observed experimentally and explains the contribution of the crack cyclic closure to the final result. Moreover, it is validated with a very large database of experimental tests present in the literature dealing with simply supported RC damaged beams and supported by the use of a FEM model with non-linear elements reproducing the crack closure.
It is evident from the discussion that the onset of a stable 10%-15% frequency reduction (which probably is even steadily slightly increasing due to progressive bond deterioration), is the key response to look for, which suggests the sudden plan of inspection and maintenance activities. The same problem is extended to the simply supported concrete bridge deck of Section 3.3.2, even assessing its residual bending capacity through frequency data.

Lastly, concluding with the two aforementioned existing bridges introduced in Chapter 4, some dynamic investigations have been presented and discussed in the light of assessing numerically their behaviour by calibrating in an optimization process their corresponding FE models.
The Annibaldi bridge, a walkway near the Rome Colosseum, is illustrated showing the setups employed for recording data and the main outcomes achieved in the context of the APESS Summer School at the University of “La Sapienza” in Rome. is tested using ICP accelerometers placed on the deck surface according to three different setups which have been then merged together for the final identification process. The properties of the bridge cross-section and the mechanical parameters of the materials are used for creating an accurate FE model, calibrated on the experimental outcomes.
A similar approach was followed for the Bacchelli bridge in Bologna, where all its spans were investigated through dynamic tests. Three natural frequencies have been detected via OMA algorithms and used for creating the corresponding numerical model. In the end, having the value of the fundamental frequency, two prototypes of an accelerometer-based monitoring system have been permanently installed on one deck of the bridge for tracking its evolution over time by monitoring the fundamental frequencies. This experiment trying to evaluate the health condition of the bridge during time is still in evolution.

5.3 Suggestions for future research

Further analyses are yet in progress looking at the evolution of the main frequency of the two decks and the Bacchelli bridge over time due to daily and seasonal variation of the temperature by recording acceleration data every hour. After one year of recorded data, the influence of the temperature will be removed by processing the acquired data through some regression or statistical algorithms. Other dynamic investigations are already scheduled to be performed on the two small bridges concerning the consequences of damage on modal shapes and damping ratios. In particular, even the EMA approach will be implemented for more accurate frequency estimation. Finally, both the two decks in their damaged configuration will be strengthened by using carbon fibres or external post-tensioning cables.

The present work provides an experimental benchmark for validating damage detection or system identification algorithms which will be developed in the future. Since time is passing, even the assessment of the effects of corrosion and fatigue might be recorded on the two open space laboratory decks. Lastly, concerning the monitoring system, a wireless sensor network has been recently installed on the bridge to compare the performances with the previous versions, increasing the number of accelerometers and improving their sensitivity.

6 References

[1] Wikipedia, "List of bridge failures," *Wikipedia*. 2021.

[2] A. A. Mufti, "Structural Health Monitoring of Innovative Canadian Civil Engineering Structures," *Struct. Heal. Monit.*, vol. 1, no. 1, pp. 89–103, 2002.

[3] K. Worden and J. M. Dulieu-Barton, "An Overview of Intelligent Fault Detection in Systems and Structures," *Struct. Heal. Monit.*, vol. 3, no. 1, pp. 85–98, 2004.

[4] C. R. Farrar and K. Worden, "An introduction to structural health monitoring.," *Philos. Trans. Ser. A, Math. Phys. Eng. Sci.*, vol. 365, no. 1851, pp. 303–315, Feb. 2007.

[5] D. E. Bently, C. T. Hatch, and B. Grissom, "Fundamentals of Rotating Machinery Diagnostics," 2003.

[6] P. J. Shull, *Nondestructive evaluation: theory, techniques, and applications*. CRC press, 2002.

[7] D. C. Montgomery, *Introduction to Statistical Quality Control*. Wiley, 2020.

[8] K. Worden, "Structural Health Monitoring using Pattern Recognition," *New Trends in Vibration Based Structural Health Monitoring*. Springer Vienna, pp. 183–246, 2010.

[9] W. J. Staszewski, K. Worden, R. Wardle, and G. R. Tomlinson, "Fail-safe sensor distributions for impact detection in composite materials," *Smart Mater. Struct.*, vol. 9, no. 3, pp. 298–303, 2000.

[10] M. P. Henry and D. W. Clarke, "The self-validating sensor: rationale, definitions and examples," *Control Eng. Pract.*, vol. 1, no. 4, pp. 585–610, 1993.

[11] M. A. Kramer, "Nonlinear principal component analysis using autoassociative neural networks," *AIChE J.*, vol. 37, no. 2, pp. 233–243, 1991.

[12] M. A. Kramer, "Autoassociative neural networks," *Comput. Chem. Eng.*, vol. 16, no. 4, pp. 313–328, 1992.

[13] H. Sohn, "Effects of environmental and operational variability on structural health monitoring," *Philos. Trans. R. Soc. A Math. Phys. Eng. Sci.*, vol. 365, no. 1851, pp. 539–560, Feb. 2007.

[14] K. Kumar, P. K. Biswas, and N. Dhang, "Data normalization technique in shm under environmental variations using one-class SVM," in *ICSV 2016 - 23rd International Congress on Sound and Vibration: From Ancient to Modern Acoustics*, 2016, p. Dynamic Acoustics S.A.; et al.; Hellenic Associati.

[15] C. Flexa, W. Gomes, and C. Sales Junior, "Data normalization in structural health monitoring by means of nonlinear filtering," in *Proceedings - 2019 Brazilian Conference on Intelligent Systems, BRACIS 2019*, 2019, pp. 204–209.

[16] J. P. Lynch, "An overview of wireless structural health monitoring for civil structures," *Philos. Trans. R. Soc. A Math. Phys. Eng. Sci.*, vol. 365, no. 1851, pp. 345–372, 2007.

[17] C. C. Kennedy, "Use of Vectors in Vibration Measurement and Analysis," *J. Aeronaut. Sci.*, vol. 14, pp. 603–625, 1947.

[18] M. Döhler, E. Reynders, F. Magalhães, L. Mevel, G. De Roeck, and Á. Cunha, "Pre- and Post-identification Merging for Multi-Setup OMA with Covariance-Driven SSI." 2011.

[19] E. Orlowitz, P. Andersen, and A. Brandt, "Comparison of simultaneous and multi-setup measurement strategies in operational modal analysis," in *6th International Operational Modal Analysis Conference, IOMAC 2015*, 2015, p. Bruel and Kjaer Sound and Vibration Measurement A/.

[20] M. Dohler, P. Andersen, and L. Mevel, "Data merging for multi-setup operational modal analysis with

data-driven SSI," in *Conference Proceedings of the Society for Experimental Mechanics Series*, 2011, vol. 3, no. PART 1, pp. 443–452.

[21] J. S. Bendat and A. G. Piersol, "Engineering Applications of Correlation and Spectral Analysis," 1980.

[22] A. Felber, "Development of a hybrid bridge evaluation system," 1994.

[23] G. A. Papagiannopoulos and G. D. Hatzigeorgiou, "On the use of the half-power bandwidth method to estimate damping in building structures," *Soil Dyn. Earthq. Eng.*, vol. 31, pp. 1075–1079, 2011.

[24] C. Rainieri, G. Fabbrocino, and E. Cosenza, "Some Remarks on Experimental Estimation of Damping for Seismic Design of Civil Constructions," *Shock Vib.*, vol. 17, p. 737452, 2010.

[25] D. J. Ewins, *Modal Testing, Theory, practice and application*. 2000.

[26] C. Y. Shih, Y. G. Tsuei, R. J. Allemang, and D. L. Brown, "Complex Mode Indication Function and its Applications to Spatial Domain Parameter Estimation," *Mech. Syst. Signal Process.*, vol. 2, pp. 367–377, 1988.

[27] R. Brincker, L. Zhang, and P. Andersen, "Modal Identification from Ambient Responses using Frequency Domain Decomposition," *18th Int. Modal Anal. Conf.*, pp. 625–630, 2000.

[28] R. Brincker, C. E. H. Ventura, and P. Andersen, "Damping estimation by frequency domain decomposition," 2001.

[29] L. Zhang and Y. Tamura, "A Frequency-Spatial Domain Decomposition (FSDD) Technique for Operational Modal Analysis," 2005.

[30] S. Gade, N. Møller, H. Herlufsen, and H. K.-H. Brüel, "Frequency Domain Techniques for Operational Modal Analysis," 2005.

[31] P. Andersen and R. Brincker, "Comparison of System ldentification Methods Using Ambient Bridge Test Data," 1999.

[32] G. H. James, T. G. Carne, and J. P. Lauffer, "The Natural Excitation Technique (NExT) for modal parameter extraction from operating wind turbines," 1993.

[33] D. L. Brown, R. J. Allemang, R. Zimmerman, and M. Mergeay, "Parameter Estimation Techniques for Modal Analysis," 1979.

[34] S. R. Ibrahim and E. C. Mikulcik, "A method for the direct identification of vibration parameters from the free response," 1977.

[35] H. Vold, J. Kundrat, G. T. Rocklin, and R. H. Russell, "A Multi-Input Modal Estimation Algorithm for Mini-Computers," 1982.

[36] J.-N. Juang and R. S. Pappa, "An eigensystem realization algorithm for modal parameter identification and model reduction. [control systems design for large space structures]," 1985.

[37] S. R. Ibrahim, "Random Decrement Technique for Modal Identification of Structures," *J. Spacecr. Rockets*, vol. 14, pp. 696–700, 1977.

[38] F. Poncelet, G. Kerschen, J. Golinval, and D. Verhelst, "Output-only modal analysis using blind source separation techniques," *Mech. Syst. Signal Process.*, vol. 21, pp. 2335–2358, 2007.

[39] C. Rainieri and G. Fabbrocino, *Operational Modal Analysis of Civil Engineering Structures: An Introduction and Guide for Applications*. 2014.

[40] J. Antoni and S. Chauhan, "Second Order Blind Source Separation techniques (SO-BSS) and their relation to Stochastic Subspace Identification (SSI) algorithm," 2011.

[41] B. Peeters and H. Van der Auweraer, "PolyMAX: A revolution in operational modal analysis," in *Proceedings of the 1st International Operational Modal Analysis Conference, IOMAC 2005*, 2005.

[42] L. Ljung, *System identification : theory for the user*, 2nd ed. Englewood Cliffs (N.J.) : Prentice-Hall, 1999.

[43] A. W. Ordys, "System identification, T. Sodestrom and P. Stoica. Prentice-Hall International, Hemel Hempstead, U.K. 1989, ISBN 0138812365, XXIV + 612 pp., £47.00," *Int. J. Adapt. Control Signal Process.*, vol. 7, no. 3, pp. 235–237, 1993.

[44] J.-N. Juang, "Applied system identification," 1994.

[45] P. Andersen, R. Brincker, and P. H. Kirkegaard, "Identification of Civil Engineering Structures using Vector ARMA Models," 1998.

[46] P. Van Overschee and B. D. L. R. De Moor, *Subspace Identification for Linear Systems*, no. October. Springer US, 1996.

[47] B. Peeters *et al.*, "Stochastic System Identification : Uncertainty of the Estimated Modal," no. May 2015, 1999.

[48] B. Peeters and G. De Roeck, "REFERENCE-BASED STOCHASTIC SUBSPACE IDENTIFICATION FOR OUTPUT-ONLY MODAL ANALYSIS," *Mech. Syst. Signal Process.*, vol. 13, no. 6, pp. 855–878, 1999.

[49] B. Peeters, "Comparison of System Identification Methods Using Operational Data of a Bridge Test 6WDWXV RI WKH SDSHU," no. May, 2000.

[50] R. Brincker and P. Andersen, "Understanding Stochastic Subspace Identification," 2006.

[51] B. Peeters and G. De Roeck, "Stochastic System Identification for Operational Modal Analysis: A Review," *J. Dyn. Syst. Meas. Control*, vol. 123, no. 4, 2001.

[52] M. Aoki, "State Space Modeling of Time Series," 1987.

[53] W. Scherrer, "Subspace methods for system identification. Tohru Katayama, Springer, London, 2005. No. of Pages: XVI+386. ISBN Q_8523S_981_0," *Int. J. Robust Nonlinear Control*, vol. 18, pp. 993–994, 2008.

[54] A. Benveniste and J.-. Fuchs, "Single sample modal identification of a nonstationary stochastic process," *IEEE Trans. Automat. Contr.*, vol. 30, no. 1, pp. 66–74, 1985.

[55] K. Worden *et al.*, "The fundamental axioms of structural health monitoring," *Proc. R. Soc. A Math. Phys. Eng. Sci.*, vol. 463, no. 2082, pp. 1639–1664, 2007.

[56] A. Rytter, "Vibrational Based Inspection of Civil Engineering Structures," Dept. of Building Technology and Structural Engineering, Aalborg University, 1993.

[57] M. I. Friswell, "Damage identification using inverse methods," *Philos. Trans. R. Soc. A Math. Phys. Eng. Sci.*, vol. 365, no. 1851, pp. 393–410, 2007.

[58] R. J. Schalkoff, "Pattern Recognition," in *Wiley Encyclopedia of Computer Science and Engineering*, John Wiley & Sons, Ltd, 2007.

[59] K. Worden, "STRUCTURAL FAULT DETECTION USING A NOVELTY MEASURE," *J. Sound Vib.*, vol. 201, no. 1, pp. 85–101, 1997.

[60] K. WORDEN, G. MANSON, and N. R. J. FIELLER, "DAMAGE DETECTION USING OUTLIER ANALYSIS," *J. Sound Vib.*, vol. 229, no. 3, pp. 647–667, 2000.

[61] D. Anastasopoulos, M. De Smedt, G. De Roeck, L. Vandewalle, and E. Reynders, "ScienceDirect Modal

Modal strain strain identification identification using using sub-microstrain sub-microstrain FBG FBG data data from from a a pre-stressed concrete concrete beam beam during during progressive progressive damage damage testing testing," *Procedia Eng.*, vol. 199, pp. 1846–1851, 2017.

[62] D. Anastasopoulos, M. Smedt, G. Roeck, L. Vandewalle, and E. Reynders, "Damage Identification Using Sub-Microstrain FBG Data from a Pre-Stressed Concrete Beam During Progressive Damage Testing," *Proceedings*, vol. 2, no. 8, p. 462, 2018.

[63] A. Cabboi, C. Gentile, and A. Saisi, "Vibration-based SHM of a centenary bridge: a comparative study between two different automated OMA techniques," *Eurodyn 2014 Ix Int. Conf. Struct. Dyn.*, no. July, pp. 1461–1468, 2014.

[64] C. Gentile and A. Saisi, "Ambient vibration testing of historic masonry towers for structural identification and damage assessment," vol. 21, pp. 1311–1321, 2007.

[65] D. Anastasopoulos, M. De Smedt, L. Vandewalle, G. De Roeck, and E. P. B. Reynders, "Damage identification using modal strains identified from operational fiber-optic Bragg grating data," *Struct. Heal. Monit.*, vol. 17, no. 6, 2018.

[66] C. Gentile and F. Ubertini, "Radar-based dynamic testing and system identification of a guyed mast," *AIP Conf. Proc.*, vol. 1457, no. June, pp. 318–325, 2012.

[67] C. Gentile, "Application of Radar Technology to Deflection Measurement and Dynamic Testing of Bridges," in *Radar Technology*, G. Kouemou, Ed. Rijeka: IntechOpen, 2010.

[68] C. R. Farrar, S. W. Doebling, and D. A. Nix, "Vibration–based structural damage identification," *Philos. Trans. R. Soc. London. Ser. A Math. Phys. Eng. Sci.*, vol. 359, no. 1778, 2001.

[69] J. A. Ruhl and R. M. Berdahl, "Forced vibration tests of a deepwater platform," in *Proceedings of the Annual Offshore Technology Conference*, 1979, vol. 1979-May, pp. 1341–1354.

[70] A. Heng, S. Zhang, A. C. C. Tan, and J. Mathew, "Rotating machinery prognostics: State of the art, challenges and opportunities," *Mech. Syst. Signal Process.*, vol. 23, no. 3, pp. 724–739, 2009.

[71] R. B. Randall, "State of the art in monitoring rotating machinery. Part 2," *Sound Vib.*, vol. 38, pp. 10–17, 2004.

[72] J. M. W. Brownjohn, "Structural health monitoring of civil infrastructure," *Philos. Trans. R. Soc. A Math. Phys. Eng. Sci.*, vol. 365, no. 1851, pp. 589–622, 2007.

[73] Y. J. Yan, L. Cheng, Z. Y. Wu, and L. H. Yam, "Development in vibration-based structural damage detection technique," *Mech. Syst. Signal Process.*, vol. 21, no. 5, pp. 2198–2211, 2007.

[74] S. W. Doebling, C. R. Farrar, M. B. Prime, D. W. Shewitz, and D. W. Shevitz, "Damage Identification and Health Monitoring of Structural and Mechanical Systems from Changes in Their Vibration Characteristics: A Literature Review." 1996.

[75] J. R. Casas and J. J. Moughty, "Bridge Damage Detection Based on Vibration Data : Past and New Developments," vol. 3, no. February, pp. 1–12, 2017.

[76] J. J. Moughty and J. R. Casas, "A State of the Art Review of Modal-Based Damage Detection in Bridges: Development, Challenges, and Solutions," *Appl. Sci.*, vol. 7, no. 5, 2017.

[77] H. Sohn, C. R. Farrar, F. M. Hemez, and J. J. Czarnecki, "A Review of Structural Health Monitoring Literature : 1996-2001," *Struct. Heal. Monit.*, vol. LA-13976-M, no. LA-13976-MS, pp. 1996–2001, 2003.

[78] W. Fan and P. Qiao, "Vibration-based damage identification methods: A review and comparative study,"

Struct. Heal. Monit., vol. 10, no. 1, pp. 83–111, 2011.

[79] R. Hou and Y. Xia, "Review on the new development of vibration-based damage identification for civil engineering structures: 20102019," *J. Sound Vib.*, vol. 491, 2021.

[80] A. Moallemi, A. Burrello, D. Brunelli, and L. Benini, "Model-based vs. Data-driven Approaches for Anomaly Detection in Structural Health Monitoring: a Case Study," in *2021 IEEE International Instrumentation and Measurement Technology Conference (I2MTC)*, 2021, pp. 1–6.

[81] V. R. Gharehbaghi, H. Kalbkhani, E. Noroozinejad Farsangi, T. Y. Yang, and S. Mirjalili, "A data-driven approach for linear and nonlinear damage detection using variational mode decomposition and GARCH model," *Eng. Comput.*, 2022.

[82] S. P. Gardner and R. J. Barthorpe, "On current trends in forward model-driven SHM," in *Structural Health Monitoring 2019: Enabling Intelligent Life-Cycle Health Management for Industry Internet of Things (IIOT) - Proceedings of the 12th International Workshop on Structural Health Monitoring*, 2019, vol. 2, pp. 2152–2160.

[83] O. S. Salawu, "Detection of structural damage through changes in frequency: a review," *Eng. Struct.*, vol. 19, no. 9, pp. 718–723, 1997.

[84] A. Benedetti, G. Pignagnoli, and M. Tarozzi, "Damage identification of cracked reinforced concrete beams through frequency shift," *Mater. Struct.*, vol. 51, no. 6, pp. 1–15, Dec. 2018.

[85] Y. Narkis, "Identification of Crack Location in Vibrating Simply Supported Beams," *J. Sound Vib.*, vol. 172, pp. 549–558, 1994.

[86] Y.-S. Lee and M.-J. Chung, "A study on crack detection using eigenfrequency test data," *Comput. \& Struct.*, vol. 77, pp. 327–342, 2000.

[87] P. G. Nikolakopoulos, D. E. Katsareas, and C. A. Papadopoulos, "Crack identification in frame structures," *Comput. Struct.*, vol. 64, no. 1, pp. 389–406, 1997.

[88] F. Vestroni and D. Capecchi, "DAMAGE DETECTION IN BEAM STRUCTURES BASED ON FREQUENCY MEASUREMENTS," *J. Eng. Mech.*, vol. 126, pp. 761–768, 2000.

[89] M. N. Cerri and F. Vestroni, "Detection of damage in beams subjected to diffused cracking," *J. Sound Vib.*, vol. 234, no. 2, pp. 259–276, 2000.

[90] A. Messina, E. J. Williams, and T. Contursi, "STRUCTURAL DAMAGE DETECTION BY A SENSITIVITY AND STATISTICAL-BASED METHOD," *J. Sound Vib.*, vol. 216, no. 5, pp. 791–808, 1998.

[91] R. J. Allemang and D. L. Brown, "A Correlation Coefficient for Modal Vector Analysis," 1982.

[92] D. L. Hunt, "Application of an enhanced Coordinate Modal Assurance Criterion," in *10th International Modal Analysis Conference*, 1992, vol. 1, pp. 66–71.

[93] O. Salawu and W. Clive, "Bridge Assessment Using Forced-Vibration Testing," *J. Struct. Eng.*, vol. 121, no. 2, pp. 161–173, Feb. 1995.

[94] L. Frýba and M. Pirner, "Load tests and modal analysis of bridges," *Eng. Struct.*, vol. 23, no. 1, pp. 102–109, 2001.

[95] R. Salgado, P. J. S. Cruz, L. F. Ramos, and P. B. Lourenco, "Comparison between damage detection methods applied to beam structures," 2006.

[96] L. Balsamo, S. Mukhopadhyay, R. Betti, and H. Lus, "Damage Detection Using Flexibility Proportional

Coordinate Modal Assurance Criterion,” 2014.

[97] A. Z. Khan, A. B. Stanbridge, and D. J. Ewins, “Detecting damage in vibrating structures with a scanning LDV,” *Opt. Lasers Eng.*, vol. 32, no. 6, pp. 583–592, 1999.

[98] W.-X. Ren and G. De Roeck, “Structural Damage Identification using Modal Data. I: Simulation Verification,” *J. Struct. Eng.*, vol. 128, no. 1, pp. 87–95, Jan. 2002.

[99] H. Yamaguchi, Y. Matsumoto, K. Kawarai, A. J. Dammika, S. Shahzad, and R. Takanami, “Damage detection based on modal damping change in bridges,” 2012.

[100] J. R. Casas and Á. C. Aparicio, “Structural Damage Identification from Dynami Test Data,” *J. Struct. Eng.*, vol. 120, pp. 2437–2450, 1994.

[101] C. Williams and O. S. Salawu, “Damping as a damage indication parameter BT - Proceedings of the 1997 15th International Modal Analysis Conference, IMAC. Part 2 (of 2), February 3, 1997 - February 6, 1997,” 1997, vol. 2, pp. 1531–1536.

[102] C. R. Farrar, W. E. Baker, and R. C. Dove, “Dynamic parameter similitude for concrete models,” *ACI Struct. J. (American Concr. Institute)*, vol. 91, no. 1, pp. 90–99, 1994.

[103] R. Eyre and G. Tilly, “DAMPING MEASUREMENTS ON STEEL AND COMPOSITE BRIDGES,” 1977.

[104] A. K. Pandey, M. Biswas, and M. M. Samman, “Damage detection from changes in curvature mode shapes,” *J. Sound Vib.*, vol. 145, no. 2, pp. 321–332, 1991.

[105] Y. K. Ho and D. J. Ewins, “On the structural damage identification with mode shapes,” in *Proceedings of the European COST F3 conference on system identification and structural health monitoring*, 2000, vol. 1.

[106] C. P. Ratcliffe and W. J. Bagaria, “Vibration Technique for Locating Delamination in a Composite Beam,” *AIAA J.*, vol. 36, pp. 1074–1077, 1998.

[107] M. A. Wahab and G. De Roeck, “Damage detection in bridges using modal curvatures: application to a real damage scenario,” *J. Sound Vib.*, vol. 226, pp. 217–235, 1999.

[108] C. R. Farrar and K. Worden, *Structural Health Monitoring: A Machine Learning Perspective*. 2012.

[109] L. Y. Yam, T. P. Leung, D. B. Li, and K. Z. Xue, “THEORETICAL AND EXPERIMENTAL STUDY OF MODAL STRAIN ANALYSIS,” *J. Sound Vib.*, vol. 191, no. 2, pp. 251–260, 1996.

[110] P. Cornwell, S. W. Doebling, and C. R. Farrar, “APPLICATION OF THE STRAIN ENERGY DAMAGE DETECTION METHOD TO PLATE-LIKE STRUCTURES,” *J. Sound Vib.*, vol. 224, no. 2, pp. 359–374, 1999.

[111] T. A. Duffey, S. W. Doebling, C. R. Farrar, W. E. Baker, and W. H. Rhee, “Vibration-Based Damage Identification in Structures Exhibiting Axial and Torsional Response ,” *J. Vib. Acoust.*, vol. 123, no. 1, pp. 84–91, 2000.

[112] S. Law, Z. Shi, and L. Zhang, “Structural Damage Detection from Incomplete and Noisy Modal Test Data,” *J. Eng. Mech.*, vol. 124, no. 11, pp. 1280–1288, Nov. 1998.

[113] A. K. Pandey and M. Biswas, “Damage Detection in Structures Using Changes in Flexibility,” *J. Sound Vib.*, vol. 169, no. 1, pp. 3–17, 1994.

[114] T. Toksoy and A. E. Aktan, “Bridge-condition assessment by modal flexibility,” *Exp. Mech.*, vol. 34, no. 3, pp. 271–278, 1994.

[115] J.-Y. Wang, J. Ko, and Y. Q. Ni, “Modal sensitivity analysis of Tsing Ma Bridge for structural damage detection,” in *Smart Structures*, 2000.

[116] Z. Zhang and A. Aktan, “The Damage Indices for the Constructed Facilities,” 1995.

[117] Y. Gao and B. F. Spencer, “Damage localization under ambient vibration using changes in flexibility,” *Earthq. Eng. Eng. Vib.*, vol. 1, no. 1, pp. 136–144, 2002.

[118] C. R. Farrar and S. W. Doebling, “Damage Detection and Evaluation II BT - Modal Analysis and Testing,” J. M. M. Silva and N. M. M. Maia, Eds. Dordrecht: Springer Netherlands, 1999, pp. 345–378.

[119] U. Lee and J.-W. Shin, “A frequency response function-based structural damage identification method,” *Comput. \& Struct.*, vol. 80, pp. 117–132, 2002.

[120] N.-G. Park and Y. Park, “Identification of damage on a substructure with measured frequency response functions,” *J. Mech. Sci. Technol.*, vol. 19, pp. 1891–1901, 2005.

[121] K. Worden, C. R. Farrar, J. Haywood, and M. Todd, “A review of nonlinear dynamics applications to structural health monitoring,” *Struct. Control Heal. Monit.*, vol. 15, no. 4, pp. 540–567, Jun. 2008.

[122] A. P. Bovsunovsky and C. Surace, “Considerations regarding superharmonic vibrations of a cracked beam and the variation in damping caused by the presence of the crack,” *J. Sound Vib.*, vol. 288, no. 4–5, pp. 865–886, 2005.

[123] P. Omenzetter and J. M. W. Brownjohn, “Application of time series analysis for bridge monitoring,” *Smart Mater. Struct.*, vol. 15, no. 1, pp. 129–138, 2006.

[124] G. E. P. Box and G. M. Jenkins, “Time series analysis, forecasting and control,” 1970.

[125] Q. Mei and M. Gül, “Novel Sensor Clustering–Based Approach for Simultaneous Detection of Stiffness and Mass Changes Using Output-Only Data,” *J. Struct. Eng.*, vol. 141, no. 10, p. 4014237, Oct. 2015.

[126] M. Spiridonakos and E. N. Chatzi, “Metamodeling of nonlinear structural systems with parametric uncertainty subject to stochastic dynamic excitation,” *Earthquakes Struct.*, vol. 8, pp. 915–934, 2015.

[127] Z. K. Peng, Z. Q. Lang, C. Wolters, S. A. Billings, and K. Worden, “Feasibility study of structural damage detection using NARMAX modelling and Nonlinear Output Frequency Response Function based analysis,” *Mech. Syst. Signal Process.*, vol. 25, no. 3, pp. 1045–1061, 2011.

[128] S. Mallat, “A wavelet tour of signal processing,” 1998.

[129] Y. Xiao-zhong and Y. Sheng-lin, “Hilbert-Huang transform and its application,” *J. Zhenjiang Coll.*, 2007.

[130] N. E. Huang *et al.*, “The empirical mode decomposition and the Hilbert spectrum for nonlinear and non-stationary time series analysis,” *Proc. R. Soc. London. Ser. A Math. Phys. Eng. Sci.*, vol. 454, no. 1971, pp. 903–995, Mar. 1998.

[131] E. Douka and L. J. Hadjileontiadis, “Time-frequency analysis of the free vibration response of a beam with a breathing crack,” *Ndt \& E Int.*, vol. 38, pp. 3–10, 2005.

[132] N. J. Yang, Y. Lei, S. Lin, and N. Huang, “Hilbert-Huang Based Approach for Structural Damage Detection,” *J. Eng. Mech.*, vol. 130, no. 1, pp. 85–95, Jan. 2004.

[133] J. A. Anderson, *An introduction to neural networks*. MIT press, 1995.

[134] X. Wu, J. Ghaboussi, and J. H. Garrett, “Use of neural networks in detection of structural damage,” *Comput. Struct.*, vol. 42, no. 4, pp. 649–659, 1992.

[135] C.-B. Yun and E. Y. Bahng, “Substructural identification using neural networks,” *Comput. Struct.*, vol. 77, no. 1, pp. 41–52, 2000.

[136] B. A. Paya, I. I. Esat, and M. N. M. Badi, “ARTIFICIAL NEURAL NETWORK BASED FAULT DIAGNOSTICS OF ROTATING MACHINERY USING WAVELET TRANSFORMS AS A PREPROCESSOR,” *Mech. Syst. Signal Process.*, vol. 11, no. 5, pp. 751–765, 1997.

[137] D. E. Goldberg, “Genetic Algorithms in Search Optimization and Machine Learning,” 1988.

[138] H. Hong and X. Yong, “Vibration-based Damage Detection of Structures by Genetic Algorithm,” *J. Comput. Civ. Eng.*, vol. 16, no. 3, pp. 222–229, Jul. 2002.

[139] J.-H. Chou and J. Ghaboussi, “Genetic algorithm in structural damage detection,” *Comput. Struct.*, vol. 79, no. 14, pp. 1335–1353, 2001.

[140] A. M. Raich and J. Ghaboussi, “Implicit representation in genetic algorithms using redundancy.,” *Evol. Comput.*, vol. 5, no. 3, pp. 277–302, 1997.

[141] J. E. Mottershead and M. I. Friswell, “Model Updating In Structural Dynamics: A Survey,” *J. Sound Vib.*, vol. 167, no. 2, pp. 347–375, 1993.

[142] T. Marwala, “Finite-element-model Updating Using Computional Intelligence Techniques,” 2010.

[143] M. Baruch, “Optimization Procedure to Correct Stiffness and Flexibility Matrices Using Vibration Tests,” *AIAA J.*, vol. 16, no. 11, pp. 1208–1210, Nov. 1978.

[144] P. L. Liu, “Identification and Damage Detection of Trusses Using Modal Data,” *J. Struct. Eng.*, vol. 121, no. 4, pp. 599–608, Apr. 1995.

[145] D. C. Zimmerman and M. Kaouk, “Structural damage detection using a minimum rank update theory,” *J. Vib. Acoust.*, vol. 116, pp. 222–231, 1994.

[146] S. W. Doebling, “Minimum-rank optimal update of elemental stiffness parameters for structural damage identification,” *AIAA J.*, vol. 34, no. 12, pp. 2615–2621, Dec. 1996.

[147] J. M. Ricles and J. B. Kosmatka, “Damage detection in elastic structures using vibratory residual forces and weighted sensitivity,” *AIAA J.*, vol. 30, no. 9, pp. 2310–2316, Sep. 1992.

[148] C. Farhat and F. M. Hemez, “Updating finite element dynamic models using an element-by-element sensitivity methodology,” *AIAA J.*, vol. 31, no. 9, pp. 1702–1711, Sep. 1993.

[149] T. W. Lim and T. A. L. Kashangaki, “Structural damage detection of space truss structures using best achievable eigenvectors,” *AIAA J.*, vol. 32, no. 5, pp. 1049–1057, May 1994.

[150] E. P. Carden and P. Fanning, “Vibration Based Condition Monitoring: A Review,” *Struct. Heal. Monit.*, vol. 3, no. 4, 2004.

[151] A. Berman, “Mass Matrix Correction Using an Incomplete Set of Measured Modes,” *AIAA J.*, vol. 17, no. 10, pp. 1147–1148, Oct. 1979.

[152] J. J. Moughty and J. R. Casas, “Performance Assessment of Vibration Parameters as Damage Indicators for Bridge Structures under Ambient Excitation,” in *Procedia Engineering*, 2017, vol. 199, pp. 1970–1975.

[153] M. R. Kaloop and J. W. Hu, “Stayed-Cable Bridge Damage Detection and Localization Based on Accelerometer Health Monitoring Measurements,” *Shock Vib.*, vol. 2015, p. 102680, 2015.

[154] J. M. Ndambi, J. Vantomme, and K. Harri, “Damage assessment in reinforced concrete beams using eigenfrequencies and mode shape derivatives,” *Eng. Struct.*, vol. 24, no. 4, pp. 501–515, 2002.

[155] I. Talebinejad, C. Fischer, and F. Ansari, “Numerical Evaluation of Vibration-Based Methods for Damage Assessment of Cable-Stayed Bridges,” *Comput. Civ. Infrastruct. Eng.*, vol. 26, no. 3, pp. 239–251, Apr.

2011.

[156] P. J. S. Cruz and R. Salgado, “Performance of vibration-based damage detection methods in bridges,” *Comput. Civ. Infrastruct. Eng.*, vol. 24, no. 1, pp. 62–79, 2008.

[157] European Techincal Committee, “UNI EN 206:2021 - Calcestruzzo: Specificazione, prestazione, produzione e conformità.” 2021.

[158] L. Trifone, “A Study of the Correlation Between Static and Dynamic Modulus of Elasticity on Different Concrete Mixes.” 2017.

[159] K. J. Bastgen and V. Hermann, “Experience made in determining the static modulus of elasticity of concrete,” *Matériaux Constr.*, vol. 10, no. 6, pp. 357–364, 1977.

[160] Italian Ministry of Infrastructures and Transports, “Aggiornamento delle «Norme tecniche per le costruzioni», 2018,” pp. 1–198, 2018.

[161] European Technical Committee, “EN 10025: Hot rolled products of structural steel.” .

[162] E. T. Committe, “EN 10219: Cold formed welded steel structural hollow sections.” .

[163] Italian National Research Council, “CNR 10018/85 – Apparecchi di appoggio per le costruzioni, Istruzioni per l’impiego.” .

[164] FIP Industriale, “Rubber sheets and mats datasheet.” .

[165] C. Viggiani, R. Lancellotta, and J. Calavera, “Fondazioni Superficiali : Cedimenti S t = S i + S c + S s,” 2015.

[166] G. De Roeck, A. Teughels, and E. Reynders, “Damage identification of civil engineering structures based on operational modal data,” in *Proceedings of the 1st International Operational Modal Analysis Conference, IOMAC*, 2005.

[167] S. W. Doebling, C. R. Farrar, and M. B. Prime, “Summary Review of Vibration-Based Damage Identification Methods,” *Shock Vib. Dig.*, vol. 30, no. 2, pp. 91–105, 1998.

[168] F. Magalhães, A. Cunha, and E. Caetano, “Vibration based structural health monitoring of an arch bridge: From automated OMA to damage detection,” *Mech. Syst. Signal Process.*, vol. 28, pp. 212–228, 2012.

[169] C. Gentile, M. Guidobaldi, and A. Saisi, “One-year dynamic monitoring of a historic tower: damage detection under changing environment,” *Meccanica*, vol. 51, no. 11, 2016.

[170] J. MAECK and G. D. E. ROECK, “DAMAGE ASSESSMENT USING VIBRATION ANALYSIS ON THE Z24-BRIDGE,” *Mech. Syst. Signal Process.*, vol. 17, no. 1, 2003.

[171] J. Maeck, B. Peeters, and G. De Roeck, “Damage identification on the Z24 bridge using vibration monitoring,” *Smart Mater. Struct.*, vol. 10, no. 3, 2001.

[172] M. Döhler, F. Hille, L. Mevel, and W. Rücker, “Structural health monitoring with statistical methods during progressive damage test of S101 Bridge,” *Eng. Struct.*, vol. 69, pp. 183–193, 2014.

[173] C. R. Farrar *et al.*, “Dynamic characterization and damage detection in the I-40 bridge over the Rio Grande.” 1994.

[174] C. R. Farrar, P. J. Cornwell, S. W. Doebling, and M. B. Prime, “Structural Health Monitoring Studies of the Alamosa Canyon and I-40 Bridges,” no. January 2014, 2000.

[175] P. F. Giordano and M. P. Limongelli, “Vibration-based damage identification for the S101 Bridge benchmark bridge: a comparison of indicators,” *9th European Workshop on Structural Health Monitoring - EWSHM*. 2018.

[176] R. G. Lauzon and J. T. DeWolf, "Ambient Vibration Monitoring of a Highway Bridge Undergoing a Destructive Test," *J. Bridg. Eng.*, vol. 11, no. 5, 2006.

[177] Y. E. Zhou and A. E. Biegalski, "Investigation of Large Web Fractures of Welded Steel Plate Girder Bridge," *J. Bridg. Eng.*, vol. 15, no. 4, 2010.

[178] R. Haghani, M. Al-Emrani, and M. Heshmati, "Fatigue-Prone Details in Steel Bridges," *Buildings*, vol. 2, no. 4, 2012.

[179] M. Chajes, D. Mertz, S. Quiel, H. Roecker, and J. Milius, "Steel Girder Fracture on Delaware's I-95 Bridge over the Brandywine River," in *Structures Congress 2005*, 2005.

[180] SENSR, "CX1 Network Accelerometer & Inclinometer." .

[181] R. Brincker, L. Zhang, and P. Andersen, "Modal identification of output-only systems using frequency domain decomposition," *Smart Mater. Struct.*, vol. 10, no. 3, pp. 441–445, 2001.

[182] F. Magalhães, Á. Cunha, and E. Caetano, "Dynamic monitoring of a long span arch bridge," *Eng. Struct.*, vol. 30, no. 11, pp. 3034–3044, 2008.

[183] F. Magalhães, Á. Cunha, E. Caetano, and F. Magalha, "Online automatic identification of the modal parameters of a long span arch bridge," *Mech. Syst. Signal Process.*, vol. 23, no. 2, pp. 316–329, 2009.

[184] A. Otto, "OoMA Toolbox - MATLAB Central File Exchange." 2021.

[185] E. Cheynet, "Operational modal analysis with automated SSI-COV algorithm." Zenodo, 2020.

[186] F. Magalhães and Á. Cunha, "Explaining operational modal analysis with data from an arch bridge," *Mech. Syst. Signal Process.*, vol. 25, no. 5, pp. 1431–1450, 2011.

[187] R. J. Allemang, "The modal assurance criterion--twenty years of use and abuse," *Sound Vib.*, vol. 37, no. 8, pp. 14–23, 2003.

[188] F. Bazzucchi, L. Restuccia, and G. Ferro, "Considerations over the Italian road bridge infrastructure safety after the Polcevera viaduct collapse: past errors and future perspectives," *Frat. ed Integrità Strutt.*, vol. 12, no. 46, 2018.

[189] A. Brencich, S. Lagomarsino, and G. Riotto, "Dynamic identification of reduced scale masonry bridges," in *IOMAC 2009 - 3rd International Operational Modal Analysis Conference*, 2009.

[190] M. Tarozzi, G. Pignagnoli, and A. Benedetti, "Identification of damage-induced frequency decay on a large-scale model bridge Identification of damage-induced frequency decay on a large-scale model bridge," *Eng. Struct.*, vol. 221, no. October, p. 111039, 2020.

[191] J. Maeck *et al.*, "Damage identification in reinforced concrete structures by dynamic stiffness determination," *Eng. Struct.*, vol. 22, no. 10, pp. 1339–1349, 2000.

[192] D. Bolognani *et al.*, "IWSHM 2017: Quantifying the benefit of structural health monitoring: what if the manager is not the owner?," *Struct. Heal. Monit.*, vol. 17, no. 6, 2018.

[193] L. IANNACONE, P. GARDONI, P. F. GIORDANO, and M. P. LIMONGELLI, "Decision Making Based on the Value of Information of Different Inspection Methods," in *Structural Health Monitoring 2019*, 2019.

[194] D. M. Frangopol, Y. Dong, and S. Sabatino, "Bridge life-cycle performance and cost: analysis, prediction, optimisation and decision-making," *Struct. Infrastruct. Eng.*, vol. 13, no. 10, 2017.

[195] Y. Liang, D. Li, G. Song, and Q. Feng, "Frequency Co-integration-based damage detection for bridges under the influence of environmental temperature variation," *Measurement*, vol. 125, no. April, pp. 163–

175, 2018.

[196] K. Van Den Abeele and J. De Visscher, “Damage assessment in reinforced concrete using spectral and temporal nonlinear vibration techniques,” *Cem. Concr. Res.*, vol. 30, no. 9, pp. 1453–1464, 2000.

[197] V. Askegaard and H. E. Langsœ, “Correlation between changes in dynamic properties and remaining carrying capacity,” *Mater. Struct.*, vol. 19, no. 1, pp. 11–20, 1986.

[198] S. A. Neild, M. S. Williams, and P. D. McFadden, “Nonlinear Vibration Characteristics of Damaged Concrete Beams,” *J. Struct. Eng.*, vol. 129, no. 2, pp. 260–268, 2003.

[199] C. M. Tan, “Nonlinear vibrations of cracked reinforced concrete beams.” 2003.

[200] S. J. A. Koh, M. Maalej, and S. T. Quek, “Damage Quantification of Flexurally Loaded RC Slab Using Frequency Response Data,” *Struct. Heal. Monit.*, vol. 3, no. 4, 2004.

[201] M. Massenzio, E. Jacquelin, and P. A. Ovigne, “Natural frequency evaluation of a cracked RC beam with or without composite strengthening for a damage assessment,” *Mater. Struct.*, vol. 38, no. 10, 2005.

[202] N. Baghiee, M. R. Esfahani, and K. Moslem, “Studies on damage and FRP strengthening of reinforced concrete beams by vibration monitoring,” *Eng. Struct.*, vol. 31, no. 4, 2009.

[203] M. Musiał, “Static and dynamic stiffness of reinforced concrete beams,” *Arch. Civ. Mech. Eng.*, vol. 12, no. 2, pp. 186–191, 2012.

[204] W. I. Hamad, J. S. Owen, and M. F. M. Hussein, “Modelling the degradation of vibration characteristics of reinforced concrete beams due to flexural damage,” *Struct. Control Heal. Monit.*, vol. 22, no. 6, pp. 939–967, 2015.

[205] A. Benedetti, J. M. Nichols, and A. Tomor, “Influence of Environmental Degradation on Dynamic Properties of Masonry Bridges,” *16th IB2MAC Conf.*, no. June, pp. 1029–1035, 2016.

[206] C. M. Newtson, G. P. Johnson, and B. T. Enomoto, “Fundamental Frequency Testing of Reinforced Concrete Beams,” *J. Perform. Constr. Facil.*, vol. 20, no. 2, 2006.

[207] A. Castel, R. I. Gilbert, and G. Ranzi, “Instantaneous Stiffness of Cracked Reinforced Concrete Including Steel-Concrete Interface Damage and Long-Term Effects,” *J. Struct. Eng.*, vol. 140, no. 6, 2014.

[208] T. Xu and A. Castel, “Modeling the dynamic stiffness of cracked reinforced concrete beams under low-amplitude vibration loads,” *J. Sound Vib.*, vol. 368, pp. 135–147, 2016.

[209] T. G. CHONDROS, A. D. DIMAROGONAS, and J. YAO, “VIBRATION OF A BEAM WITH A BREATHING CRACK,” *J. Sound Vib.*, vol. 239, no. 1, 2001.

[210] J. S. Bendat, *Nonlinear Systems Techniques and Applications*. John Wiley & Sons, 1998.

[211] H. Kim and H. Melhem, “Fourier and wavelet analyses for fatigue assessment of concrete beams,” *Exp. Mech.*, vol. 43, no. 2, 2003.

[212] W. L. Bayissa and N. Haritos, “Experimental investigation into vibration characteristics of a cracked RC T-beam,” in *Fourth Australasian Congress on Applied Mechanics*, 2005, pp. 263–269.

[213] Y. Gao, Y. Du, Y. Jiang, and W. Zhao, “Research on Cracking of Reinforced Concrete Beam and Its Influence on Natural Frequency by Expanded Distinct Element Method,” *J. Aerosp. Eng.*, vol. 30, no. 2, pp. 1–7, 2017.

[214] T. Nagayama and B. F. Spencer Jr, “Structural health monitoring using smart sensors,” 2007.

[215] A. Sabato, C. Niezrecki, and G. Fortino, “Wireless MEMS-based accelerometer sensor boards for structural vibration monitoring: a review,” *IEEE Sens. J.*, vol. 17, no. 2, pp. 226–235, 2017.

[216] N. Testoni, F. Zonzini, A. Marzani, V. Scarponi, and L. De Marchi, "A Tilt Sensor Node Embedding a Data-Fusion Algorithm for Vibration-Based SHM," *Electronics*, vol. 8, no. 1, p. 45, 2019.

[217] C. Rainieri and G. Ã. Fabbrocino, "Automated output-only dynamic identification of civil engineering structures," *Mech. Syst. Signal Process.*, vol. 24, no. 3, pp. 678–695, 2010.

[218] Rilem Technical Committee, "Recommendation of RILEM TC 212-ACD: acoustic emission and related NDE techniques for crack detection and damage evaluation in concrete," *Mater. Struct.*, vol. 43, no. 9, pp. 1183–1186, 2010.

[219] C. U. Grosse and M. Ohtsu, *Acoustic emission testing*. Springer Science \& Business Media, 2008.

[220] D. Soulioti, N. M. Barkoula, A. Paipetis, T. E. Matikas, T. Shiotani, and D. G. Aggelis, "Acoustic emission behavior of steel fibre reinforced concrete under bending," *Constr. Build. Mater.*, vol. 23, no. 12, pp. 3532–3536, 2009.

[221] K. Ohno and M. Ohtsu, "Crack classification in concrete based on acoustic emission," *Constr. Build. Mater.*, vol. 24, no. 12, pp. 2339–2346, 2010.

[222] E. Proverbio, G. Campanella, and V. Venturi, "EVALUATION OF DAMAGE EVOLUTION UNDER REPEATED LOADING OF POST-TENSIONED CONCRETE BEAMS BY ACOUSTIC EMISSION," 2008.

[223] J. Ongpeng, A. Oreta, and S. Hirose, "Monitoring Damage Using Acoustic Emission Source Location and Computational Geometry in Reinforced Concrete Beams," *Appl. Sci.*, vol. 8, no. 2, 2018.

[224] D. G. Aggelis, D. V Soulioti, N. Sapouridis, N. M. Barkoula, A. S. Paipetis, and T. E. Matikas, "Acoustic emission characterization of the fracture process in fibre reinforced concrete," *Constr. Build. Mater.*, vol. 25, no. 11, pp. 4126–4131, 2011.

[225] M. Ohtsu and Y. Tomoda, "Phenomenological model of corrosion process in reinforced concrete identified by acoustic emission," *ACI Mater. J.*, vol. 105, no. 2, p. 194, 2008.

[226] R. Brincker and C. Ventura, *Introduction to Operational Modal Analysis*. Wiley, 2015.

[227] J. Zhang, K. Maes, G. De Roeck, E. Reynders, C. Papadimitriou, and G. Lombaert, "Optimal sensor placement for multi-setup modal analysis of structures," *J. Sound Vib.*, vol. 401, 2017.

[228] University "La Sapienza," "APESS - Technical reports," 2019.

[229] Insula -Architettura, F. Cellini, and F. Brancaleoni, "Ponte degli Annibaldi," 2015. [Online]. Available: https://archidiap.com/opera/ponte-degli-annibaldi/.

[230] E. Reynders, F. Magalhaes, G. De Roeck, and A. Cunha, "Merging strategies for multi-setup Operational Modal Analysis: Application to the Luiz i steel arch bridge," in *Conference Proceedings of the Society for Experimental Mechanics Series*, 2009, p. Society for Experimental Mechanics (SEM)-.

[231] E. Tavelli and et Al., "Winet Srl." [Online]. Available: https://www.winetsrl.com.

[232] R. Brincker, "Some Elements of Operational Modal Analysis," *Shock Vib.*, vol. 2014, 2014.

[233] ST Microelectronics, "LSM6DS3 iNEMO inertial module (sensor A30)," no. May, pp. 1–95, 2015.